Development of Electrospun Multifunctional Fibrous Structures for Icephobic and Superhydrophobic Applications

Mahmut Taş

Thesis submitted to the University of Nottingham for the degree of Doctor of Philosophy

PhD. Materials Engineering and Materials Design

Faculty of Engineering

The University of Nottingham

January 2022

Abstract

Icephobicity is defined as the ability of a solid surface to prevent ice accumulation or the potential of repelling ice from the surface. On the other hand, superhydrophobicity is a physical property of a surface, which means lacking affinity for water, and tending to repel water. Although these two surface properties have critical application areas such as energy harvesting systems, transportation, corrosion resistance coatings and friction reduction, fabricating superhydrophobic and icephobic surfaces is still a big challenge due to the lack of scalable, straightforward, and cost-effective production methods. Moreover, integrating additional functions, including electromagnetic interference (EMI) shielding and electrical conductivity to these materials to achieve multifunctionality, enables many modern applications, such as EMI shielding protective devices and power transmission systems.

Electrospinning is one of the most commonly used methods to produce nano-sized polymeric fibrous membranes or coatings. Unique properties such as high surface-to-volume ratio, high porosity interconnected open pore structures, and adjustable pore sizes make electrospun membranes irreplaceable. However, the potential of using the electrospinning method to produce superhydrophobic and icephobic surfaces is still not investigated in depth. Although there are some studies on the superhydrophobic application of electrospun membranes, considerable challenges remain, such as expensive chemicals, low reproducibility, complex production techniques, and the necessity of a post-treatment or functionalization step. Moreover, electrospun membranes may be a good candidate for icephobic applications based on the Cassie-Baxter icing state or specific material design such as slippery liquid-infused porous structures (SLIPS). In the Cassie-Baxter icing state, water does not penetrate the details of roughness but sits on the air pockets, which provides a low icing area between the ice and the surface, resulting in a lowered work of adhesion of ice. However, no report has been found that explores

the potential of the electrospinning method for icephobic applications. In this thesis, the potential of using electrospinning method to fabricate superhydrophobic and icephobic surfaces has been explored.

Polyvinylidene fluoride-co-hexafluoropropylene (PVDF-co-HFP), which is a low surface energy polymer, was used to explore the potential of using electrospinning method to design a one-step production method of superhydrophobic surfaces without a post-treatment or nanofiller by only changing the production parameters of electrospinning. The proposed method has significant benefits such as shortened processes, less material use, and low-cost production compared to multistep methods reported in the literature. Moreover, the roles of each parameter on surface topography, contact angle, and fibre formation have been discussed. Superhydrophobicity has been achieved thanks to the synergetic effect of the roughness and the low surface tension of the polymer. Additionally, the lowest contact angle hystereses were less than 10°, which is one of the requirements of superhydrophobicity and indicates good mobility of the water droplet on the surface, thanks to the Cassie-Baxter state exhibited.

Since the electrospun PVDF-co-HFP nanofibre membranes fabricated had a good porosity and oleophilic nature, their potential as the porous part of the SLIPS has been explored. The designed structure exhibited exceptional icephobic properties (lower than 1 kPa, one of the lowest ice adhesion strengths reported in the literature) with smooth surface topography and decreased water contact angle. As the water droplet sat completely on a thin film of lubricating liquid thanks to encapsulated regime achieved, ice adhesion strength was reduced significantly. It was also found that these SLIPS had outstanding flexibility and transparency (>90%), resulting from refractive index matching of polymer used and lubricants.

Moreover, a novel multifunctional electrospun membrane was designed and produced for outdoor EMI shielding applications, using recycled polyethylene terephthalate (r-PET) instead of virgin polymers to widen the horizon of using

recycled materials. A two-step production process has been applied, which consisted of (i) fabrication of r-PET/magnetite electrospun membranes and (ii) surface modification by fluorinated silane functionalized SiO_2 nanoparticles (FSFS). The coaxial waveguide method, a common method to investigate EMI shielding efficiency, was used to investigate EMI shielding properties, and it was found that 20 wt.% magnetite-loaded nanofibre membrane had an EMI shielding efficiency of 22 dB, which was equivalent to above 99% shielding efficiency between 400 MHz and 6 GHz. After FSFS treatment, the nanofibre membrane exhibited Cassie-Baxter state resulted in less than 5° of contact angle hysteresis and approximately 50 kPa ice adhesion strength, thanks to lower surface energy and hierarchical topography, which was beneficial for both icephobic and superhydrophobic performance.

Acknowledgements

First and foremost, I would like to praise Allah the Almighty, the Most Gracious, and the Most Merciful for His blessing given to me during my study and in completing this thesis. May Allah's blessing goes to His final Prophet Muhammad (peace be up on him), his family and his companions.

I would like to express my sincere gratitude to my Supervisor Dr Xianghui Hou, for his endless support, patience, and great contribution to this study. I have learned so much from him during my Ph.D., it was a big chance and a great pleasure to become one of his students. I also wish to thank Dr Ifty Ahmed and Dr Fang Xu for their encouraging comments about the work and also for the great advice given. I am deeply grateful to all my supervisors for their contributions which were influential in shaping my experiment methods and critiquing my results.

I express my sincere thanks to my friends, namely Umar Gishiwa Musa, Fatih Kayır, and Yasin Altın, for helping me through the difficult times and for all their support. I also wish to thank my family, especially my mother, my father, my sister and brother, for their endless support during my Ph.D.

I would like to thank the Scientific and Technological Research Council of Turkey (TUBITAK), Directorate of Science Fellowships and Grant Programmes (BIDEB) for funding the first two years of my Ph.D. with program number 2213.

I also wish to thank the University of Nottingham, Faculty of Engineering, for the funding of the third-year tuition fee and the Henry Royce Institute for The Royce Student Equipment Access Scheme.

And lastly and most importantly, I would like to thank my dearest, my Muguet, for always being with me even when we were on different continents. Having you is the most important success of my life. You have changed my life for the better, and you have a great share in my achievements. Without you, none of these would be possible.

List of Publications

Tas, Mahmut; Memon, Halar; Xu, Fang; Ahmed, Ifty; Hou, Xianghui; *Electrospun nanofibre membrane-based transparent slippery liquid-infused porous surfaces with icephobic properties***, Colloids and Surfaces A: Physicochemical and Engineering Aspects**, 585, 124177, 2020, Elsevier

Tas, Mahmut; Xu, Fang; Ahmed, Ifty; Hou, Xianghui; *One-step fabrication of superhydrophobic P (VDF-co-HFP) nanofibre membranes using* electrospinning *technique*, **Journal of Applied Polymer Science**, 137, 24, 48817, 2020, Wiley

Tas, Mahmut; Musa, Umar; Smart, Christopher; Xu, Fang; Ahmed, Ifty; Hou, Xianghui; *Recycled PET/Magnetite Nanocomposite Electrospun Membranes with Icephobic Properties for Outdoor Electromagnetic Shielding Applications*, **Manuscript preparation in progress.**

List of Funding

The Scientific and Technological Research Council of Turkey (TUBITAK), *Directorate of Science Fellowships and Grant Programmes (BIDEB),* **2213- A International Ph.D. Fellowship Programme,** 2018-2020

University of Nottingham, *University Research Scholarship***, Funding Programme for International Ph.D. Students,** 2020-2021

The Henry Royce Institute, The UK National Institute For Advanced Materials, Ph.D. **Royce Student Equipment Access Scheme**, 2019-2019

List of Abbreviations

A	:	Specific surface area
a	:	Acceleration
ATR	:	Attenuated total reflectance
CA	:	Cellulose Acetate
CF_4	:	Tetraflorometan
CNTs	:	Carbon nanotube
DMAc	:	Dimethylacetamide
DMF	:	Dimethylformamide
DSC	:	Differential scanning calorimetry
E	:	Electrical field
EMSO	:	Ester Modified Silicone Oil
FP8	:	Type of fluorinated polyhedral oligomeric silsesquioxane
FPSi8	:	Type of fluorinated polyhedral oligomeric silsesquioxane
FT-IR	:	Fourier-transform infrared spectroscopy
H	:	Air-gap Distance (cm)
kV	:	Kilovolt
L	:	Length of capillary tube (cm)
M	:	The mass of a given volume element
ml/h	:	Millilitre per hour
M_n	:	Molecular number
M_W	:	Molecular weight
MWNT	:	Multi-walled carbon nanotube
NaCl	:	Sodium chloride
PAN	:	Poly (acrylonitrile)

PCL : Poly (caprolactone)

PDA : Poly (dopamine)

PDMS : Poly (dimethylsiloxane)

PEO : Poly (ethylene oxide)

PES : Poly (ether sulfone)

PFDTES : 1H,1H,2H,2H-Perfluorodecyltriethoxysilane

PFOTES : 1H,1H,2H,2H-Perfluorooctyltriethoxysilane

PMMA : Poly (methyl methacrylate)

POSS : Polyhedral oligomeric silsesquioxane

PS : Poly (styrene)

PULL : Pullulan

PVA : Poly (vinyl alcohol)

PVDF : Poly (vinylidene fluoride)

PVDF-co-HFP : Poly(vinylidene fluoride-co-hexafluoropropylene)

PVP : Poly (vinyl pyrrolidone)

Q : The available charge for a given volume element

R : Radius of the tube (cm)

S : Sum of squares

SEBS : Polystyrene-b-poly (ethylene-co-butylene)-b-polystyrene

SEM : Scanning electron microscope

SiO_2 : Silicon dioxide

TGA : Thermogravimetric analysis

THF : Tetrahydrofuran

THV : Ter polymer

TiO_2 : Titanium dioxide

TPU : Thermoplastic Poly (urethane)

UV	**:**	Ultraviolet
V	**:**	Volume
Vc^2	**:**	Voltage threshold (kV)
WCA	**:**	Water contact angle
ZnO	**:**	Zinc oxide
γ	**:**	Surface tension (dyne/cm)
γ_{sl}	**:**	Solid/liquid interfacial energy
γ_{so}	**:**	Solid/gas interfacial energy

Table of Content

List of Table

List of Figures

CHAPTER 1

Introduction

1.1 Background of the Work

Superhydrophobic surfaces have a remarkable ability to repel water or any aqueous medium, and they have received significant attention in the last decades. Since 2004, studies carried out on superhydrophobic surfaces, and their applications have grown sharply, and new application areas are proposed for superhydrophobic surfaces. Superhydrophobic surfaces are used for several aims, including preventing metals from corrosion [1], reducing the friction and drag in vehicles [2], providing anti-microbial and self-cleaning properties [3], and separating oil/water emulsions [4]. Due to the increasing demand for superhydrophobic surfaces, the market share is expected to grow around 32% between 2021 and 2028 [5].

To investigate the superhydrophobic properties, water contact angle, which is measured where liquid-vapour interface meets a solid surface, and contact angle hysteresis are used. Briefly, superhydrophobic surfaces are defined as surfaces with a water contact angle of over 150° and contact angle hysteresis lower than 10°. Researchers are inspired by nature, with various examples of superhydrophobic creatures such as the lotus leaf, insect wings, mosquito eyes, and shark skins to fabricate artificial superhydrophobic surfaces [6]. The superhydrophobic effects of these natural creatures are exhibited mainly due to their specific surface structures, as seen in Figure 1.1.

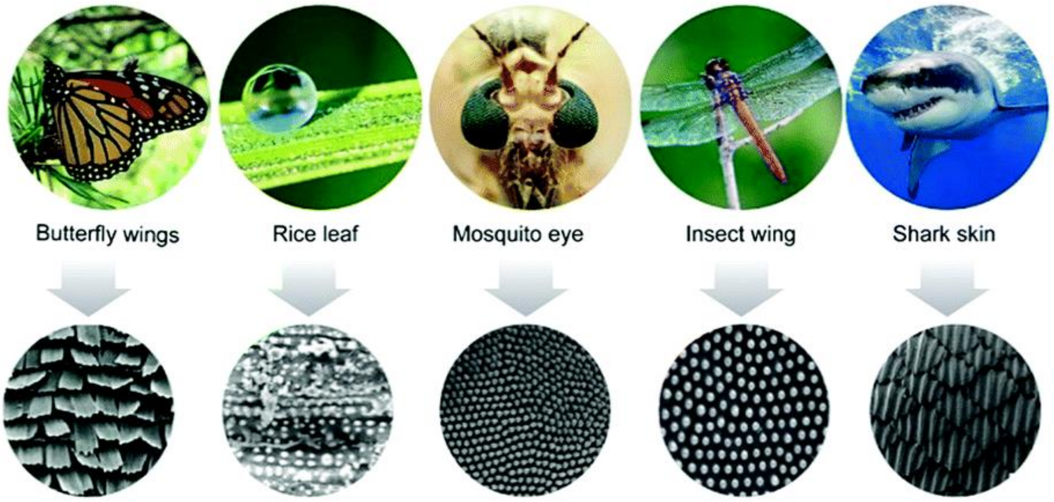

Figure 1.1 *Examples of superhydrophobic structure in Nature [6].*

Fabrication of superhydrophobic surfaces for a variety of industries and using different materials, such as polymers, metals, and ceramics, is also a crucial topic. The formation of the specific surface roughness and hydrophilization of the surface are the key steps to prepare a superhydrophobic surface [7]. However, there are some significant problems in the fabrication of superhydrophobic surfaces. For industrial applications, the methods used need to be scalable, cost-effective, and repeatable. On the other hand, the durability of the superhydrophobic effect is another problem for most of the proposed methods. Particle-based coatings, plasma treatments, and chemical modification of the surfaces are known as less durable methods. The mechanical effects, UV-exposure, basic or acidic mediums, and common solvents can easily wipe out the superhydrophobic effect [3].

Researchers recently found out that, when the Cassie-Baxter state, which focuses on incomplete wetting of the surface with the liquid achieved there is a relation between superhydrophobicity and icephobicity [7] and there have been many other studies published to link these two features [8]. Icephobicity can be defined as the ability of a solid surface to prevent ice accretion and/or repel formed ice easily due to specific surface chemistry and/or topography. This characteristic has critical importance because ice accumulation on the surfaces often causes severe problems in applications such as low efficiency of energy systems, delays in air transportation or personal injuries from falling ice masses, and structural damage of buildings due to the excessive weight of ice.

Researchers have investigated many approaches to prevent surfaces from ice-causing problems [9], such as chemicals having the de-icing ability (mostly ethylene or propylene glycol), mechanical ice removal techniques, or heating systems. However, although these methods are considered efficient in ice mitigation, they also have critical problems such as high energy consumption or harmful impacts on the environment. As such, it is vital to produce surfaces with icephobic or anti-icing capability to reduce the impact of the ice accretion for many industrial sectors. The materials used to prepare anti-icing or de-icing coatings are given in Figure 1.2.

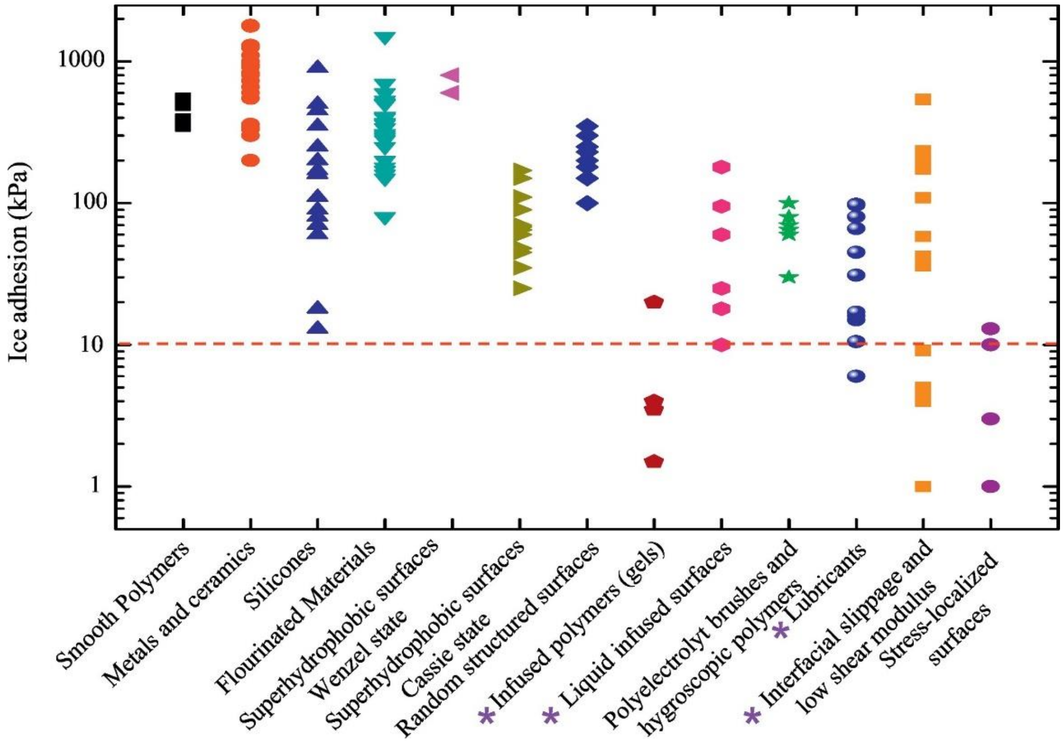

Figure 1. 2 *Ice adhesion values for different material categories (icephobicity is considered below the dotted line, wet-state icephobic materials are shown with a star symbol) [9].*

As stated in Figure 1.2, with the improving designs and strategies, it is possible to achieve lower than 1 kPa of ice adhesion strength values, which proves an extraordinary icephobicity, using passive methods. Among all proposed strategies, an alternative approach, slippery liquid-infused porous surfaces (SLIPS) proposed by Aizenberg *et al*. [10], is one of the promising methods to produce icephobic structures. They mimicked the slippery nature of the Nepenthes pitcher plant, which mainly comprised two parts: 1) porous surface and 2) lubricant and unusual slippery behaviour had been observed against immiscible liquids, as well as insects. More information on SLIPS will be provided in Section 2.3.4.

On the other hand, combining different properties or functions in a single material can be a significant challenge. Such combinations may often be required in various situations within the industry or other scenarios. Multifunctional nanocomposites are expected to possess various functionalities in one structure to achieve a desirable design for specific applications [11]. Generally, polymers are used as the matrix phase of multifunctional nanocomposite materials due to their native properties, such as corrosion resistance, ease of processability, toughness, and lightweight, etc. Depending on the properties of the reinforcement phase, it is possible to achieve various material performance characteristics, such as electrical conductivity, electromagnetic shielding efficiency, high mechanical properties, and thermal durability [11]. The concept of multifunctional nanocomposites is illustrated in Figure 1.3.

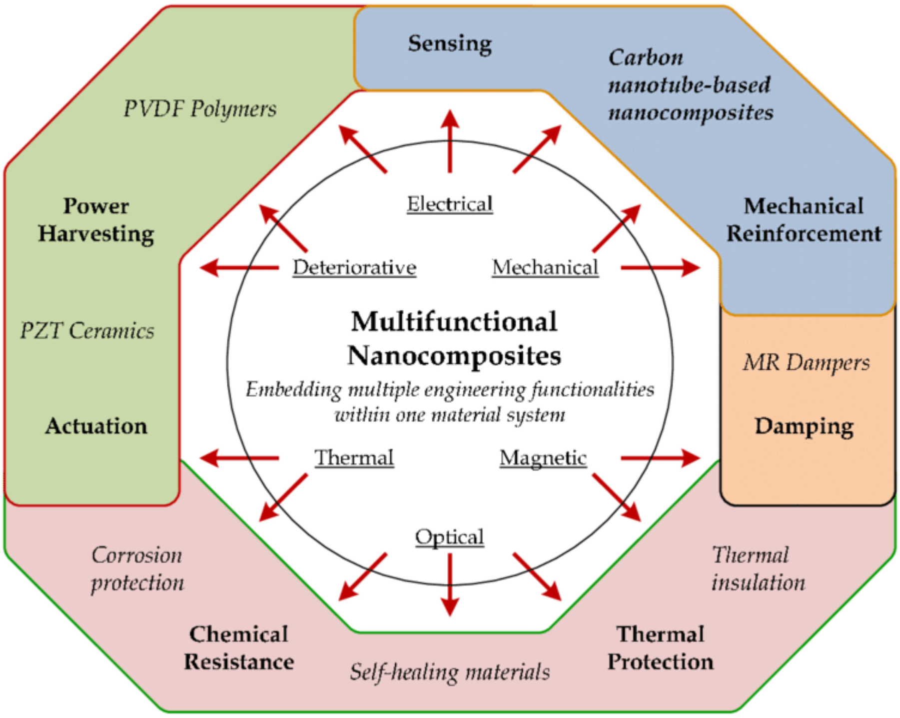

Figure 1. *3 The concept of multifunctional nanocomposites, the properties imparted, and applications areas [11].*

It is essential to understand the problem, and which functions are required to design such a multifunctional material. After that, it is possible to make a specific design for this application using specific material combinations and/or surface functionalisation techniques. For example, outdoor electronic equipment, such as signal stations, radar units, and cellular base stations, play a vital role in modern human life to provide safety and communication. One of the critical issues they experience is ice accretion, reducing their efficiency and shortening service life. Another problem with this kind of equipment is its potential to create electromagnetic waves. Some studies have linked long-term exposure to electromagnetic waves with cancer, childhood leukaemia, central nervous system disorders, and depression [12-14]. Nanocomposite layers having both electromagnetic shielding properties and icephobicity, can be designed and produced to solve ice accretion and electromagnetic pollution problems.

Electrospun nanofibre membranes are of great interest due to their unique properties, such as their lightweight, flexibility, breathability, the possibility of using other materials to prepare nanocomposite structures, and ease of processability. Most soluble polymers are suitable for the solution electrospinning process, which provides more expansive applications for electrospun membranes. Recently, researchers have focused on advanced applications of electrospun membranes.

This work focuses on exploring the potential of electrospinning as a versatile method to produce nanofibre membranes with a high surface-to-volume ratio, high porosity interconnected open pore structures, and adjustable pore sizes, to fabricate superhydrophobic and icephobic surfaces. We seek to explain the mechanism behind the properties, achieved by investigating the microstructural and performance properties of fabricated electrospun membranes.

1.2 Research Aims and Objectives

The aims of this work are (i) to explore the potential of using the electrospinning method to produce functional nanofibre membranes for superhydrophobic and icephobic applications, (ii) to investigate the possible mechanisms behind the properties achieved, and (iii) to design and produce nanocomposite nanofibre electrospun membranes using functional nanofillers, for specific applications that require multifunctionality.

The key objectives of this research are proposed as follows:

- To use the electrospinning method to fabricate nanofibre membranes having specific surface roughness and >150° of water contact angle.
- To investigate the role of electrospinning variables on surface morphology and wettability of the electrospun nanofibre membranes.

- To fabricate electrospun nanofibre membrane-based slippery liquid infused porous structure (SLIPS) having low ice adhesion strength (<50 kPa) and high transparency (>90%).
- To study the microstructural and performance properties of SLIPS prepared and to explore the mechanism of electrospinning and transparency achieved.
- To design and fabricate multifunctional nanofibre membrane combining superhydrophobicity (>150° of water contact angle) icephobicity (<50 kPa) and high EMI shielding efficiency (>99%) for outdoor EMI shielding applications.
- To investigate the possible mechanisms behind the properties achieved by investigating microstructural properties of multifunctional nanofibre membranes.

CHAPTER 2

Literature Review

2.1 Electrospinning

2.1.1 Background of Electrospinning

The first observation of the electrostatic attraction of liquids was made by William Gilbert in 1600 [15]. He used an electrically charged piece of amber for this experiment and found that when it was brought near a droplet of water, its shape changed to a small cone, and it was possible to eject tiny droplets from the tip of this cone. This process was defined as “electrospraying”. After this study; in 1885, Lord Raleigh described the amount of the charge required for changing the shape of the droplets [16], and after 20 years of this milestone, J.F. Cooley and W.J. Morton designed an apparatus for spraying by using electrically charged droplets, which they patented [17].

In 1914, John Zeleny, wrote a mathematical model to understand the behaviour of a droplet under electrostatic forces. He also investigated that the fine fibre-like liquid jets could be ejected from electrostatically charged liquid droplets [17]. This work can be considered as the origin of the electrospinning systems. Professor Kiyohiko Hagiwara produced artificial silk fibres using an electrospinning system in 1929, and he called the produced material “lineal or fibrous sol” [18].

In 1934, Anton Formhals filed a patent describing a practical apparatus to produce artificial fibres using an electrical field (Figure 2.1). After this patent, many people filed a series of patents, which consisted of improvements and modifications to this system [19].

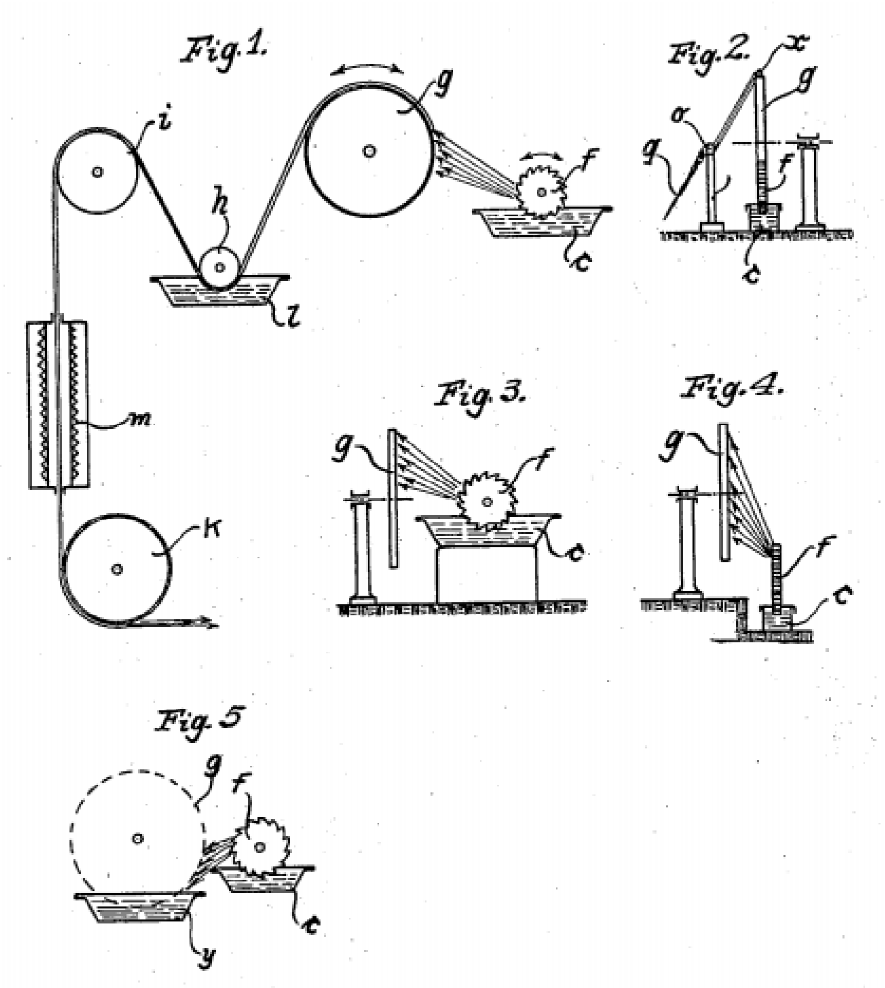

Figure 2.1 *Schematic illustration of the patented apparatus by Anton Formhals [19, 20].*

In 1936, Charles Norton from the Massachusetts Institute of Technology filed a patent about melt electrospinning working with an air blast. Larrondo and Manley published three scientific papers about melt electrospinning in 1981 in which they used poly (ethylene) and poly (propylene) [21].

In the 1960s, British physicist and mathematician Geoffrey Ingram Taylor explained electrospinning theoretically [22]. This work was critical because it was about modelling the shape of the cone, which occurred after an electrical threshold under the effect of these electrical forces. This characteristic shape is now referred to as “Taylors Cone” (see Figure 2.2).

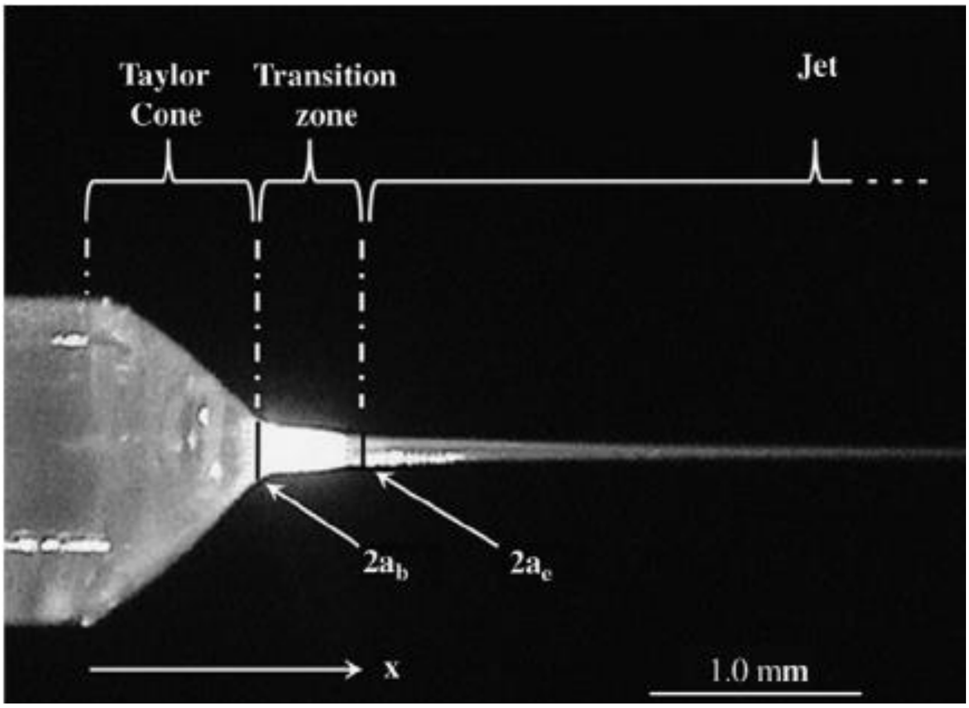

Figure 2.2 *Schematic illustration of Taylors cone [23].*

After these improvements and investigations, many scientific researchers published papers on nanofibres production by electrospinning. After the 1970s, some companies, such as Bayer filed a series of patents to commercialize this technique. The first technical application of nanofibre membranes was for the nonwoven industry, as air filters. Today, the applications of electrospun nanofibre membranes have enlarged dramatically, and commercial products in air filtration, medical applications, and functional textiles are available on the market. The current applications of electrospun nanofibres are given in Figure 2.3. Although electrospinning is a well-researched and developed technique, it is fascinating to combine it with other functionalization techniques to find advanced applications.

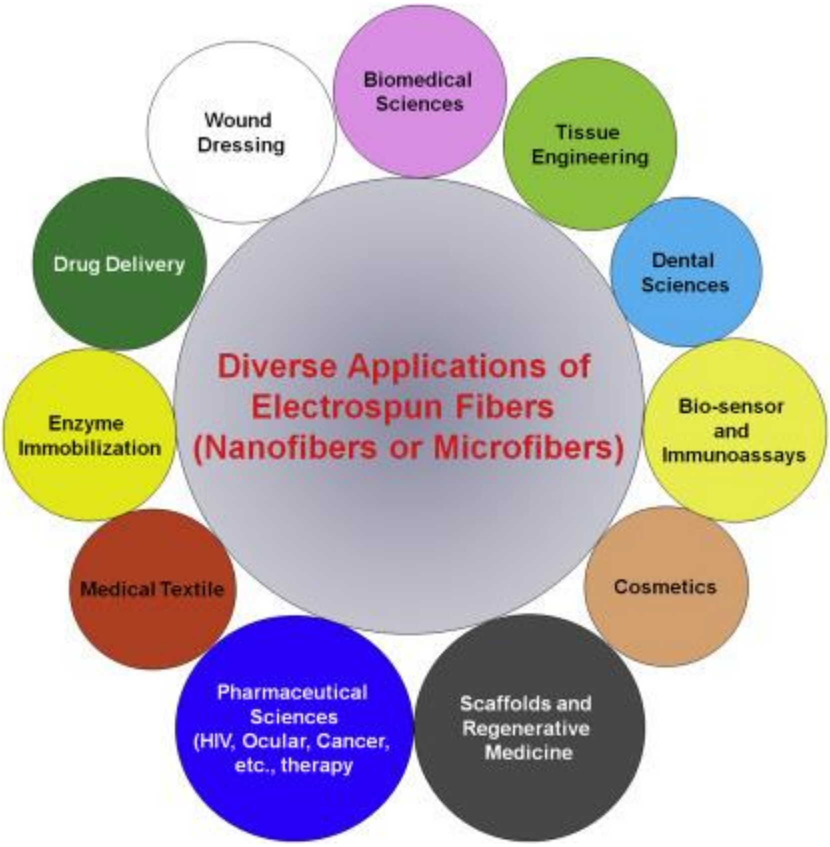

Figure 2.3 *Current applications of electrospun nanofibres [24].*

Due to their extremely high surface area and porosity, electrospun nanofibres have broad application areas such as filtration [25], tissue engineering [26], wound healing [27], energy storage [28], sensors [29], hydrophobic coatings [30], and more. Some companies and their commercially available products are given in Table 2.1. It should be also noted the number of companies and application areas they proposed are growing sharply day by day.

Table 2. 1 *Some electrospinning companies and their commercial products [31].*

Name of Company	**Commercially Available Products**
Elmarco	Nanospider™ (lab to industrial scale)
Revolution Fibres Ltd	Seta ™ (air filtration), Phnoix ™ (acoustics), Xantu. Layr™ (composite reinforcement), ActiVLayr ™ (skin care and health), nanodream ™ (bedding)

Finetex EnE, Inc	Technoweb ™ series X, V, R, Pro and Filtrepro (air and liquid filtration), Technoweb ™ C series (cosmetics), Finemask® (facial mask), Nexture ™ (technical textiles)
Xanofi	XanoLoft ™ & XanoRail ™ (air filtration), QuietMat ™ (acoustics), XanoMatrix ™ (cell culture), XanoCapture ™ (protein purification)
eSpin Technologies	Exceed® and nWeb™ filters (air filtration), SIMWyPES® (high-performance wipes), technical textiles, nanofibre culture substrate, filtration media
SNS Nano Fiber Tehcnology, LLC	NANOSAN® (super absorbant pad)
NANO-FM B. V.	Cell scaffold
nanoScaffold Technologies, LLC	Cell scaffold
nanomyp	Tiss® Series (nanofibre tissues)
Welcron Co., Ltd	Technical textiles, wound dressings and medical textiles, heat exchanging element
Amofiber	Amotex® (technical textiles), nanofibre membranes for energy storage, fluid filters
BMCbio Co., Ltd	MEDIWIZ Natural Mask Pack, Wipes
Wooree Nanophil Co. Ltd	Battery separator, technical textiles, high-efficiency filtration media
Hirose Paper MFG Co. Ltd	A range of composite nanofibre non-woven textile
FiberTrap	Insect/bug barrier for bedding and textiles
SPUR a.s.	SpurTex (air filter media), SPIN Line (nanofibre production line)

The primary advantages of the electrospinning process and electrospun membranes, which provide many application areas, are given as follows.

- Cost effectivity
- Tailorable pore sizes
- Adjustable fibre diameters and surface areas
- Easy to apply in a wide of polymers

- Larger sample sizes compared to other techniques
- Ability to provide hybrid, coaxial or side-by-side structures

2.1.2 Electrospinning Process

The standard mechanical fibre producing processes, such as melt, wet, or gel spinning, are not considered as techniques suitable for producing sub-micron fibres [32]. Although there are several techniques to prepare sub-micron fibres, electrospinning has come to the forefront because it is economical, easy, and suitable for large productions.

A basic electrospinning system consists of a high voltage supplier, feed pump with a syringe and needle, and a collector [16], as shown in Figure 2.4.

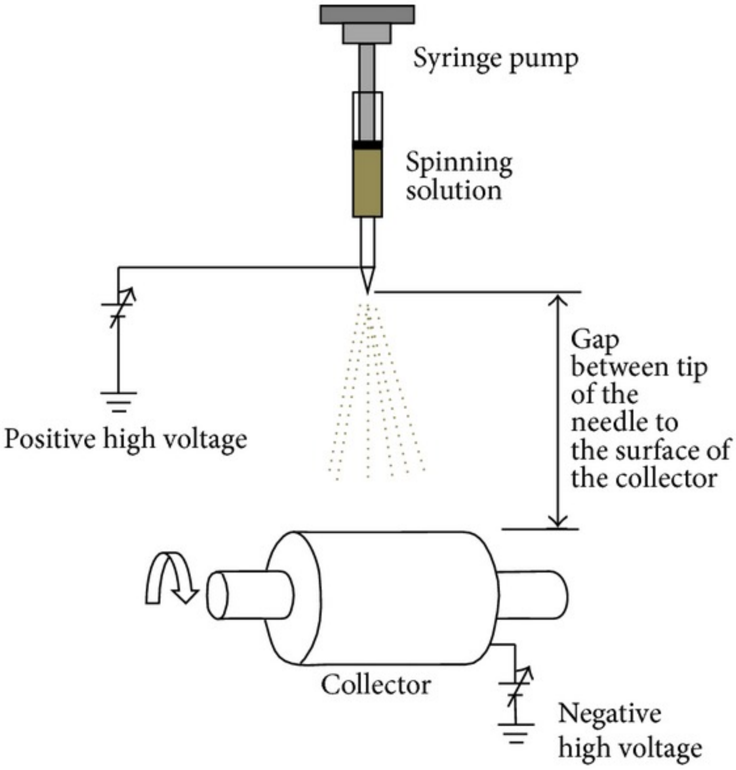

***Figure 2.4** Schematic illustration of a basic electrospinning set-up [33].*

According to Garg *et al*. [34], the principle of the electrospinning process consists of three main stages; formation of a jet, thinning of the jet, and solidification of the fibres.

a) Formation of a jet

Taylor investigated that when a sufficient electrical field was applied to the polymer droplet, its shape was changed to form a cone [34]. When the power of the electrical field reached the critical threshold, electrostatic forces overcame the surface tension of the solution, and a spinning jet formation occurred at the tip of the Taylor cone, which is also the point with the highest charge density.

According to Taylor [22], the threshold value can be calculated from the following formula;

$$Vc^2 = 4(\frac{H^2}{L^2})(\ln\frac{2L}{R} - 1.5)(0.117\pi R\gamma) \qquad \textit{(Eq. 2.1)}$$

Where Vc^2 is the voltage threshold (kV), H is the air-gap distance (cm), L *is the* length of the capillary tube (cm), R is the radius of the tube (cm), and γ is the surface tension of the polymer solution (dyne/cm).

b) Thinning of the jet

Solution concentration, electrical field, flow rate, and jet velocity significantly affect the electrospinning process [34]. When a low molecular weight polymer is used for electrospinning, the deformation of the polymer jet mostly depends on the flow rate. If the flow rate is not sufficient, the jet will disappear quickly. When it is higher than the optimum value, then the jet will decay slowly. In 2006, Deitzel *et al*. [35] published a study that explained this phenomenon using a simple cylindrical geometry as the electrospinning jet (Equation 2.2). According to Deitzel *et al*., the ratio of surface area to volume (specific surface area) was proportional to the inverse of the jet radius. This means that when the specific surface area increases, the radius of the jet will decrease sharply, and when the volume increase, the radius of the jet will also increase [35].

$$\frac{A}{V} = \frac{2}{R} \qquad \textit{(Eq. 2.2)}$$

Where *A* is the specific surface area, *V* is volume, and *R* is the radius of the jet.

Assuming the polymer solution and the surface charge density are constant, then the charge-to-mass ratio will decrease with increasing jet radius. As seen in Equation 2.3, the acceleration is directly proportional to the ratio of the charge to mass. Thus, an increase in jet radius results in a decrease in the acceleration of the fluid.

$$a = E(\frac{q}{m}) \qquad \textit{(Eq. 2.3)}$$

Where *a* is Acceleration, *E* is Electrical field, *q* is the available charge for a given volume element, and *m* is the mass of a given volume element.

This simplified model of a cylinder was only meant to provide a gross illustration of the interaction between the solution feed rate, electrospinning voltage, and the charge to mass ratio. The results of the Deitzel *et al*. were coherent with the Baumgarten`s work [36]. His work in 1971 showed that when both voltage and feed rate increased, collected fibre diameter initially decreased, reached a minimum diameter, and then increased.

c) Instabilities of the jet

When the polymer jet is sprayed from the tip of the Taylor cone, it is subjected to a variety of forces that create some instabilities [35-37]. The polymer jet may create splitting called splaying or branching. The main reasons for this branching and splaying are changing the shape of the jet and charge per unit area due to the evaporation of the solvent. Then, the balance of the electrical field and surface tension deteriorates, which is the starting point of an unstable polymer jet. To decrease the local charge of the surface area, an unstable jet forces out smaller jets from the surface of the main polymer jet. More concentrated and viscous polymer solutions can cause this kind of branching under very high electrical fields.

Non-axisymmetric or whipping instability is one of the most important parameters to decrease fibre diameter from micrometre to nanometre. When the fibre diameter is very thin and fibres very long, it takes much more time for the excess charge to redistribute itself along the entire length of the jet. Then, the location of the excess charge changes because of the elongation of the fibre. The Coulomb forces between the charges carried with the jet elongate on its axis until the jet solidifies. This situation creates a fantastically high velocity at the end of the fibre jet and causes jet bends (Figure 2.5).

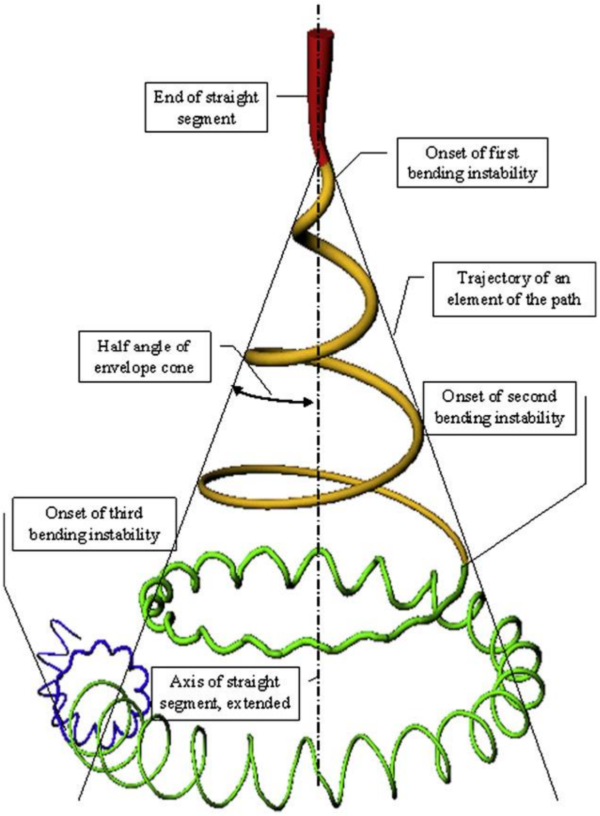

Figure 2.5 *Schematic illustration of instabilities of polymer jet [37, 38].*

According to Hohman *et al*., there are three types of instabilities in the fibre jet [39], Rayleigh instability which occurs due to opposing forces acting on the surface area of the jet, axisymmetric instability, and whipping instability which caused by the bending forces.

d) Solidification of the polymer jet

Solidification of the polymer fibre is mainly related to the evaporation of the solvent and crystallization of the polymer chains [34]. Solidification rates during electrospinning depend on the polymer concentration, electrical field, and collector-needle distance. In 2001, Yarin *et al*. developed an equation to calculate the polymer jet's mass loss and volume change caused by evaporation of the solvent and solidification. However, they assumed that there was no branching or splitting from the main jet. They also reported that the diameter of the solidified fibres was 1310 times lower than the initial jet. The effect of the solidification step on the initial jet is given in Figure 2.6.

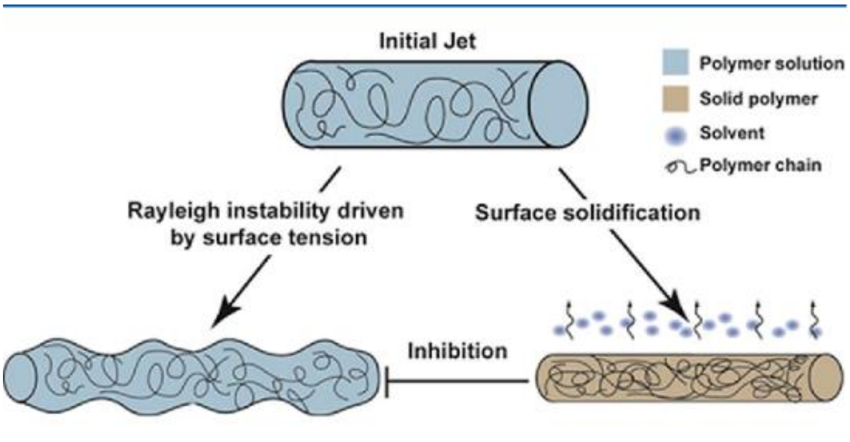

Figure 2.6 *Solidification of the initial jet, the effect of Rayleigh instability on the surface morphology and the change in diameter with solvent evaporation [40].*

2.1.3 Variations of Electrospinning Setups

For the production of core-shell nanofibres, a coaxial electrospinning method was developed [41]. This novel method utilizes two intertwined needles. Feeding two different materials into the coaxial needle made it possible to produce coaxial fibres with unique properties such as self-healing ability or improved mechanical properties. It was also possible to have hollow fibres using this method. A schematic illustration of a coaxial spinning system and needle is given in Figure 2.7. The first publication for coaxial electrospinning was made by Sun *et al*. in 2003 [41]. They produced coaxial fibres for the first time using a combination of two different polymers.

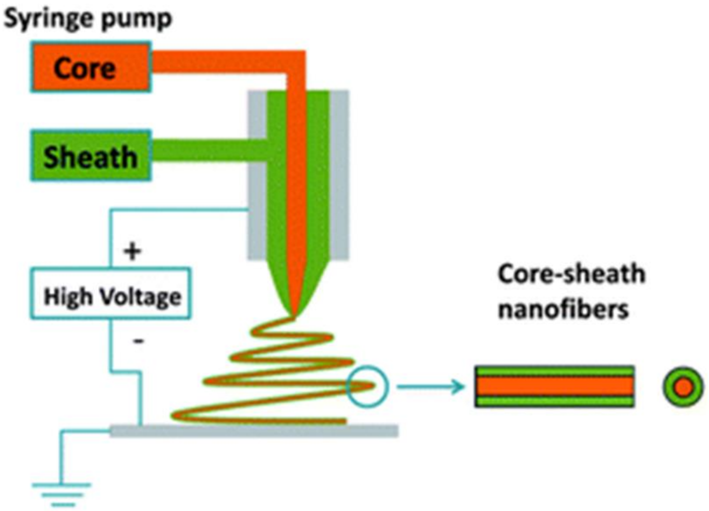

Figure 2.7 *Schematic representation of coaxial spinning system [42].*

Mixed electrospinning enables the production of electrospun membranes with two or more components. The main advantage of this modification is the ability to control the processing conditions of different components. This method was first used by Kiodaki *et al*. [43] to produce nanofibre scaffolds which include three different polymers. After this work, many other results were published by the researchers. Figure 2.8 illustrates the schematic representation of a multilayer or mixed electrospinning setup.

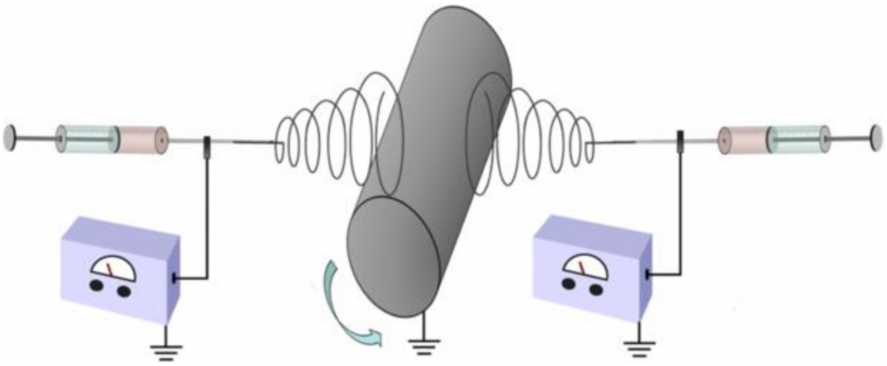

Figure 2.8 *Schematic representation of multi-nozzle spinning system [44].*

Another approach to producing multi-component electrospun networks is side-by-side electrospinning. In this method, it is possible to control the feed ratio for each component. However, it is not possible to control other processing conditions, such as electric field and collector distance. Similar to the coaxial method, two or more components are fed into the same needle, but they are located side by side instead of intertwined. Figure 2.9 shows the schematic illustration of the side-by-side electrospinning.

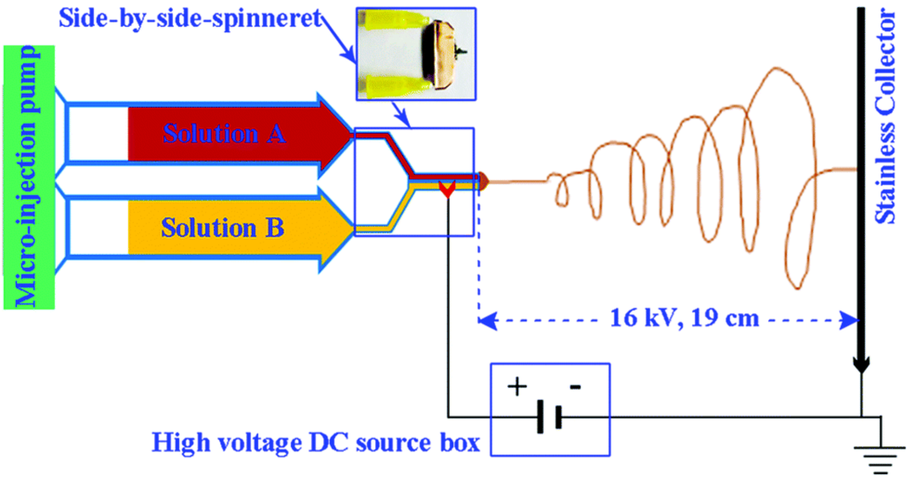

Figure 2.9 *Schematic representation of side-by-side spinning system [45].*

To provide a large deposition area, produce specific membranes with highly aligned fibres or modified fibre surfaces, electrospinning collectors also are of great importance. There are many novel collector types for electrospinning; some common ones are given in Figure 2.10. For example, it is possible to obtain aligned fibres using rotating drum collectors with larger deposition areas depending on the diameter of the cylinder. There are many works published using a rotating drum collector type in almost every application area. Parallel electrode collectors can also provide highly aligned fibres, but the distance of the electrodes limits the deposition area. Arrays of counter electrodes type collectors were also designed to obtain sieve-like structures.

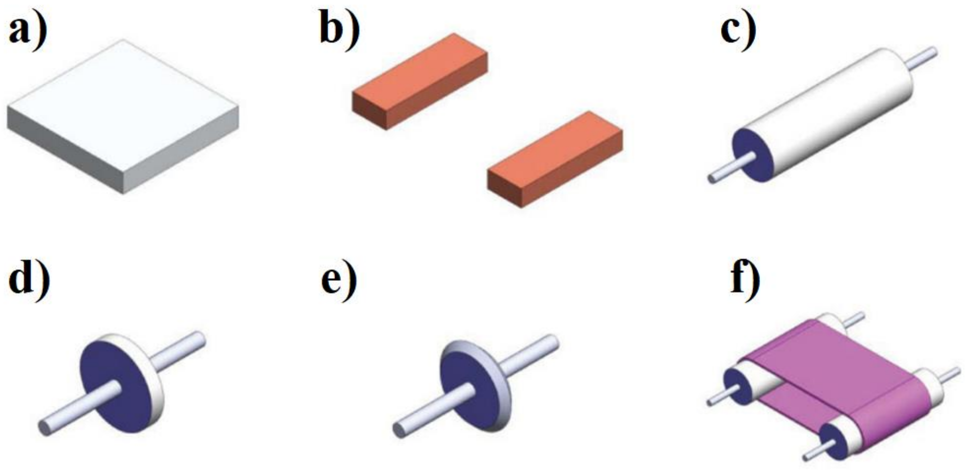

Figure 2.10 *Some types of electrospinning collectors (a) flat plate, (b) parallel plates, (c) rotating drum, (d) rotating disc with a flat edge, (e) rotating disc with a sharp edge and (f) conveyor [46].*

2.1.4 Parameters of Electrospinning

Primarily, the parameters and the potential effects of each parameter on the properties and morphology of polymer membranes are stated in Table 2.2 [16]. More information about the impact of the parameters on the properties and morphology of the membranes will be discussed in the following sections.

Table 2.2 *Effect of parameters on fibre morphology.*

	Parameters	**Effect on fibre morphology**	**Ref.**
Solution parameters	Viscosity	Increasing viscosity provides fewer beads and a smooth fibre structure.	[47-50]
	Polymer concentration	An increase in the concentration of polymer cause a larger diameter of fibres.	[51, 52]
	The molecular weight of the polymer	The increasing molecular weight provides beadles, smooth fibres.	[53, 54]
	Conductivity	Increasing conductivity can cause beads but also provide thinner fibres.	[47, 55]
	Surface tension	Increasing surface tension leads to more instability of the polymer jet.	[56, 57]
Processing parameters	Applied voltage	Increasing voltage provides thinner fibres because of the increasing velocity of the polymer jet.	[51, 55]
	Distance between tip and collector	The lower distance can cause wet fibres; the optimum distance should be chosen.	[58-60]
	Flow rate	A higher flow rate can cause unspun droplets; the lower flow rate cannot provide continuous fibre production.	[61]
Environmental parameters	Humidity	The diameters of the fibres decrease with the increasing humidity.	[62, 63]
	Temperature	It affects the viscosity of the solution and evaporation rate. Higher temperatures provide thinner fibres.	[63]

2.1.4.1 Solution Parameters

a) Concentration and viscosity of electrospinning solution

To fabricate continuous nanofibres by using electrospinning, solution parameters, especially concentration, have great importance. It was reported that for polyacrylonitrile when the concentration of the solution was too low (lower than 18% wt.), microbeads and bead-on-string fibres were formed instead of smooth nanofibres [64]. Higher concentrations also caused a problem because of the increased viscosity. For polyacrylonitrile, it was difficult to feed the polymer solution when the concentration was higher than 26% wt. So, there is an optimum range for polymer concentration for electrospinning depending on the types of polymer, molecular weight, and solvent. Some papers published also reported that increasing concentrations caused a larger diameter of fibres [36].

Viscosity, another essential solution parameter for electrospinning, plays a critical role in nanofibres' diameter and surface morphology. Similar to concentration, when the viscosity is low, no fibre formation occurs. Moreover, ejecting the electrospinning solution through the needle can be challenging when high-viscosity solutions are used. As a result, an optimum range of viscosity is suggested by Baumgartner *et al. [36]*. They investigated the effect of viscosity on the fibre formation of poly (acrylonitrile) solutions. They found that it was possible to produce continuous nanofibres between the viscosities of 0.17 to 21.5 newton second/square meter. They also reported that the increasing viscosity caused increasing fibre diameter. The effect of increasing viscosity on polymer jet formation is summarised in Figure 2.11.

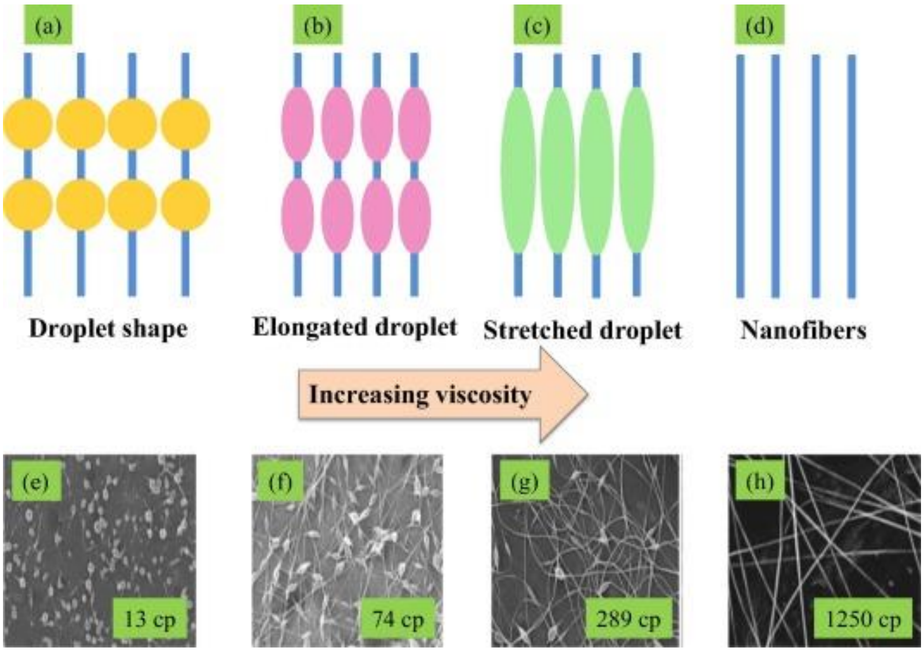

Figure 2.11 *Effect of increasing viscosity on polyacrylonitrile electrospun nanofibres (with polymer viscosity of 13 cp (a, e) 74 cp (b, f) 289 cp (c, g) and 1250 cp (d, h)) [65].*

b) Electrical conductivity of the electrospinning solution

Most synthetic and natural polymers have non-conductive nature. For the electrospinning process, the conductivity of the solution is determined by the nature of the polymer, conductivity of the solvent used, and the presence of ionizable salts [65]. Some studies showed that the increased conductivity of the electrospinning solution leads to thinner fibre structures, while lower conductivities provide beady structures because of the insufficient elongation of the polymer jet. Tan *et al.* [66] explored the effect of electrospinning solution conductivity on P(LLA-CL) nanofibres and they found that when the solution conductivity was 0 Ω^{-1}, fibre diameter obtained was around 300 nm and it decreased to around 100 nm when the conductivity of the solution increased to 13 Ω^{-1}. However, it was also reported that when the electrical conductivity of the polymer solution is significantly high; it results in unstable polymer jets under high voltages [65]. Thus, it causes dramatic bending instability, which affects the broader diameter distribution.

c) Surface tension and volatility of the solvent used

The surface tension of electrospinning solutions, which is strongly related to the solvent, is also an important parameter for electrospinning. In general, higher surface tension limits the electrospinning process and causes bead formation instead of fibres because of polymer jet instability [65]. Besides, lower surface tension provides electrospun nanofibre at lower electrical fields. Bead, droplet, or nanofibre formation is mainly about the surface tension of solutions.

The volatility of the solvent also has a significant impact on fibre formation. The solvent should have a moderate boiling point and volatility for the electrospinning process. When the volatility of the solvent is low, the fibre formation can not be completed between the tip of the needle and collector, and a smooth film morphology will be obtained instead of the fibrous membrane. On the other hand, if the volatility of the solvent is dramatically high, it can evaporate before spinning, which may cause a blocked needle [65].

2.1.4.2 Process Parameters

a) Applied voltage

It is well known that when high voltage is applied to a polymer droplet; it causes the formation of the Taylor cone, and then fibre spinning occurs at the tip of the cone at the critical voltage value. This threshold mostly depends on the polymer and solvent used. Below this threshold, it is not possible to obtain fibre. However, some morphologic changes can be seen on the nanofibre membrane when the voltage increases after this critical value. Deitzel *et al.* investigated the effect of voltage on the morphology of the polyethylene oxide (PEO) nanofibres. They reported that increasing voltage below the optimum point might cause beady structures for PEO. Meechaisue *et al*. [65] also studied the effect of the voltage on the fibre properties, and they found that increasing voltage results in fewer beads. However, the diameter of the fibres also increases with the increasing voltage. This is because of the effect of applied voltage on the size of the jet length. Tepsorn *et al.* investigated the effect of applied voltage on the chitosan-cellulose acetate-gelatin hybrid nanofibres and showed that the average fibre diameter of nanofibres decreased from 170 to 100 nm when the applied voltage increased from 20 to 25 kV. When higher voltages are applied, the length of the jet becomes larger, and it affects the diameter of the fibres with the same trend. The effect of the voltage on the droplet is shown in Figure 2.12.

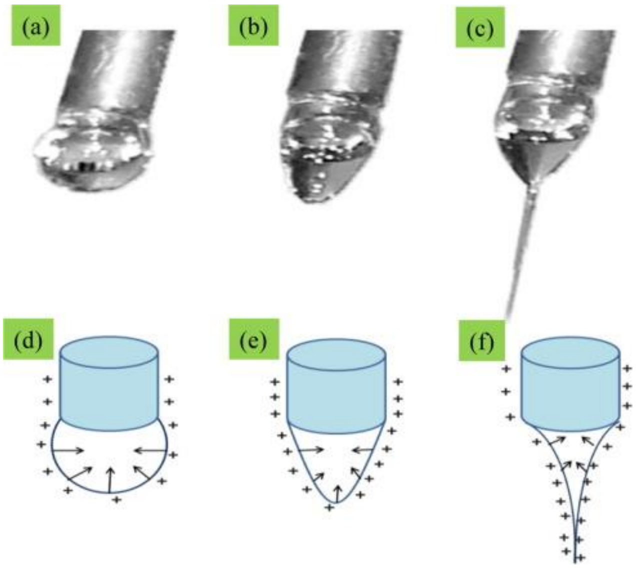

Figure 2.12 *Effect of increasing voltage to the droplet shape (a-c) and schematic representation of droplet deformation with increasing voltage (d-f) [65].*

b) Solution flow rate

The flow rate of the electrospinning solution also has an important impact on fibre size, fibre shape, and porosity. The flow rate should be optimized to protect the shape of the Taylor cone; otherwise, it will disappear by the ejected fibre from the droplet and evaporation of the solvent. Using the optimum value of the flow rate can contribute to continuous smooth fibre production. Megelski *et al.* [67] investigated the effect of the flow rate on fibre size and shape using poly (styrene). As a result, they found that the fibres' diameter and porosity increased with higher flow rate values. Higher flow rates also can cause bead formation due to the inability of the fibre to dry completely before being collected. Additionally, higher flow rates may cause unspun droplets and ribbon-like defects to form due to the contribution of gravitational forces [67, 68].

c) Needle to collector distance

Distance between the tip of the needle to the collector also has an essential role in the electrospinning process due to its effects on the morphology of nanofibres. The optimum distance also depends on the polymer and solvent used. The structure and morphology of electrospun fibres are easily affected by the needle-to-collector distance because of their dependence on the deposition time, evaporation rate, and whipping or instability interval [65, 69]. Lesser distances can cause wet fibres or beads due to the inability of solvent evaporation with this limited distance [51]. Many studies were carried out to understand the effect of the distance between the needle tip and collector and concluded that defective and large-diameter nanofibres are formed with decreasing distances. In contrast, the nanofibre diameter decreased as the distance was increased [36, 70].

2.2 Environmental Parameters

Environmental parameters, temperature, and humidity have an important effect on the diameter and morphology of the electrospun nanofibres. The solidification step of the jet can be influenced easily by humidity. However, it also depends on the chemical nature of the polymer used. The impact of the humidity on the diameter and morphology of the PVA and PEO nanofibres was studied by Pelipenko *et al*. [62]. They showed that the fibre diameter dramatically decreased from 231 nm to 41 nm with the increasing humidity. Besides, they also confirmed that defects and beads could occur after 60% of relative humidity, and even the electrospinning process may be interrupted if the relative humidity gets increased more.

The temperature has two primary impacts. The first is increasing the evaporation rate of the solvent, and the second is its effect on the viscosity of the polymer solution. Both effects can provide a smaller diameter for fibres. Similar results were observed by Vrieze *et al*. [63] using PVP and CA.

2.3 Hydrophobicity and Theory of Hydrophobic Effects

The wettability of a solid surface is an important feature, due todifferent application areas require different wettability of the surfaces. There are two basic requirements to define a surface as superhydrophobic. The first of these requirements is the high water contact angle (typically over 150°). The second is low contact angle hysteresis, which can be described as the required activation energy for the movement of a droplet from one metastable state to another on a solid surface, typically lower than 10°, which indicates that the droplet has good mobility on the surface. There are many examples of superhydrophobic surfaces in nature. The most known one, *Lotus Leaf*, can easily repel water when it is raining with minimal tilt angles due to an excellent combination of surface chemistry and roughness. There are many more examples from nature, such as insects, plants, or even living microorganisms.

For the superhydrophobicity, there are two main parameters: 1) The roughness of the surface and 2) The chemical composition of the material [71]. Lotus leaf has a very tiny, hairy structure on it, which contributes the hydrophobicity. The effect of the surface structure on the contact angle is shown in Figure 2.13. As seen from Figure 2.13, considering all samples having the same chemical composition, the flat sample has the lowest water contact angle value and by texturing the surface in nano-micro scale, it is possible to achieve higher contact angle values.

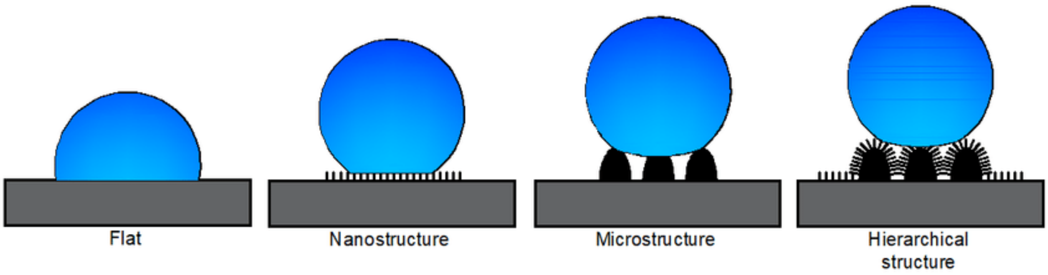

Figure 2.13 *Effect of surface topography on the contact angle [71].*

The chemical composition of the material is also essential because this feature directly influences the surface tension of the surface, which has a critical role in the surface's wettability [71].

2.2.1 Contact Angle and Young's Equation

To quantify the wettability of a solid surface, it is possible to use contact angle measurement methods, which are based on a simple measurement of the contact angle between a solid surface and droplet. Young's equation, presented in 1805, has been used as a basic equation. However, it has quite limited applications due to the necessity of a perfect surface, which is solid, purely flat, non-soluble, inert, and chemically homogenous. This surface theoretically has a contact angle of 0°. The following Young's equation can describe the contact angle of a liquid droplet on the surface:

$$\gamma_{sv} = \gamma_{sl} + \gamma_{lv} \cdot \cos\theta \qquad \textit{(Eq. 2.4)}$$

Where γ_{lv} is the surface tension of the liquid, γ_{sl} is the interfacial tension between the liquid and solid, γ_{sv} is the surface free energy of the solid and cosθ is the contact angle between γ_{lv} and γ_{sl} [72]. The schematic representation of Young`s equation is shown in Figure 2.14.

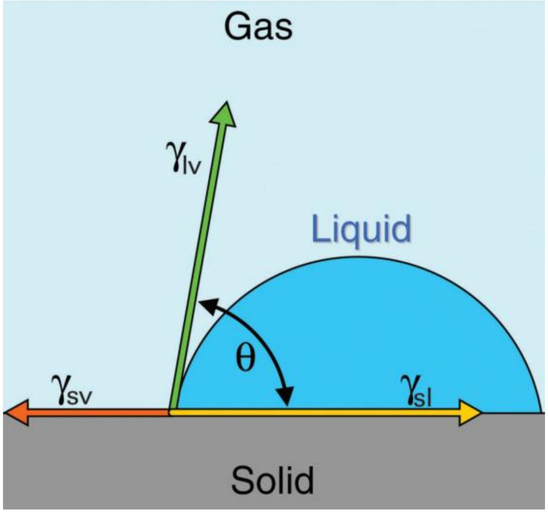

Figure 2.14 *Schematic illustration of Young`s equation (γ is the surface tensions between the three phases) [72].*

However, as mentioned, this model is not for actual surfaces but ideal surfaces. Because the actual surfaces are not ideal, other models were developed for actual surfaces.

2.2.2 Contact Angle Models for Actual Surfaces

Two different models were developed to describe the contact angle for non-ideal or actual surfaces: Wenzel Model and Cassie-Baxter Model. It is always possible for the actual surfaces to have heterogenic chemical structure and surface roughness. Contrary to Young`s equation, the Wenzel Model considers the roughness of the surface and assumes that the surface has a homogenous chemical structure. On the other hand, the Cassie-Baxter Model, unlike Wenzel, considers that there is no roughness, so the surface is flat but with chemical heterogeneity [2].

In the Wenzel model [73], the surface roughness (r) is defined as the ratio of the actual area to the projected area of the surface. The equation of the Wenzel model can be written as follows,

$$cos\ \theta = r \cdot \cos(\theta_y) \qquad \text{(Eq.2.5)}$$

Where θ is the apparent contact angle and θ_Y is the equilibrium contact angle from Young's equation on an ideal solid without roughness. In the Cassie-Baxter model, f1 and f2 are solid and air area fractions under a droplet on the substrate. The Cassie-Baxter equation can be written as:

$$\cos(\theta^*) = f_1 \cdot \cos(\theta_Y) - f_2 \qquad \textit{(Eq.2.6)}$$

Where θ^* is the apparent contact angle and θ_Y is the equilibrium contact angle on the solid.

From the Wenzel model, it can be deduced that the surface roughness amplifies the wettability of the original surface. Hydrophilic surfaces become more hydrophilic, and hydrophobic surfaces more hydrophobic. In the Cassie-Baxter model [74], the area fractions under the droplet are important, and the larger the area fraction of air provides, the higher the contact angle (Figure 2.15). Although these two models were proposed half a century ago, they are still widely used with active research on superhydrophobic surfaces.

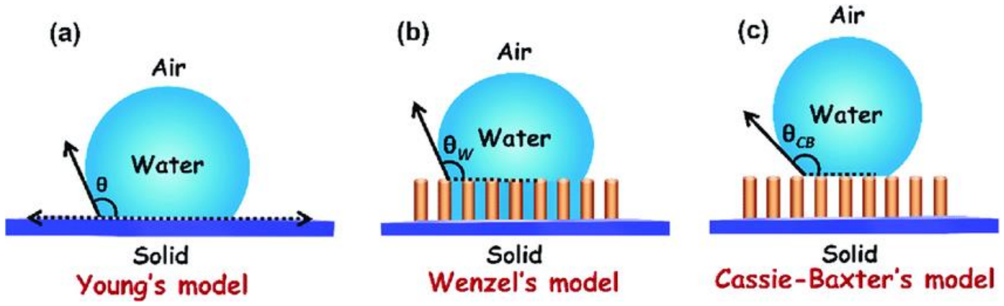

***Figure 2.15** Schematic illustration of Young`s (a), Wenzel (b) and Cassie-Baxter (c) Models [75].*

2.2.3 Contact Angle Hysteresis

Contact angle hysteresis is an important and frequently used concept to describe the wettability of a surface as it provides information on the required activation energy for the movement of a droplet from one metastable state to another on a solid surface. To calculate the contact angle hysteresis, advancing and receding contact angles need to be measured, known as the dynamic contact angles. To measure the advancing contact angle of a surface, first, the needle of the contact angle measurement system should be as close as around 1 mm to the surface. After that, the water droplet is injected onto the surface at a constant flow rate. While the volume of water droplet increase, the contact area between the droplet and surface also increases. The change in contact angle with the increasing drop volume is referred to as \`advancing contact angle\` as described in Figure 2.16a.

The receding contact angle is the exact opposite of the advancing contact angle. The liquid is removed from the droplet at a constant rate to measure receding contact angle, resulting in the droplet's decreasing volume. While the droplet volume decreases, the contact area between the droplet and surface is expected to get smaller, as described in Figure 2.16b. The following equation can be used to calculate the contact angle hysteresis using advancing and receding contact angles:

$$CAH = \theta_{Advancing} - \theta_{Receding} \qquad \textit{(Eq. 2.7)}$$

Where *CAH* is the contact angle hysteresis, $\theta_{Advancing}$ is the surface's advancing contact angle, and $\theta_{Receding}$ is the receding contact angle.

The contact angle hysteresis mainly has two components, thermodynamic and dynamic. The thermodynamic component is related to the roughness and chemical heterogeneity of the surface, while the dynamic one is about the chemical interaction between the surface and water droplet and the ability of the droplet to penetrate inside the pores of the surface.

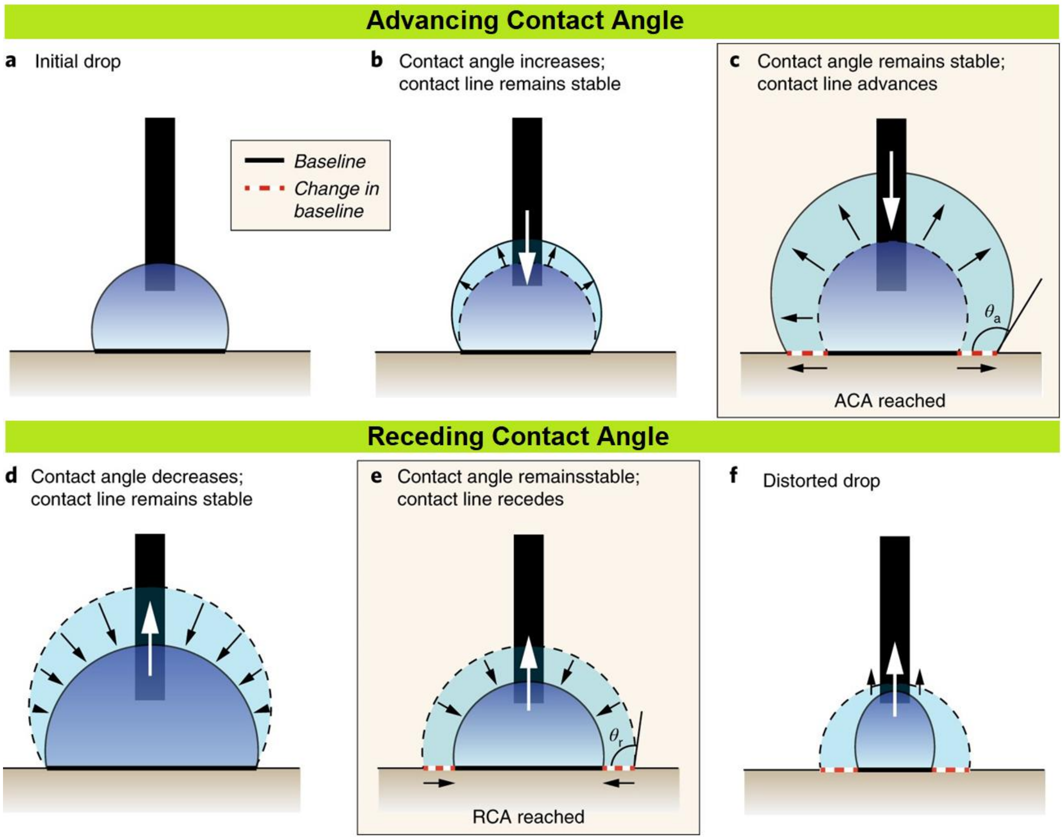

Figure 2. 16 *Measurement of Advancing(a-c) and receding (d-f) contact angles and their different stages [76].*

2.3 Materials and Production Methods of Superhydrophobic Surfaces

It is significantly essential to control the wettability of the surfaces for many areas of the technology. Superhydrophobic surfaces, which exhibit higher than 150° of water contact angle and contact angle hysteresis lower than 10°, have unique advantages such as the self-cleaning effect, a critical feature for photovoltaic panels, satellite dishes, and architectural glasses. They can also impart the ability to prevent ice from forming or adhering to the surface [77].

There are mainly two methods to prepare superhydrophobic surfaces; the first is to use low-surface energy material to prepare a rough surface. This technique makes it possible to produce superhydrophobic surfaces in just one step, which may be cost-effective and suitable for rapid production. The second method is to prepare a rough surface using the proper techniques and then modify the surface with low-surface tension materials [77].

2.3.1 Commonly Used Materials for Superhydrophobicity

Some of the common methods to produce superhydrophobic surfaces are summarized in Table 2.3. As seen, the formation of the surface roughness and hydrophobization of the surface are key steps to preparing a superhydrophobic surface.

Table 2. 3 *Superhydrophobic surface preparation methods [78].*

Method	**Roughness Formation**	**Hydrophobization**	**Ref.**
Covalent layer-by-layer assembly	Nanoparticle-induced micro or nanostructure	Using low surface energy chemicals	[79-82]
Polymer film roughening	Phase-separation-induced porous structure of the multicomponent mixture	Using hydrophobic polymers	[83-86]
Chemical vapour deposition	Growth of nanostructures by polymerization	Polymerized structure itself	[87]
Hydrothermal synthesis	Hydrothermal growth of nanostructures	Using low surface energy chemicals	[88]
Coating with composites of nanoparticles	Nanoparticle-induced micro or nanostructure	Using low surface energy chemicals	[89]
Sol-gel process	Rough coating	Using low surface energy chemicals	[90-92]

However, the hydrophilization step is not always mandatory if the proper material, having low surface energy or slippery behaviour, is chosen. Some of the materials widely used for superhydrophobic applications are summarized below.

2.3.1.1 Fluoropolymers

Since fluoropolymers have extremely low surface energies, they are promising candidates to prepare superhydrophobic surfaces in the literature. It is possible to prepare superhydrophobic surfaces using this kind of polymers using surface roughening techniques.

Zhang *et al.* [93] used poly tetrafluoroethylene (PTFE) films to prepare superhydrophobic surfaces. PTFE has only fluor and carbon atoms on the polymer's backbone and around 20 mN/m surface tension, making it an excellent choice for superhydrophobic applications. They stretched this film to modify the surface. They reported that the extended film had some fibrous crystal structures that provide a rough surface, and this particular structure provided superhydrophobicity. Another work to produce superhydrophobic surfaces with PTFE has been carried out by Shiu *et al.* [94]. Differently, they used the oxygen plasma technique to obtain a rough surface of PTFE films, and with this method, they achieved higher than 165° of WCA.

Because of the low solubility of many fluorinated materials, it is also a standard method to use them as a mixture of other polymers, which are generally easy to roughen to achieve superhydrophobicity. Yabu *et al.* [95] prepared a porous membrane offering superhydrophobicity using a fluorinated block polymer solution with a casting method. It was also reported that the produced membrane was transparent because of the small pore sizes. Xu *et al.* [96] used the combination of chemical polymerization and electropolymerization techniques to fabricate roughened perfluorooctanesulfonate doped polypyrrole films. As an exciting feature, these films had reversible switching between super hydrophilicity and superhydrophobicity with the changing applied voltage.

2.3.1.2 Silicones

After fluoropolymers, silicones also have a very high potential to produce superhydrophobic surfaces thanks to their low surface energy and slippery surface properties [77, 97]. Polydimethylsiloxane (PDMS) is one of the most studied materials among silicones, and it is possible to impart superhydrophobicity by using several simple processes. The chemical structure of PDMS is given in Figure 2.17.

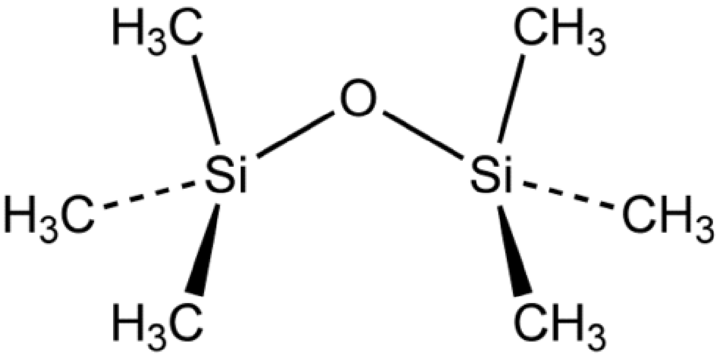

Figure 2. 17 Chemical structure of PDMS *[98]*.

Khorasani *et al.* [97] used an excitation source, a CO_2 pulsed laser, to modify the PDMS surface. After this treatment, the PDMS surface exhibited over 170° of WCA, and it is believed that this increase is mainly about the porosity and roughness of the treated surface (Figure 2.18a). In a similar study, Jin *et al.* [99] used laser-assisted etching technique to roughen the surface of PDMS. They reported that the etched surface had higher than 160° of WCA and lower than 5° of sliding angle.

Nanocasting is another method to roughen the surface of PDMS. Sun *et al.* [100] applied this method to achieve superhydrophobicity with PDMS. Firstly, they fabricate a negative template of rough PDMS using lotus leaf; then, they produce a positive PDMS surface using this template which mimics the original lotus leaf

(Figure 2.18b). They also claimed that the surface energies and chemical structures are quite different around the same surface hydrophobicity and sliding angle of lotus leaf obtained using this technique.

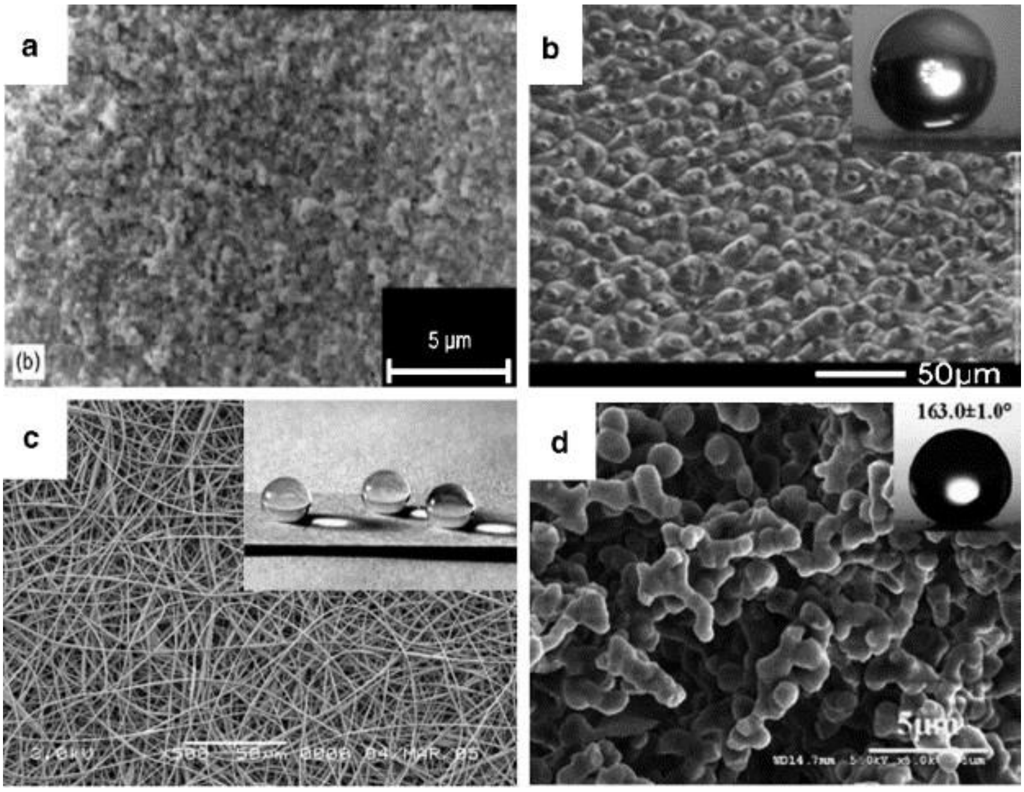

Figure 2. 18 *Surface appearances of laser modified PDMS surface (a), artificial lotus leaf (b), polystyrene-b-dimethylsiloxane and polystyrene blend non-woven textile, and polystyrene-b-dimethylsiloxane films prepared by vapour-induced phase separation [97, 100-102].*

Another way to produce superhydrophobic surfaces using PDMS is to use a block copolymer, such as polystyrene-b-dimethylsiloxane. Ma *et al.* [101] fabricated an electrospun membrane in a nonwoven textile form using polystyrene-b-dimethylsiloxane and polystyrene blend (Figure 2.18c). They achieved more than 155° of WCA, and it was reported that the superhydrophobic effect results from the thin fibre structure and low surface energy of the polymer blend. Superhydrophobic electrospun membranes are of particular interest because of their unique properties, such as breathability, flexibility, and light weightiness, especially for biomedical and textile applications. Zhao *et al.* [102] used vapour-induced phase separation techniques to prepare superhydrophobic surfaces using polystyrene-b-dimethylsiloxane, and they also carried out another step for the surface enrichment of PDMS (Figure 2.18d).

2.3.1.3 Organic and Inorganic Materials

Although lotus leaf exhibits high superhydrophobicity and sliding angle, it does not contain silicones or fluorocarbons on its chemical structure but paraffinic hydrocarbons. This is proof that it is possible to use organic or inorganic materials to fabricate superhydrophobic surfaces. For example, Lu *et al.* [103] used polyethylene, which has much higher surface energy than many fluoropolymers and silicones, to produce superhydrophobic films. They prefer to use a solvent/non-solvent system to achieve high porosity and control the crystallization behaviour of polyethylene. As a result, they obtained higher than 170° of WCA with the floral-like nanostructured crystal structures, as seen in Figure 2.19.

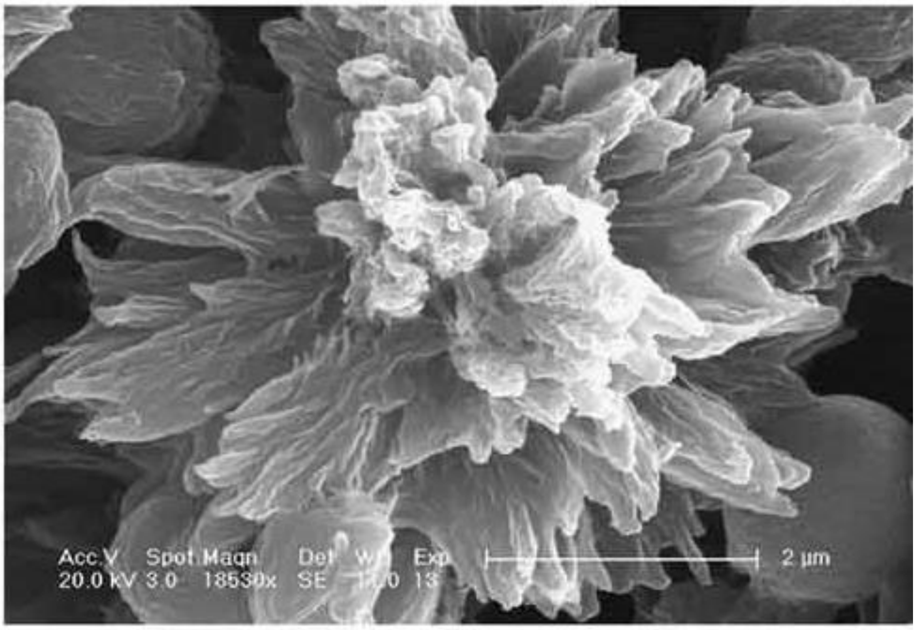

Figure 2. 19 *Floral-like nanostructured crystal structures [103].*

Other organic materials have been used to prepare superhydrophobic surfaces such as polystyrene, polycarbonate, and polyalkylpyrrol. In addition, some inorganic materials have been used, such as ZnO and TiO_2, to achieve superhydrophobicity. Feng *et al.* [104] synthesized ZnO nanorods using two-step solution methods, and they achieved superhydrophobicity with these ZnO nanorod films thanks to the high roughness and low surface energy offered. The SEM image of the prepared nanorod film is given in Figure 2.20. It is also noteworthy that under UV light, the superhydrophobicity of the ZnO nanorod films transformed to hydrophilicity, most probably due to the electron pairs generated by UV light.

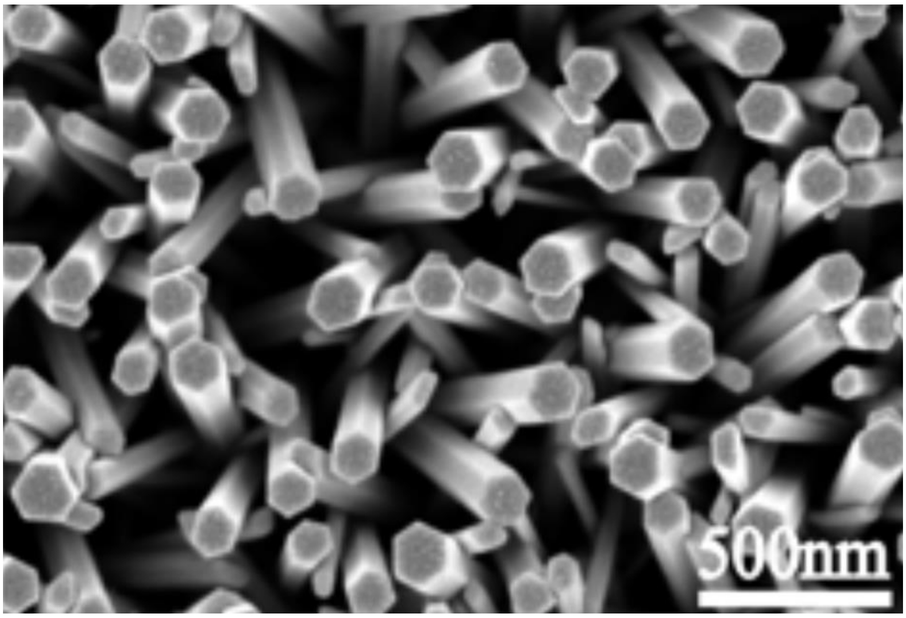

Figure 2. 20 *ZnO nanorod films fabricated by Feng et al. [104].*

2.3.2 Surface Roughening Methods

There are many methods to prepare rough surfaces, including mechanical stretching, lithography, solution casting, laser etching, chemical reaction, and deposition techniques, and more. Additionally, for the modification of the surface chemistry, for example, chemical bonding, physical binding, adsorption, etc. In this section, surface roughening methods, which are used to prepare superhydrophobic surfaces, will be explained, and subsequent modification of surface chemistry will be discussed.

2.3.2.1 Sol-Gel Processing

Sol-gel is a widely used method for preparing superhydrophobic surfaces from different materials. When the low surface energy materials are used for the surface production with the sol-gel method, no subsequent treatment is necessary to achieve superhydrophobicity which can be considered as an important advantage. Shirtcliffe *et al.* [105] produced superhydrophobic surfaces via the sol-gel method using organo-triethoxysilanes. It was reported that the produced material was a porous foam structure, and it was changing wettability properties when the temperature changed. Another study to produce superhydrophobic materials using the sol-gel method was carried out by Hikita *et al.* [106]. They used fluoroalkyl silane and colloidal silica particles to form a sol-gel film which offered high water contact angles (Figure 2.21). Shang *et al.* [107] prepared transparent silica particle-based sol-gel films, and after surface functionalization with a fluorinated silane coupling agent, they achieved superhydrophobicity.

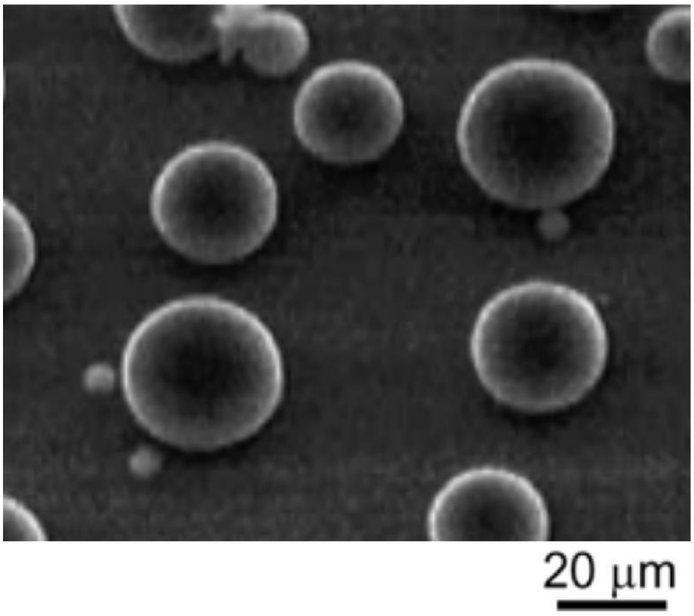

Figure 2.21 *AFM image of sol-gel film containing 30 wt.% colloidal silica [106].*

2.3.2.2 Lithography and Etching Techniques

Etching methods such as plasma etching, chemical etching, laser etching are used widely to produce rough surfaces to provide the superhydrophobic effect [108]. Teshima *et al.* [109] used the oxygen plasma etching method to prepare rough surfaces using polyethylene terephthalate. After that, they used the chemical vapour deposition method with a silane precursor to functionalize the surface and achieve superhydrophobicity. Shen *et al.* [110] described a simple chemical etching method to increase the roughness of polycrystal metals. After roughening the metals, they carried out a surface treatment with silanes to obtain superhydrophobic metal surfaces.

Micro-nanopatterned surfaces can be quickly produced using lithography techniques, such as electron beam lithography, photolithography, soft lithography, etc. As one of the main factors of surface wettability is the topography of the surface, this method is widely used to prepare the surface wettability of the materials. Martines *et al.* [111] used plasma etching and electron beam lithography techniques to obtain superhydrophobic surfaces. They produced nanopillars and nanopits on the surface and achieved superhydrophobicity with a water contact angle of 164° and contact angle hysteresis of less than 1°.

2.3.2.3 Colloidal Assembly and Layer-by-Layer Methods

The layer-by-layer method is a thin film fabrication method with oppositely charged materials. It is possible to control the thickness of the thin film at an even molecular level using this method. Many groups have used this method to fabricate rough surfaces for superhydrophobicity. Zhai *et al.* [112] used the LbL method with acid treatment techniques to obtain honeycomb structure from polyallylamine hydrochloride, polyacrylic acid multilayer structure. They carried out a crosslinking step, and then, using a dip-coating method, they deposited some silica nanoparticles on the surface to achieve superhydrophobicity. The advantage of this multi-step fabrication method was to provide a hierarchical structure, which is a critical property to increase the water contact angle of the surface. The SEM image of the designed surface is given in Figure 2.22.

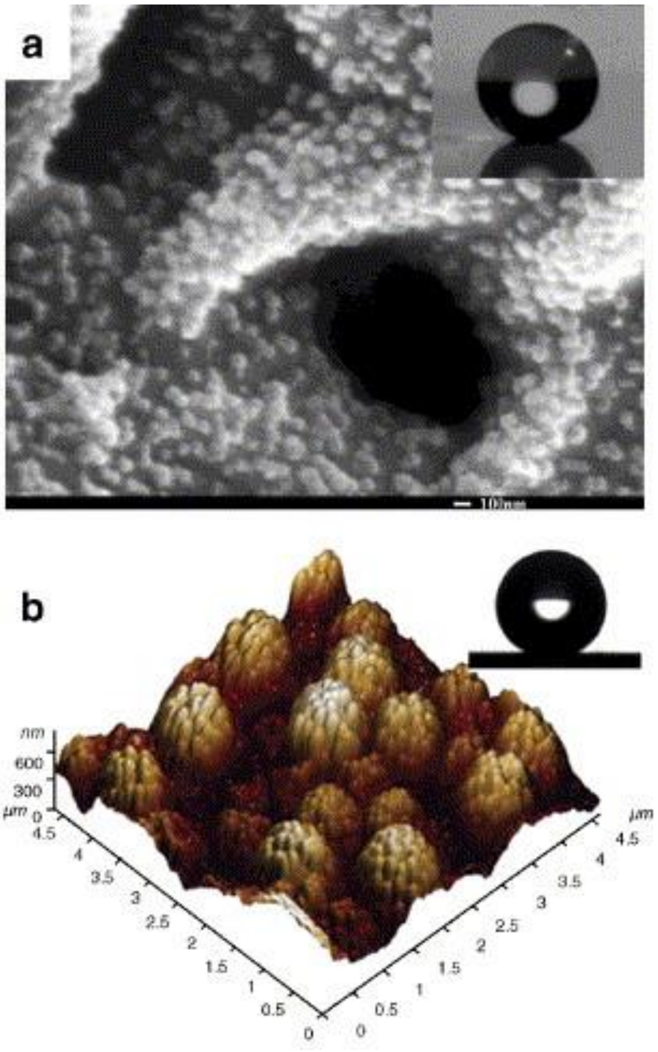

Figure 2. 22 *The hierarchical structure achieved by Zhai et al. and AFM result of Ming et al. [81, 112].*

The colloidal assembly method also is a promising technique to achieve high roughness values with superhydrophobic properties. Ming *et al.* [81] fabricate a roughened surface using this method which consisted of some silica particles. The surface had been modified with PDMS and achieved superhydrophobicity (Figure 2.22b)

2.3.2.4 Electrochemical Deposition

Electrochemical deposition methods have been used widely to achieve superhydrophobicity. This process involves depositing a thin metal film layer or a metal oxide tightly onto the electrically conductive substrate. The schematic representation of the electrochemical deposition method is given in Figure 2.23.

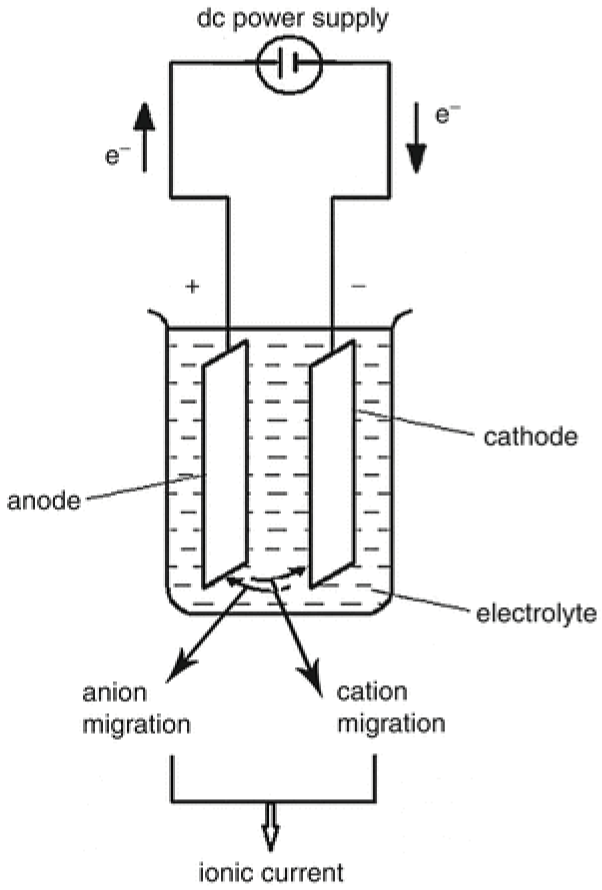

Figure 2. 23 *Schematic representation of electrochemical deposition method [113].*

Zhang *et al.* [114] published a study showing that it is possible to provide superhydrophobicity for indium thin oxide surfaces via gold nanoparticles' electrochemical deposition method. Another study has been carried out by

Shirtcliffe *et al.* [115]. They used patterning methods with electrochemical deposition techniques to obtain double roughened copper surfaces. They also carried out a hydrophilization step with fluorocarbons, and it was reported that the structure they produced showed superhydrophobicity with a water contact angle of 160°.

2.4 The Use of Electrospinning Process to Prepare Superhydrophobic and Multifunctional Surfaces

2.4.1 Surface-Modified Electrospun Membranes

Surface modification techniques are one of the most common ways to achieve superhydrophobicity using electrospun membranes. It is possible to modify the surface chemically to obtain lower surface energies, or physically to achieve high roughness values. In both scenarios, a significant increase in water contact angle may be achieved. For example, Yoon *et al*. [116] applied a two-step fabrication process to produce superhydrophobic surfaces. They firstly prepared an electrospun membrane using poly (3-hydroxybutyrate-co-3-hydroxy valerate), and then, subsequent treatment of the electrospun surface with plasma CF_4 was carried out. The electrospun poly (3-hydroxybutyrate-co-3-hydroxy valerate) nanofibre membrane with no plasma treatment exhibited a 142° of water contact angle. However, after the CF_4 plasma treatment of 150 seconds, 158° of contact angle was achieved thanks to the fluorine atoms introduced onto the fibre surface. They also found that after 300 seconds of plasma treatment, the water contact angle of the electrospun membranes decreased because of the surface etching, resulting in a decrease in the surface roughness and fluorine content.

Islam *et al*. [117] produced blend polymer nanofibres via electrospinning using poly vinylalcohol/pullulan (PULL/PVA) polymers. After that, they used perfluorooctyltriethoxysilane (PFOTES) to modify the electrospun nanofibre membrane to achieve superhydrophobicity. It was reported that, without PFOTES modification, when 9 wt.% and 12 wt.% of total polymer concentrations were used, membranes could not reach the superhydrophobic region, 150° and above. Superhydrophobic membranes with contact angles of 155° and 152° were obtained after PFOTES modification.

Wang *et al*. [118] produced thermoplastic polyurethane (TPU) nanofibre membranes using the electrospinning technique. Produced membranes were then functionalized by using hexadecyltrimethoxysilane-modified nano-silica via the solution-immersion method to achieve superhydrophobicity. It was also reported that the nano silica-treated TPU electrospun mat displayed both superhydrophobicity and superoleophilicity. Thus, it can be promising to continuously separating oil and water mixtures, as shown in Figure 2.24, which may find its applications in technological areas.

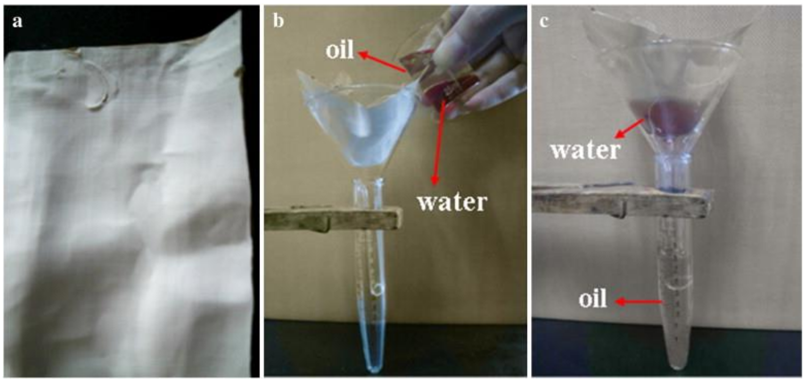

Figure 2.24 *(a) Electrospun mat after functionalization, (b and c) the process of the separation of water and oleic acid mixture [118].*

Yildiz *et al*. [119] used the electrospinning method to apply hybrid polyurethane/silica coating on the cotton fabric. A UV lamp was set up in the electrospinning cabin to stabilize the coating applied. The highest value of contact angle achieved was 154°. It was also reported that the amount of the inorganic part in the hybrid solution directly affected the contact angle.

Malarmohan *et al*. [120] used poly (caprolactone) with a small amount of 1H,1H,2H,2H-Perfluorodecyltriethoxysilane (0.05 vol.%) to produce superhydrophobic electrospun membranes. They reported that without PFDTES, PCL has only 80° of contact angle, but after surface modification with PFDTES, the contact angle achieved increased up to 154°.

Zhu *et al*. [121] fabricated superhydrophobic surfaces with a combination of electrospinning and hydrothermal coating (Figure 2.25). They collected PVDF nanofibres directly hydrothermally grown TiO_2 surface. The surface obtained was modified using the perfluorooctyltriethoxysilane for 15 seconds, and a 160° of water contact angle was achieved. They also investigated the durability of the superhydrophobic effect, and it was also reported that after ten cycles of water jet treatment, the contact angle decreased from 160 to 152°.

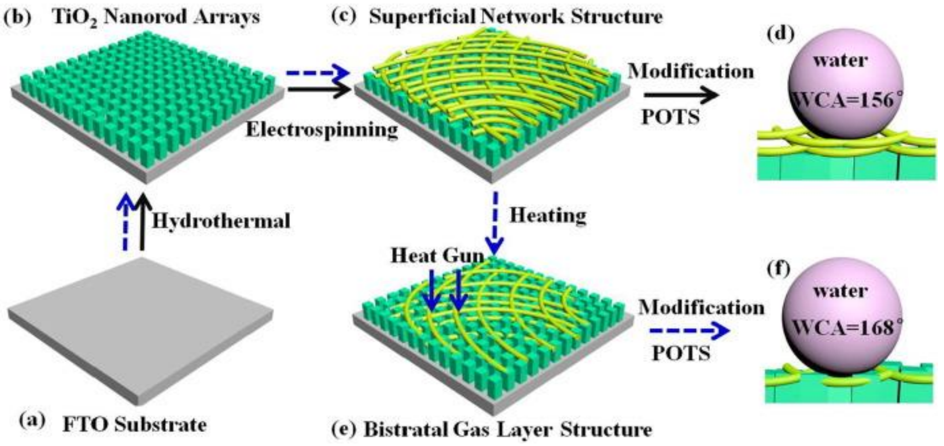

Figure 2.25 *Production steps used by Zhu et al. ((a)FTO substrate (b)* TiO_2 *nanoarrays (c) superficial network structure (d) bistrayal gas layer structure (d, e) modification of the substrate (f) final structure exhibiting superhydrophobicity) [121].*

Yang *et al*. [122] produced a multilayer structure using polyethersulfone (PES), polydopamine, and octadecyl trichlorosilane to obtain superhydrophobic membranes. Polyethersulfone nanofibre mat was produced with the electrospinning process followed by immersion into dopamine solution, and 24-hour polymerization under shaking was carried out at room temperature. The obtained structure was then modified using octadecyl trichlorosilane. It was reported that while PES itself had a 90° of contact angle, after DA polymerization on the surface, the contact angle was raised to the superhydrophobic region.

Li *et al*. [123] used PVDF with stearic acid (SA) to obtain superhydrophobic electrospun coatings on the Al surface. They found that while the PVDF nanofibre membrane had a 132° of water contact angle, with the addition of SA, it increased to 152°. They also reported that after 30 days in the NaCl solution, the contact angle of PVDF/SA coated Al did not significantly change.

2.4.2 The Use of Modified Electrospinning Set-Ups

Using different setups of electrospinning systems makes it possible to impart superhydrophobic properties to the electrospun membranes using less toxic chemicals, such as surface modification agents. Steckl *et al*. [124] reported the coaxial spinning method to produce superhydrophobic and superoleophobic surfaces. They used poly (ε-caprolactone) as the core and a commercial Teflon resin, Teflon^{TM} AF as the shell part of the fibre. They mentioned that coaxial electrospinning is a simple process requiring only relatively simple equipment, which can form superhydrophobic membranes with no permanent supporting substrate and use less hydrophobic material. They achieved 158° of water contact angle with this core-shell structure.

Zhan *et al*. [125] used the multi-nozzle technique for electrospinning to obtain superhydrophobic surfaces, as seen in Figure 2.26. Polystyrene was used with different concentrations (4-20 wt.%) to produce microscale and bead on string fibres hybrid structure. They changed the number of microscale fibres/beads on string fibres to understand their effect. It was reported that microfibres have a significant contribution to the membrane's mechanical properties. The simultaneous presence of bead-on-string fibres and microfibres generated a novel composite electrospun mat, which offered superhydrophobicity. 154° of water contact angle was obtained, and it was possible to control the value of CA and the mechanical properties of the electrospun composite film by altering the mass ratio of bead-on-string fibres/micro-sized fibres.

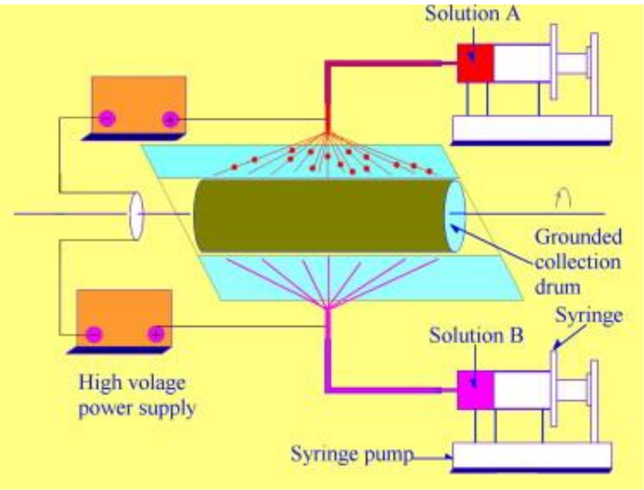

Figure 2. 26 *Production method used by Zhan et al. [125].*

Wang *et al*. [126] designed an electrospinning apparatus for unlimited production (Figure 2.27). They used three nozzles for the electrospinning system, and PVDF, polystyrene, and polyacrylonitrile were fed to the nozzles, respectively. They achieved up to 158.5° of contact angle with their design.

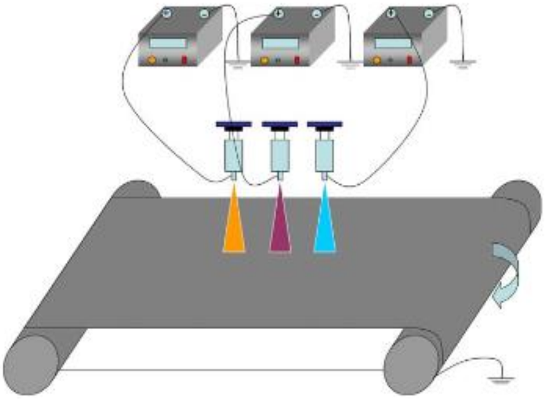

Figure 2. 27 *The schematic of the large-scale multi-nozzle electrospinning process [126].*

Su *et al*. [127] used the simultaneous electrospraying and electrospinning process for the membrane preparation. They used PVDF:DMAc (20 wt.%) solution for the electrospinning and Silica/DMAc (10 wt.%) colloids for the electrospraying (Figure 2.28). They found that the simultaneous electrospinning and electrospraying process provided the 3D structure of nanomembranes with much higher roughness values than the traditional electrospinning process. With the help of higher roughness values, the membrane they produced exhibited superhydrophobic properties with a water contact angle of 163°.

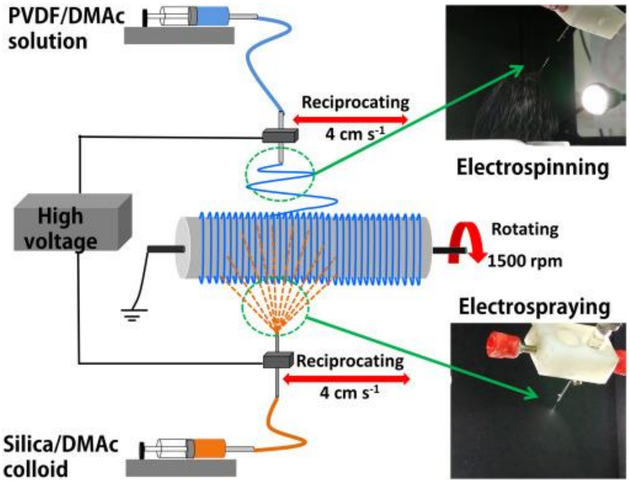

Figure 2. 28 *Schematic representation of simultaneous electrospinning-electrospraying process [127].*

Ding *et al*. [128] used a feedback system control to optimize all electrospinning parameters. This system was to control the surface roughness by changing input parameters. They found out that it was possible to produce superhydrophobic surfaces by using feedback system control.

Wang *et al*. [129] used Polystyrene-b-poly (ethylene-co-butylene)-b-polystyrene (SEBS) triblock copolymer to obtain electrospun membranes. After electrospinning, electrospraying was carried out onto the electrospun surface to spray nano-micro beads on it. After production of the membrane, thermal annealing at 170 °C and for 3 hours have been applied. It was reported that increasing the bead amount of the surface caused higher contact angles and provided superhydrophobicity. They also mentioned that thermal annealing provided physical crosslinking and made the superhydrophobicity of the product much more durable.

2.4.3 The Use of Nanofillers for Nanocomposite Electrospun Membranes

Hong *et al*. [130] obtained nanocomposite nanofibre membranes by using poly (vinylidene fluoride) (PVDF) with the epoxy–siloxane modified SiO_2 nanoparticles. The silica nanoparticles were synthesized firstly via the stöber method, and then they were modified by using a silane-epoxy coupling agent. It was also reported that epoxy–siloxane copolymer grafted on the surface of SiO_2 nanoparticles made the superhydrophobic surface more durable. The amount of the modified silica added had a significant role in the contact angle of PVDF (Figure 2.29).

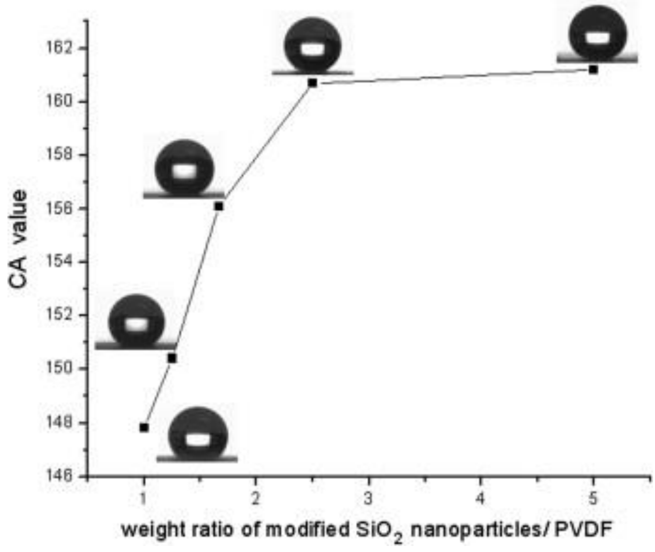

Figure 2.29 *Effect of SiO_2 amount on the contact angle of PVDF [130].*

Hutchings *et al*. [131] used polystyrene with a small amount of compatible polymer additives, end-functionalized with 1-3 fluoroalkyl groups. They reported that these kinds of additives could cause surface segregation, which results in lower surface energy. They also performed experiments using different amounts of additives and annealing time. They found that increasing amounts of additives caused increasing superhydrophobicity, and the annealing time had critical importance on the superhydrophobicity.

Xu *et al*. [132] prepared nanocomposite fibres using fluorinated polyhedral oligomeric silsesquioxanes (POSS) and PVDF-co-HFP. They have used two kinds of fluorinated POSS (i.e., FP8 and FPSi8). They collect electrospun nanofibres from the glass substrate to obtain transparent superhydrophobic surfaces. It was mentioned that with fluorinated POSS, 158° of contact angle could be obtained.

Song *et al*. [133] used PS with the ester modified silicone oil (EMSO) to obtain superhydrophobic electrospun membranes. For this purpose, 20 wt.% of Polystyrene solution was prepared using DMF, and after that, the EMSO was added to the solution prepared, with different molar mass ratios (from 0.05:1 to 0.60:1). It was reported that with the increasing mass ratios of EMSO/PS, the CA values also increased and reached a maximum of 152.60° of water contact angle

Liu *et al*. [134] used PVDF and ZnO nanoparticles together to produce tunable and controllable superhydrophobic membranes. They reported that pure PVDF itself has a maximum of 146° of contact angle. Post treatments with acid and ammonia were applied to the electrospun membranes to achieve higher contact angle values. The increasing amount of ZnO provides a higher contact angle up to 171° (8 wt.% ZnO), and modification of surfaces with POTS or ammonia provided anti-fouling property.

Dogan *et al*. [135] used ter polymer of tetrafluoroethylene, hexafluoropropylene, and vinylidene fluoride (THV) to prepare electrospun nanofibre membranes and characterise their properties. They also added clays to the electrospinning solution to see how surface properties changed. They used three concentrations of THV (8, 15, and 20 wt.%) and a 10:1 mass ratio of THV/Clay. It was found that both pure and clay reinforced electrospun polymer membranes have near superhydrophobic contact angle values. The lowest water contact angle was determined as 130° when the highest one was approximately 145°.

Tijing *et al*. [136] produced nanocomposite nanofibres using PVDF-co-HFP and carbon nanotubes (CNTs) to obtain superhydrophobic surfaces. They reported that the presence of CNTs in/on the nanofibres resulted in beads on the surface of the membrane, and some protruding CNTs were observed on the nanofibre surface. The maximum water contact angle reported was 156°.

Sun *et al*. [137] synthesized SiO_2 nanoparticles using the stöber method. Then, surface modification was carried out with three different silane coupling agents to obtain superhydrophobic nanofillers of three different sizes (90, 170, and 270 nm, respectively). The nanofillers obtained mixed with the PVDF using different ratios to prepare the final solution of electrospinning. The results showed that the type of silane coupling agent and the mass ratio of modified silica particles had an important role in the surface wettability of the composite nanofibre membrane. The water contact angle value increased from 149 to 160° as the mass ratio of modified SiO_2, and PVDF matrix increased from 0.5:1 to 5:1. The SEM result of one of the obtained surfaces is shown in Figure 2.30.

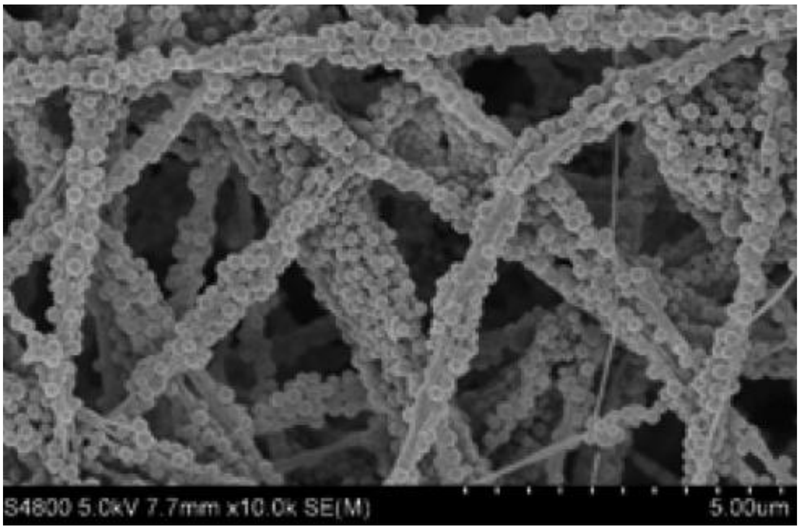

Figure 2.30 *SEM image of modified* SiO_2*/PVDF nanocomposite fibres [137].*

According to the literature review, it can be seen that the production of nanofibre membranes with superhydrophobic properties requires using nanofillers, subsequent treatment techniques, and/or surface modification methods. Producing superhydrophobic electrospun membranes with a shortened, easy, and scalable method is still a challenge. The first part of the study presented the one-step production method of superhydrophobic nanofibre membranes with no filler, modification, and/or subsequent treatment. The main parameters that affect the surface morphology of the membrane were optimized to reach the highest level of contact angle.

2.5 Icephobicity

2.5.1 Brief Information About Icephobic Surfaces

Ice formation can cause severe problems in many applications such as decreased efficiency of energy systems (i.e., wind turbines and solar panels,) delays for air transportation or, what is worse, aircraft accidents, personal injuries from falling ice masses, and structural damage of buildings because of the excessive weight of the ice [138-141]. There are many approaches to prevent surfaces from ice-caused problems, such as active heating systems [142], chemical de-icing fluids [143] (typically composed of ethylene glycol or propylene glycol), and mechanical removal [144]. These approaches have either energy-consuming working systems or environmental impacts. Producing anti-icing or icephobic surfaces seems the best option to reduce the effect of the ice formation in mentioned application areas.

2.5.2 Ice Nucleation

2.3.2.1 Homogenous Nucleation

When the water droplet gets cold (typically <0 °C), the phase transformation from water to ice can occur in two steps: ice nucleation and growth. Nucleation is when a few hundreds of water molecules come together and form tiny particles, and the growth is the expansion of this nucleus to get bigger sizes [145]. Figure 2.31 shows the molecular simulation of water quenching from high temperatures. After quenching, water molecules spontaneously attach into small groups. Then small groups are destroyed and reshaped, but all the systems still show a disordered structure with some randomly distributed long-lived hydrogen bonds. After that, a polyhedral structure with long-living hydrogen bonds appeared, which can be seen in the yellow circle. This polyhedral structure is named an embryo and slowly changes its shape by adding surrounding molecules with hydrogen bonds. Once this embryo becomes a nucleus, the water molecules in the polyhedral structure transform from a disordered arrangement to the stable phase, which means `ice formation`. Most of the time is consumed by the first icing step, which involves quenching to nucleus forming. Ice forming occurs immediately after the nucleus is formed because of the reduction of total energy, as shown in Figure 2.31 (f).

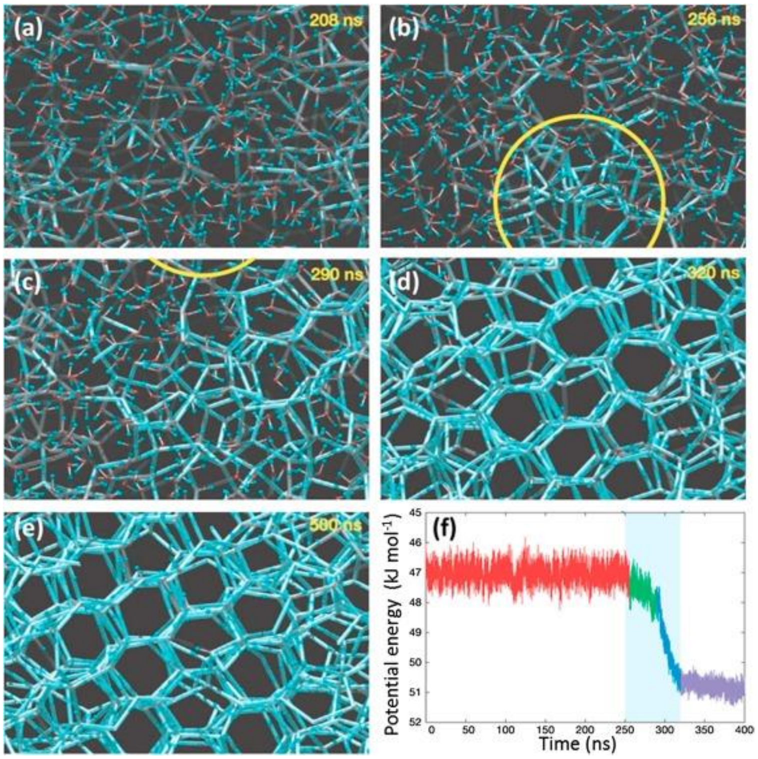

Figure 2. 31 *Molecularly-simulated hydrogen bond network structure of water at (a) 208 ns, (b) 256 ns, (c) 290 ns, (d) 320 ns, and (e) 500 ns and (f) the effect of the freezing process on total potential energy [145].*

As seen from the molecular simulation, there are three essential conditions of the nucleation process: supercooling, structure fluctuation, and energy fluctuation. By regulating these conditions, it is possible to produce anti-icing surfaces. If the embryo cannot reach the minimum size for the expansion process, the ice can not be formed, and the embryo will dissolve into water molecules again [145].

The nucleation process requires a critical size of ice nucleus, which is governed as:

$$r_c = \frac{2\gamma_{\mathrm{IW}}}{\Delta G} \qquad \textit{(Eq. 2.8)}$$

Where γ_{IW} is the liquid/solid interface energy, and ΔG is the energy of the new boundary (ice/liquid interface). This equation also conforms to the equation of Gibbs-Helmholtz:

$$\Delta G = \frac{\Delta H(T_{\mathrm{m}}\text{-}T)}{T_{\mathrm{m}}} \qquad \textit{(Eq. 2.9)}$$

From these two equations, the minimum nucleus size can be calculated as 2.2 nm for water at -20 °C. This minimum size varies depending on the temperature, and lower temperatures may require smaller nucleus sizes.

2.5.2.2 Heterogeneous Nucleation

Homogenous nucleation does not happen in most practical cases. The heterogeneous nucleation, which requires an existing solid surface, could occur mostly. The geometric factor f (θ) has an important impact on the free energy barrier $\Delta Gc'$ of the solid/liquid interface and the classical nucleation theory explain this phenomenon with the following equation:

$$\frac{\Delta Gc^{\prime}}{\Delta Gc} = f(\theta) = \frac{2-3cos\theta+cos^3\theta}{4} \leqslant 1 \qquad \textit{(Eq. 2.10)}$$

If the heterogeneous nucleation occurs on a perfectly smooth, flat surface, it is only related to the contact angle of the system. Variation of the contact angle and geometric factor is given in Figure 2.32.

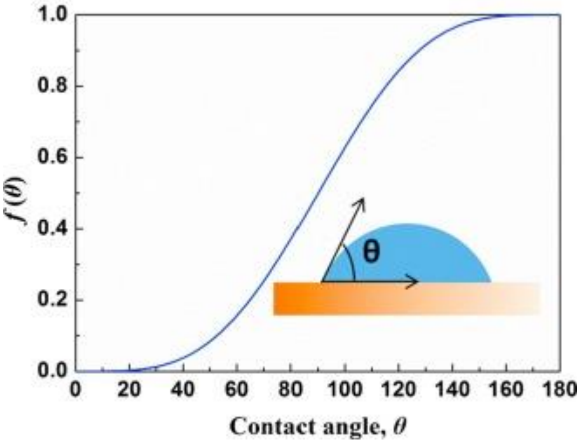

Figure 2.32 *Variation of the contact angle and geometric factor [145].*

However, because most surfaces are not perfectly flat, this relationship is not meant for practical applications. The effect of the surface topography on the $\Delta Gc'$ can be studied with convex and concave surfaces. In this case, the minimum size of the nucleus confirmed as the same as homogenous nucleation and $\Delta Gc'$ can be calculated from the following equations:

$$\Delta Gc' = \Delta Gc \cdot \frac{1}{2}\left[1 - cos^3(\phi + \theta) - \frac{3cos\theta sin^2(\phi+\theta)}{1+cos\phi} + \frac{(2-3cos\phi+cos^3\phi)sin^3(\phi+\theta)}{sin^3\phi}\right]$$

(Eq. 2.11)

and

$$\phi = \text{arccot}\left(\frac{R/r_c - cos\theta}{sin\theta}\right)$$ *(Eq. 2.12)*

Where θ is the contact angle of the nucleus on the spherical surface and ϕ is the angle between spherical surfaces with the planar substrate. These two equations are suitable for both convex and concave substrates.

To sum up, lower roughnesses and higher contact angle values can provide a higher free energy barrier which causes longer icing times or lower freezing temperatures. Cooper *et al*. [146] improved these equations by adopting an angle of ice nucleus on the planar substrate. In this case, the free energy barrier of ice nucleation can be given as follows;

$$\Delta G_c' = \Delta G_c \cdot f(\theta_p) \qquad \textit{(Eq. 2.13)}$$

where $f(\theta_p)$ is the factor of heterogeneous ice nucleation.

2.5.3 Ice Adhesion

Adhesion is defined as a physicochemical process in which chemical, thermodynamic and mechanical forces bind two surfaces. There are four different parameters, which can affect the total adhesion between ice and solid surfaces: hydrogen bonds, Van Der Waals forces, mechanical adhesion (from the roughness of the surface), and electrostatic interactions.

Electrostatic interactions can occur between two substrates that can transfer electrons between their atoms or molecules based on Coulomb`s law and acceptor-donor interactions. According to Petrenko *et al*. [147], this type of interaction always occurs between ice and dielectric substrates, or ice and metal substrates. It has an essential contribution to ice adhesion strength.

Van Der Waals forces are joint interfacial forces and resulting from the dipole-dipole interactions. Although Van Der Waals forces are always present between two substrates, they have no significant contribution to ice adhesion strength and electrostatic interactions.

Hydrogen bonding results from the distribution of a proton between two electronegative atoms, such as fluorine, nitrogen, and oxygen. It is believed that hydrogen bonds are responsible for the cohesion of solid ice. However, only a limited number of studies show the effect of hydrogen bonds on the ice adhesion strength.

In practice, commercial surfaces are never perfectly smooth and always have a certain roughness and even porosity. This structure always affects the ice adhesion strength due to the liquid penetration of these 3D layers that provide mechanical anchoring after solidification. Mechanical forces usually occur at the micrometre scale and can be observed by optical microscopes. It is also crucial that when the surface roughness of porosity increases, the contact area between liquid and solid surface also increases, leading to more hydrogen bonds and electrostatic interactions.

2.5.4 Slippery Liquid-Infused Porous Surfaces (SLIPS)

After the work published by Aizenberg *et al*. in 2011 [10], slippery liquid-infused porous surfaces became a significant research topic. In their study, they produced a porous structure, and then this structure was infused with a lubricant (perfluorinated liquid such as Krytox-100). The obtained structure has significant advantages, such as low sliding angle, extremely low ice adhesion, and good bio-fouling properties. They also reported that SLIPS has self-healing properties with durability under high pressure.

There are three key criteria to produce SLIPS [10];

- The lubricant must wick into the pores and stay stable
- The porous solid surface must be wettable by lubricant
- The lubricant and test liquid (for icephobic applications `water`) must be immiscible.

The schematic representation of SLIPS is given in Figure 2.33.

Some of the unique properties of SLIPS can be summarised as follows:

- Repellency against ice and frost

- Stainproof
- Repellency against insects
- Repellency against biofilm growth
- Self-healing against mechanical effects.

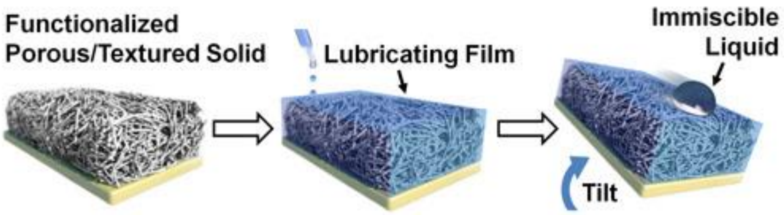

Figure 2.33 *Schematic representation of SLIPS [10].*

There are mainly three categories of techniques to fabricate the porous part of SLIPS. The most common one is the structuring of a flat surface. Some of the important approaches used for surface structuring are surface etching, laser writing, lithography techniques. The schematic representation of surface structuring methods is shown in Figure 2.34. Subramanyam *et al.* [148] used the gas etching method to prepare nano-structured silicon substrates, which perform 10 times better than non-etched flat surfaces, for SLIPS applications. For metal surfaces, chemical etching [149], sand blasting and electrolysis [150] methods are also widely used.

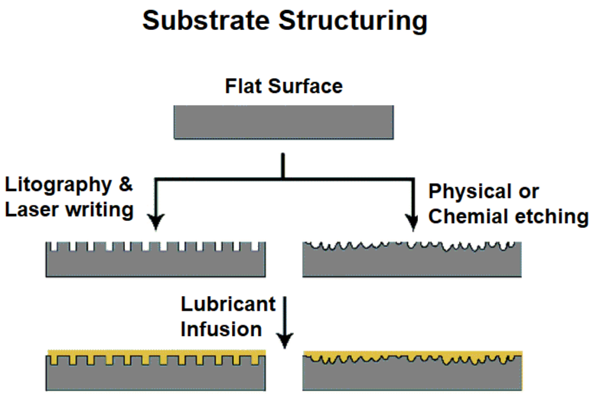

Figure 2. 34 *Surface structuring methods used for SLIPS preparation [151].*

The second category to prepare porous surfaces is the in-situ growth of porous surfaces on a flat surface. However, the maximum surface which can be prepared using this method depends on the container size of the reaction. However, it is possible to prepare both nano and microscale textured organic and inorganic structures using these techniques. As an example, a mussel-inspired polydopamine coating for immobilizing TiO_2 nanostructures through a sol-gel process was proposed by Lee et al. [152].

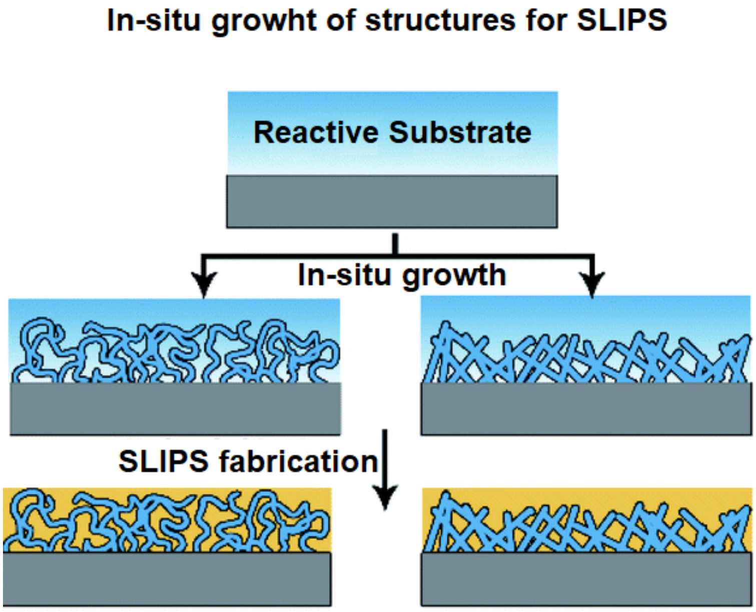

Figure 2. 35 *In-situ growth fabrication techniques used for SLIPS [151].*

Moreover, Seeger *et al.* [153] proposed a facile method to fabricate a superhydrophobic substrate by *in situ* growth of silicon nanofilaments which offered a good textured structure. Figure 2.35 explains the fabrication techniques of the porous part of SLIPS using in-situ growth techniques.

The last main approach to fabricate textured or porous substrates as the porous part of SLIPS is surface coating and compositing. The main problem of the directly composited structured layer is the possibility of poor interfacial adhesion between the substrate and coated/structured layer. Wang *et al.* [154] used the brush-coating technique with a mixture of polymer and silica particles to obtain textured surface morphology for SLIPS applications. Levkin *et al.* [83] used the in-situ polymerisation technique to fabricate proper surface morphology for the applications of SLIPS.

2.6 Research Motivation and Challenges

It is reported widely that electrospinning is a promising method to prepare polymer or polymer-based nanocomposite fibre membranes [15-17]. Various groups have already investigated superhydrophobic applications of the electrospun membranes. However, the proposed techniques either have complicated production steps or include expensive and hazardous chemicals. There is still no straightforward and cost-effective approach, requiring fewer chemicals to prepare superhydrophobic electrospun membranes. On the other hand, although the electrospinning method has been used before to obtain superhydrophobic surfaces, no study has been published concerning the icephobic application of electrospun membranes. As superhydrophobicity and icephobicity are naturally connected applications, we believe that electrospun membranes are a strong candidate for icephobic applications using the Cassie-Baxter ice mechanism or specific material design SLIPS.

Our motivation for the work described in Chapter 4 was to explore the potential of the electrospinning system to prepare superhydrophobic electrospun membranes using an improved method. We propose this approach is straightforward, cost-effective, and requires fewer chemicals. There is no additive or any additional step, with only the polymer itself being used. For this aim, the production and solution parameters of the electrospinning system, which have a significant contribution to surface properties and bead formation, have been altered to achieve optimum surface roughness.

In Chapter 5, the electrospun fibre membrane is used as the porous part of slippery liquid infused porous structures, which is considered an efficient design to obtain icephobicity. The mechanism of the icephobic behaviour, and the theory behind the transparency achieved using electrospun membrane-based SLIPS, were studied. Because the electrospun nanofibre membranes produced exhibited excellent porosity and outstanding lyophilic properties, they proved ideal candidates for these applications. Additionally, different lubricants were used to understand the effect of lubricant on the icephobic properties of SLIPS.

In Chapter 6, instead of a virgin polymer, we used waste PET bottles to explore their potential as the matrix phase of magnetite/polymer nanocomposite nanofibre membranes. After preparing a recycled PET/magnetite nanocomposite membrane, a surface modification step with fluorinated silane functionalized SiO_2 was added to achieve multi-functional properties. The benefits of the magnetite and the surface treatment step were studied, and the possible mechanisms behind the properties achieved were explained theoretically.

CHAPTER 3

Methodology

3.1 Raw Materials and Chemicals

3.1.1 Polymers

P(VDF-co-HFP) (average M_n 130,000 and average M_W 400,000 g/mol) was purchased from Sigma Aldrich (UK) and used for the study of one-step production of superhydrophobic membranes (Chapter 4) and the study electrospun nanofibre based SLIPS (Chapter 5). The two main reasons for choosing P(VDF-co-HFP) are its fluorinated structure, which is essential to achieve superhydrophobicity by producing only rough surfaces, and its oleophilic nature, making it a promising material for SLIPS. Additionally, PVDF-co-HFP has good mechanical properties, high dielectric strength, low flammability, and low moisture absorption properties. Some critical properties of P(VDF-co-HFP) used in this work is given in Table 3.1.

***Table 3. 1** Properties of PVDF-co-HFP used.*

Surface Tension	24 mN/m at 20 °C
Density	1.78 g/ cm^3
Average Molecular Weight	400.000 g/mol
Viscosity	23000-27000 poise at 230 °C
Melting Temperature	135-145 °C
Decomposition Temperature	350 °C

The second polymer used was the recycled PET, which was obtained from a coke bottle. The reason for choosing this polymer was to demonstrate an alternate use area for recycled PET, which could help to boost recycling incentives for PET, working towards circular economy approaches. Some of the properties of the recycled PET used are given in Table 3.2.

Table 3. 2 *Properties of PET obtained from waste bottles [155, 156].*

Density	1.22-1.30 g/ cm^3
Average Molecular Weight	14000-15000 g/mol
Melting Temperature	240-245 °C
Decomposition Temperature	418-425 °C
Surface Tension	44-48 mN/m at 20 °C

3.1.2 Solvents

Dimethylformamide (DMF) (>99 wt.%), acetone (>99.9 wt.%), and dimethylacetamide (DMAc) (99.8 wt.%), which are known as the three primary solvents to dissolve PVDF-co-HFP, were purchased from Sigma Aldrich to prepare a clear solution of PVDF-co-HFP. As acetone is a volatile solvent having a very low boiling temperature (56 °C), it is not a proper solvent for the electrospinning process. Because of this reason, DMF:Acetone mixture has been used instead of acetone itself. It also balanced the high boiling point and very low volatility of the DMF. Trifluoroacetic acid (TFA) (>99 wt.%) and dichloromethane (DCM) (>99.8 wt.%) were used to prepare the r-PET solutions (both purchased from the Sigma Aldrich (UK)). Some of the key properties of the solvents used are given in Table 3.3.

Table 3. 3 *Some key properties of the solvents used [157-159].*

Solvents	**Surface Tension (mN/m)**	**Dielectric Constant**	**Boiling Point (°C)**	**Density (g/cm^3)**	**Vapor Pressure (kPa, at 20 °C)**
DCM	34.2	37.8	165.1	0.937	0.17
DMF	37.1	38.3	153.0	0.994	0.35
Acetone	21.0	27.0	56.0	0.791	24.53
TFA	72.0	8.5	72.4	1.490	1.17

3.1.3 Lubricants

Three types of lubricants having slippery nature and immiscibility with water were used to fabricate electrospun nanofibre-based SLIPS. A fluorinated lubricant, Polychlorotrifluoroethylene (PcTFE), was supplied by Halocarbon (USA). The silicon oil and paraffin wax oil were purchased from Sigma Aldrich (Germany). Viscosity, vapour pressure, thermal conductivity, and boiling point values of the lubricants used are given in Table 3.4.

Table 3. 4 *Some of the key properties of the lubricants used.*

	Vapour Pressure (mmHg)	**Viscosity (mPa.s)**	**Thermal Conductivity (W/(mK))**	**Boiling Point (°C)**
PcTFE	0.0017	870	0.065	290
Silicone Oil	0.6	1000	0.157	315
Paraffin Wax	0.13	910	0.12	370

3.1.4 Other Materials and Substrates

Acetone (>99.9 wt.%) and ethanol (>99.9 wt.%) were used to purify the PET bottle. Magnetite nanopowder (50-100 nm particle size) was purchased from Sigma Aldrich (UK) to produce magnetite-loaded r-PET electrospun membranes. Additionally, for the preparation of fluorinated silane functionalized SiO_2 (FSS), fluorinated silane coupling agent, 1h,1h,2h,2h-Perfluorooctyltriethoxysilane (PFOTES) (98 wt.%) was supplied from Sigma Aldrich (UK) and fumed SiO_2 (Aerosil R805, 5-20 nm particle sizes) purchased from Evonik Industries (Germany). Sodium hydroxide (Alfa Aesar) was used to activate the fibre surfaces before SiO_2 treatment. Lastly, as the Al substrate is one of the most studied materials for icephobic applications, we have used AL2024-T3 aluminium alloy as a reference for the ice adhesion strength comparison purpose.

3.2 Setup of Electrospinning Rig

A basic electrospinning set-up with a rotating drum collector was prepared to fabricate electrospun nanofibre membranes used in this work, as shown in Figure 3.1. A programmable syringe pump, *syringeONE,* was used to feed the polymer solution and control the flow rate. This device offers to control the flow rate as accurately as 0.01 ml/hour. Once the polymer solution was prepared, it was first poured into a syringe with having a 0.75 mm of inner diameter metal needle. After that, the polymer solution-loaded syringe was placed on the syringe pump to provide a controllable flow rate. This system was on a Single-axis automated scanning emitter motion, controlled using a computer and software. Thus, the fibres produced were deposited to all the surface of the collector, which provides a good homogeneity.

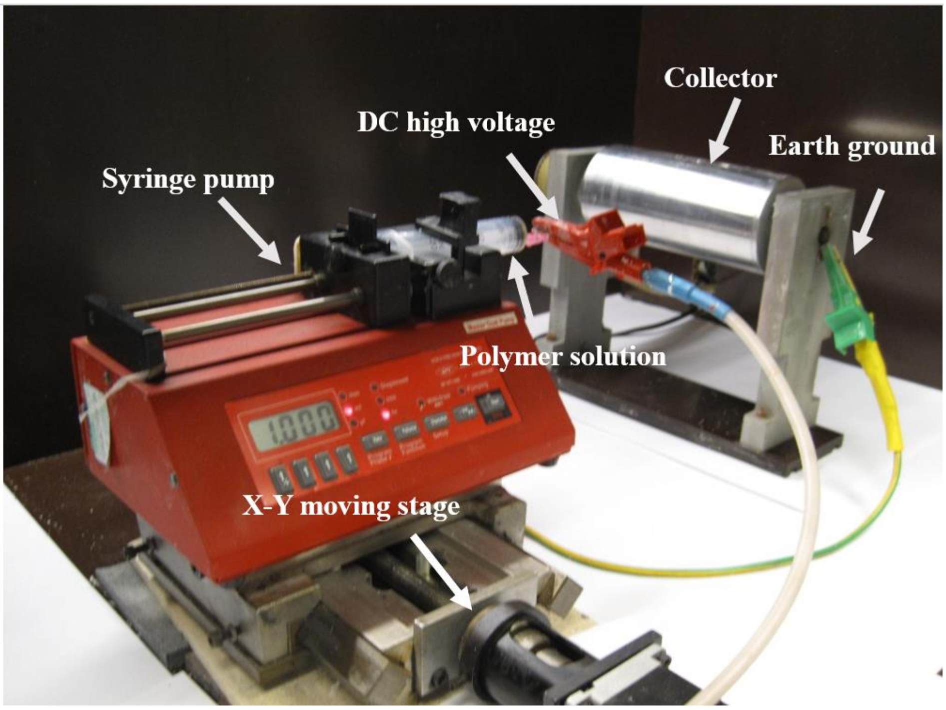

Figure 3. 1 *The image of the electrospinning rig used.*

A high voltage supplier (Glassman High Voltage Inc., EK40R15) with a maximum of 30 kV, was used to provide the required high voltage for the electrospinning process. A crocodile connector was used to apply the generated high voltage to the needle on the polymer solution-loaded syringe.

A rotating drum system with a speed-controlled engine was used to collect the nanofibres produced. Approximately 200 m/min of linear velocity was used to obtain randomly distributed nanofibre membranes. Nanofibre membranes of approximately 30x35 cm sizes were obtained using this collector. The image of the collector system is given in Figure 3.2.

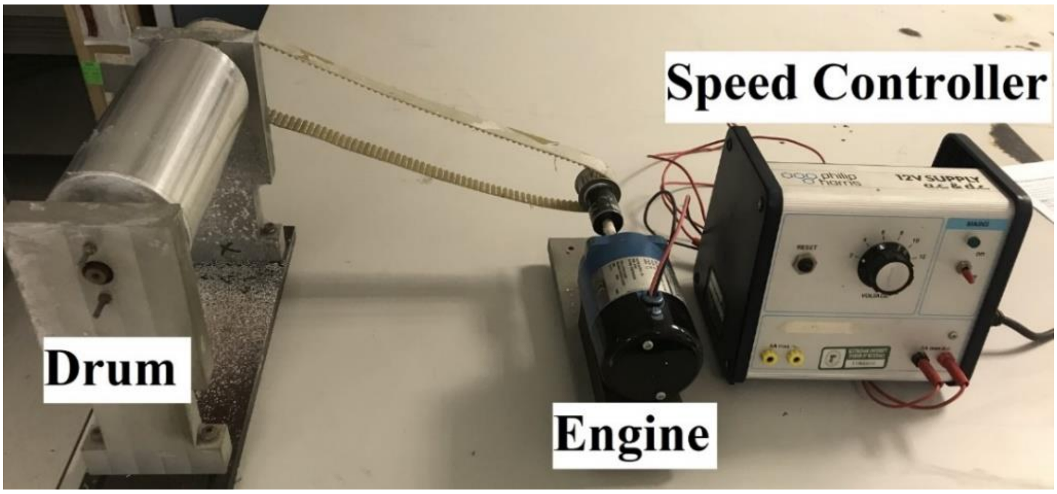

Figure 3. 2 *The rotating drum collector system prepared.*

3.3 Design of Experiments

Taguchi method, known as one of the most efficient in the consumption of energy, raw materials, and time, was applied for the experimental design. Full factorial L9 design, using the four main factors of electrospinning method: applied voltage, solution concentration, flow rate, and solvent used, was considered and three levels for each factor were determined. Electrospinning factors and the levels defined for the Taguchi experimental design used are shown in Table 3.5, and the Taguchi orthogonal array with nine trials explored is listed in Table 3.6.

Table 3. 5 *Factors and levels of Taguchi design.*

	Factors			
	Concentration (wt.%)	**Voltage (kV)**	**Solvent**	**Flow Rate (ml/hour)**
Levels	10.0	12.5	DMF	1.00
	12.5	17.5	DMAc	1.25
	15.0	22.5	Acetone/DMF	1.50

Table 3. 6 *Taguchi orthogonal array with nine trials.*

Code of Sample	**Solvent Used**	**Solution Conc. (wt.%)**	**Applied Voltage (kV)**	**Flow Rate (ml/hour)**
DMAc-15	DMAc	15.00	22.5	1.00
DMF-15	DMF	15.00	17.5	1.50
Ac/DMF-15	Acetone/DMF	15.00	12.5	1.25
DMF-12.5	DMF	12.50	22.5	1.25
Ac/DMF-12.5	Acetone/DMF	12.50	17.5	1.00
DMAc-12.5	DMAc	12.50	12.5	1.50
Ac/DMF-10	Acetone/DMF	10.00	22.5	1.50
DMAc-10	DMAc	10.00	17.5	1.25
DMF-10	DMF	10.00	12.5	1.00

Several calculations were carried out to understand the impact of selected factors and changes in levels on surface properties and fibre formation. Minitab 17 was used to calculate the signal-to-noise ratios according to the “larger is better” characteristic formula. The total variation of the nine trials was calculated according to the formula (Eq. 3.1):

$$S_T = \left[\sum_{i=1}^{N} \bar{Y}_i^2\right] - \left[\frac{\left(\sum_{i=1}^{N} \bar{Y}_i\right)^2}{N}\right] \qquad \textit{(Eq. 3.1)}$$

Where Y is the average contact angles of the samples and *N* is the trials number. The following formulas, Eq. 3.2-3.6, were also used to calculate the sum of squares of each factor:

$$S_A = \frac{A_{10}^2}{3} + \frac{A_{12.5}^2}{3} + \frac{A_{15}^2}{3} - C.F \quad \textit{(Eq. 3.2)}$$

$$S_B = \frac{B_{12.5}^2}{3} + \frac{B_{17.5}^2}{3} + \frac{B_{22.5}^2}{3} - C.F \quad \textit{(Eq. 3.3)}$$

$$S_C = \frac{C_{DMAc}^2}{3} + \frac{C_{DMF}^2}{3} + \frac{C_{DMF/Acetone}^2}{3} - C.F \quad \textit{(Eq. 3.4)}$$

$$S_D = \frac{D_1^2}{3} + \frac{D_{1.25}^2}{3} + \frac{D_{1.5}^2}{3} - C.F \quad \textit{(Eq. 3.5)}$$

where S is the sum of squares, and A, B, C, and D are solution concentration, applied voltage, the solvent used, and flow rate. Eq. 3.6 was used to investigate the percentage contribution (P_i) of each factor:

$$P_i = \frac{S_i}{S_T} \times 100 \quad \textit{(Eq. 3.6)}$$

3.4 Fabrication of Electrospun Nanofibre Membranes

The desired amount of electrospinning solution was loaded into a 20 ml syringe and then attached to a syringe pump for the process of electrospinning. The positive electrode of the power supply was connected to the metal needle of the syringe, which was holding the electrospinning solution, while the other was attached to the collector. After that, the distance between the collector and the needle was adjusted to the predetermined value, usually between 10 and 18 cm. Once the system was turned on, the rotating drum collector started turning at a speed of 200 rpm. The charged polymer droplet formed the Taylor's cone, followed by the jet's spinning after exceeding the critical voltage threshold. The electrospun polymer fibres were then collected to an aluminium foil, which was highly conductive. Once the solution was consumed, the system was turned off, and the electrospun membrane was obtained. The image of the electrospinning rig used for the productions is given in Figure 3.2.

For the productions in Chapter 4, nine different productions were carried out as shown in Table 3.6, which was designed according to Taguchi’s method. The polymer solutions with different solvent systems and concentrations were prepared at room temperature, using a magnetic stirrer for at least 4 hours, at 750 RPM. The deposition time was used to control the thickness of the electrospun membrane, and 3 hours of production provided about 40 μm.

For Chapter 5, fabrication of electrospun membrane as the porous part of SLIPS, 15 wt.% of electrospinning solution prepared using DMF/Acetone solvent system and production parameters were chosen as; 1.5 ml/h of flow rate, 17.5 kV of applied voltage, and 13 cm of collector-needle distance.

The waste bottle was first to cut into small pieces to fabricate r-PET and r-PET/magnetite nanocomposite membranes. Then, the PET bottle's trimmed pieces were entirely washed with acetone and ethanol, respectively. The r-PET pieces were dissolved in a solvent mixed by TFA and DCM (1:1 by volume) to form a 15 wt.% solution. The schematic representation of the r-PET solution preparation procedure is given in Figure 3.3.

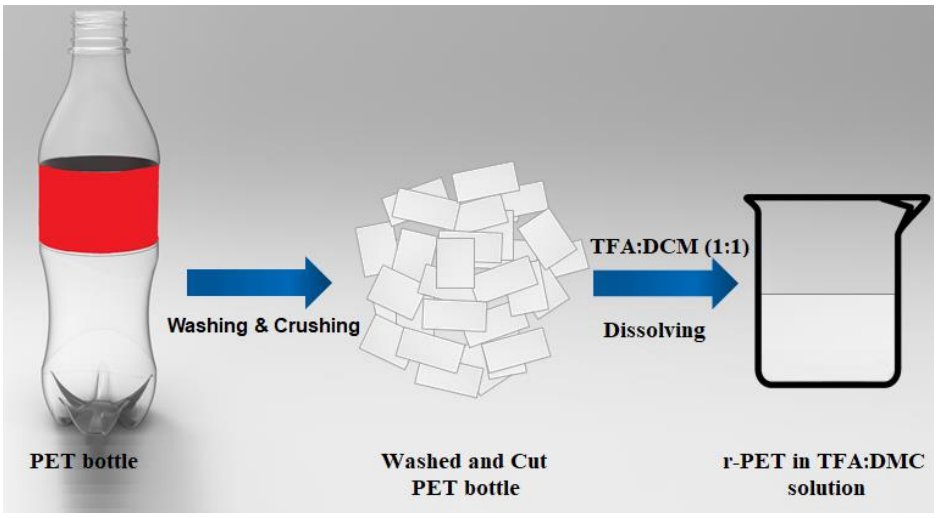

Figure 3. 3 *The schematic representation of r-PET solution preparation procedure.*

The blended solution was vigorously mixed with a magnetic stirrer for 4 hours at room temperature. To prepare the r-PET/magnetite dispersion, 20 wt.% of magnetite nanopowder was dispersed in TFA : DCM solution using a probe sonicator for 15 minutes.

15 wt.% of r-PET was eventually added to the magnetite dispersion prepared and stirred up for 4 hours. Besides, the r-PET/magnetite solution was subjected to ultrasonication for 30 minutes just before the electrospinning process. Owing to the high volatility of the solvents, all the procedures were carried out in a fume hood. The production parameters were applied as 22.5 kV of voltage, 2 ml/hour of flow rate, and 13 cm of collector-needle distance.

3.5 Fabrication of SLIPS

The schematic diagram of the fabrication process of nanofibre-based SLIPS is given in Figure 3.4. Three types of lubricants were used to fabricate SLIPS (). Approximately 20 mg/cm^2 of lubricant (silicone oil, paraffin wax, or PcTFE) was infused using a Pasteur pipette inside the pores of the electrospun nanofibre membrane upon a balance. It was important to get rid of the excess oil, and for this reason, all samples were kept in a 45° tilted plate overnight.

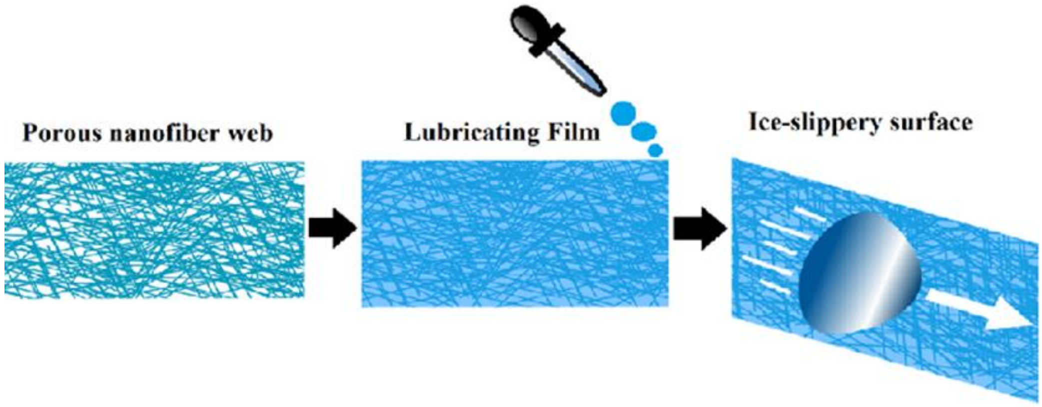

Figure 3. 4 *Fabrication of electrospun nanofibre-based SLIPS.*

3.6 Preparation of FSS and Surface Treatment of Electrospun Samples

For the functionalization of SiO_2, PFOTES was used as a silane coupling agent. Briefly, 0.1 ml ammonium hydroxide, 1 ml distilled water, and 1 ml PFOTES were added to 10 ml ethanol and stirred for 1 hour at 60 °C. Then, 0.1 g of SiO_2 with an average size of 5-20 nm was dispersed into the solution and mixed for another 3 hours at 60 °C. After that, the prepared FSS was purified using a centrifuge and dispersed in hexane. The schematic representation of the fluorination process is given in Figure 3.5.

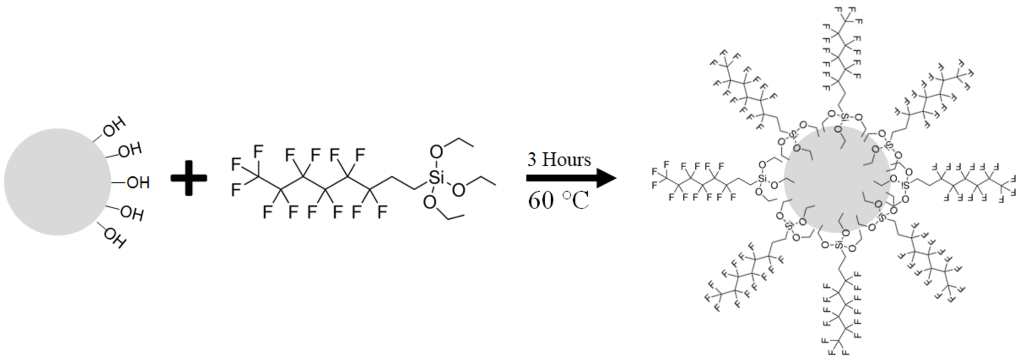

Figure 3. 5 *Surface modification of SiO_2 nanoparticles with PFTOES.*

For the surface treatment of electrospun membranes, it was essential to form chemical attractions between the surface and FSS particles. Thus, surface activation was conducted at room temperature using 0.1 M of aqueous NaOH solution to create functional groups on the surface of electrospun membranes. The samples were then washed with distilled water and dried in an oven at 50 °C. After that, the electrospun membranes were immersed in a hexane solution of 5mg/ml FSS particles for 5 seconds, followed by a heating process at 120 °C for 1 hour [160].

3.7 Characterisation Methods

3.7.1 Spectroscopic Analysis

3.7.1.1 X-Ray Photoelectron Spectroscopy

X-ray photoelectron spectroscopy (XPS) belongs to photoemission spectroscopies which is quantitative and based on the photoelectric effect (Figure 3.6). In the XPS technique, elements on the sample's surface can be identified, and elemental composition can be investigated. Additionally, XPS is a promising technique because, along with elements, it is possible to analyze other elements they are bonded to.

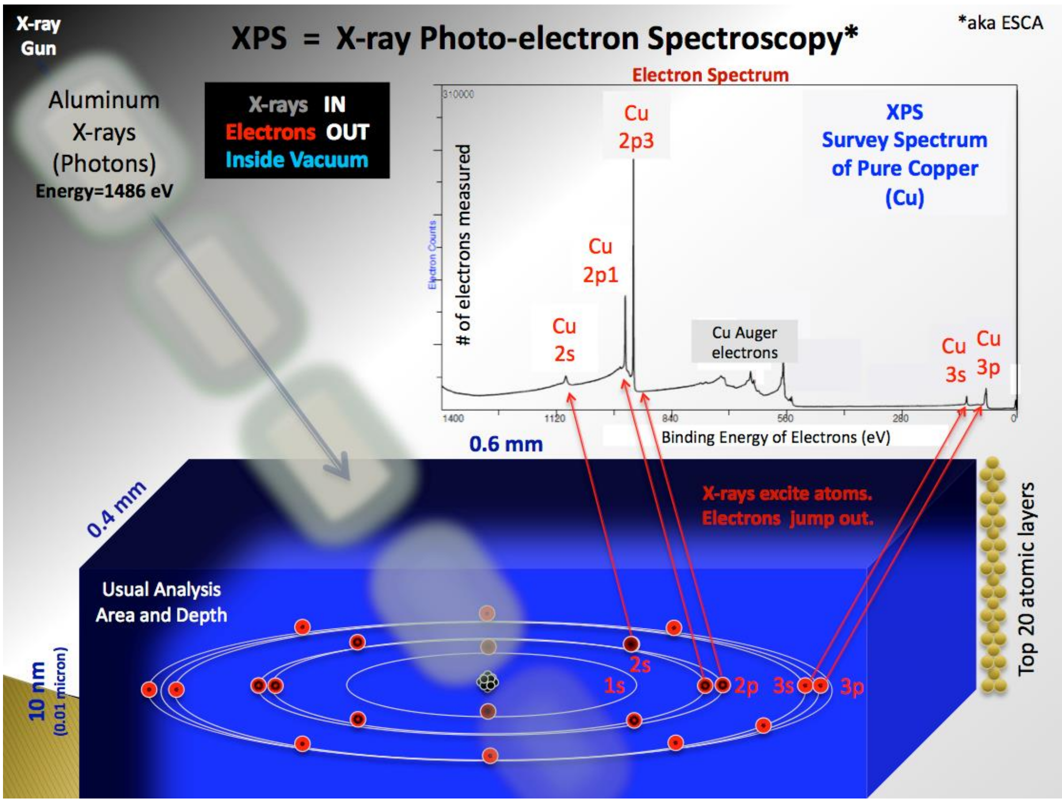

Figure 3. 6 *XPS and photoelectric field [161].*

In this work, VG ESCALab Mark II X-ray Photoelectron Spectrometer was used to investigate surface chemical compositions of the samples with Excitation source: twin Mg/Al anode: Mg K-alpha (hv = 1253.6 eV) or Al K-alpha (hv = 1486.6 eV). The spectra collected between 0-1200 eV and the adventitious carbon located at 284.8 eV was used to calibrate the XPS raw data.

3.7.1.2 Fourier-Transform Infrared Spectroscopy

Fourier-Transform Infrared Spectroscopy (FT-IR) is an easy, non-destructive and rapid technique used to detect the vibrational characteristics of chemical functional groups of solid, liquid, or gas samples by analysing an infrared spectrum of absorption and transmission and photoconductivity. An FTIR spectrometer can simultaneously collect spectral data in a wide spectral range (1-14,000 cm^{-1}), and this range can be divided into three categories: far-infrared (4-400 cm^{-1}), mid-infrared (400-4000 cm^{-1}), and near-infrared (4000-14000 cm^{-1}), respectively.

When the IR interacts with the sample, the functional groups start stretching and bending, making it possible to obtain a molecular fingerprint of the sample. An FTIR spectrometer has five main parts, an IR source, detectors, a beam splitter, mirrors, and attenuated total reflectance. The schematic diagram of an FTIR spectrometer is given in Figure 3.7.

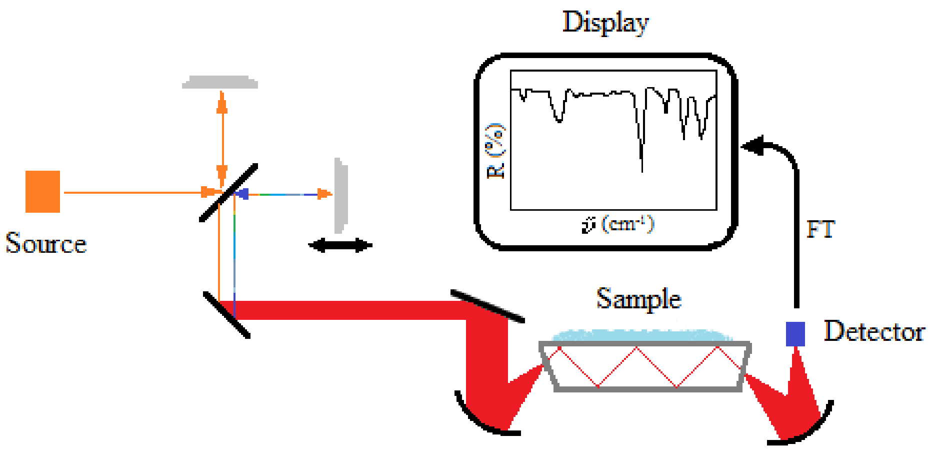

Figure 3. 7 *The schematic diagram of an FTIR spectrometer [162].*

In this work, a Perkin Elmer FT-IR with a single reflection horizontal attenuated total reflection accessory was used to investigate the chemical changes of the materials between 650-4000 cm^{-1} with no sample preparation steps. The average of four measurements was used as the sample spectrum.

3.7.1.3 UV-Vis Spectroscopy

UV-Vis is a fast, simple, and inexpensive method to investigate the optical properties of a material. The absorption, reflection, and transmission properties of the materials in liquid or solid form can be measured using this method. In UV-Vis, a beam with a wavelength varying between 180 and 1100 nm passes through the material. A UV-spectrometer consists of a light source (usually tungsten filament and Hydrogen-Deuterium lamps), a monochromator, reference and sample cells, a detector, and a computer to process and record the data produced.

A schematic illustration of a UV-vis spectrophotometer is given in Figure 3.8. In this work, a UV-Vis spectrometer (Biochrome, Libra S22) has been used to investigate some samples' transmittance properties between 300-950 nm, with the scanning rate of 0.5 nm. The following equation (Eq. 3.7) has been used to transform the data from absorption to transmittance.

$$T_{\%} = (10^{-Abs}) \times 100 \qquad \textit{Eq. (3.7)}$$

Where $T_{\%}$ is transmittance in percent and *Abs* is the absorbance value of the sample.

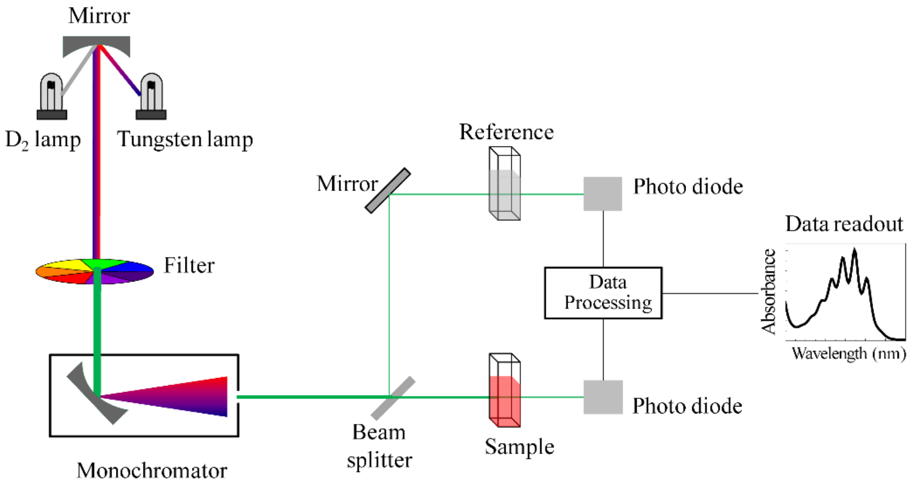

Figure 3. 8 *Schematic illustrations of a UV-vis spectrometer [163].*

3.7.2 Evaluation of Thermal Properties

3.7.2.1 Thermogravimetric Analysis

Thermogravimetric analysis (TGA) is a thermal analysis method used to investigate the changing weight of a sample as a function of increasing temperature. TGA has several applications such as determination of organic or inorganic additives, thermal characterization of materials, and degradation studies as it provides critical information about physical changes (absorption, desorption, phase changes, etc.), chemical changes (thermal decomposition, chemisorption, etc.) and Solid-gas interactions (reduction or oxidation).

A thermogravimetric analyzer usually consists of a thermocouple, high-precision balance, sample pan, reference pan, a system that purges inert gas or air, and a computer that processes the data. The pan holds the sample material and is located in a furnace. Depending on the analysis, the furnace is heated or cooled during the experiment, while a thermocouple is used to control and measure the temperature within the oven accurately. The change in weight of the sample is constantly monitored and saved during the experiment. It is also possible to control the environment by purging inert or reactive gases. A schematic illustration of a TGA is given in Figure 3.9.

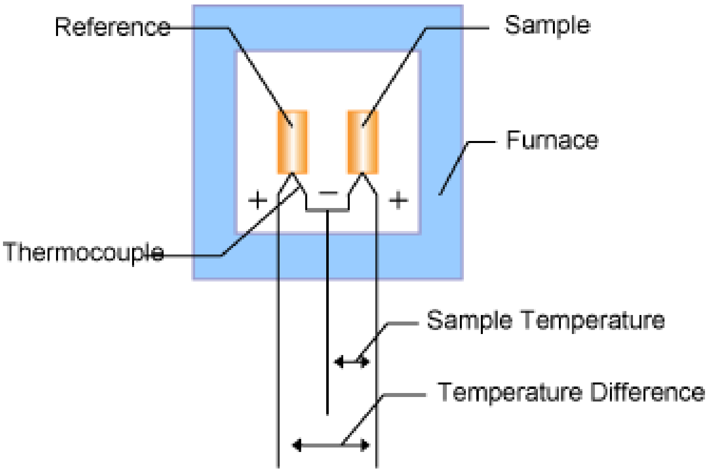

Figure 3. 9 *Schematic illustrations of TG analyser [164].*

In this work, some of the sample decomposition temperatures were investigated using TGA (TA instruments, SDT Q600) under an argon atmosphere with a purge rate of 20 mL/min. The analyses performed in the range of 50-600 °C and the constant heating rate of 20 °C/min was used.

3.7.2.2 Differential Scanning Calorimetry

Differential scanning calorimetry (DSC) is a thermo-analytical technique widely used to investigate the thermal properties of polymeric materials. The thermoanalytical DSC technique investigates some critical properties of polymer materials, such as the rate of crystallisation, glass transition temperature, melting temperature, decomposition temperature, and phase transition temperature.

There are two types of DSC: 1. Heat flux DSC and 2. Power compensation DSC. In the heat flux DSC, the temperature difference between the reference and the sample is calculated as the function of temperature, while the thermal energy applied to keep sample and reference equal is calculated in power compensation DSC. The schematic representation of a DSC is given in Figure 3.10.

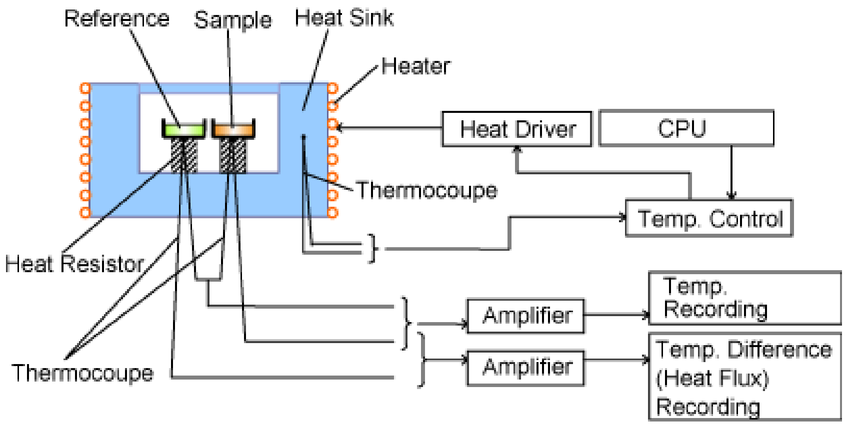

Figure 3. 10 *Basic working principles of DSC [165].*

DSC is used to investigate the degree of crystallization of electrospun membranes and melting temperatures in this work. The analyses were performed at 50-200 °C and 10 °C/min the heating rate. All analyses were performed under an inert atmosphere using Argon.

3.7.3 Surface Imaging and Topographical Characterisation

3.7.3.1 Scanning Electron Microscopy

A scanning electron microscope (SEM) is an electron microscope that produces images using a focused electron beam instead of light in optical microscopes. Compared to optical microscopes, SEM has several benefits, such as higher resolution, a large depth of field, and an accurate magnification degree. These advantages make it possible to use SEM in microstructure characterization, fracture analysis, thin-film evaluation, surface appearances examination, and failure analysis of different materials.

The main components of an SEM are an electron gun to produce electron beam, condenser, and objective lenses, scanning coils to scan electron beam across the surface of the sample, a sample chamber to mount the sample inside, and backscattered and secondary electron detectors. SEM has a complicated working mechanism, but basically, the electron gun produces a high-energy electron beam and is targeted to the sample's surface with the help of condenser and objective lenses. When the electrons hit the sample surface, they interact with the surface atoms and generate electronic signals (Secondary electrons, back-scattered electrons, characteristic X-rays). The secondary and backscattered electron detectors then collect these signals. A computer uses these signals to produce topographical and morphological images. Figure 3.11 represents a schematic diagram of SEM and sample-beam interactions.

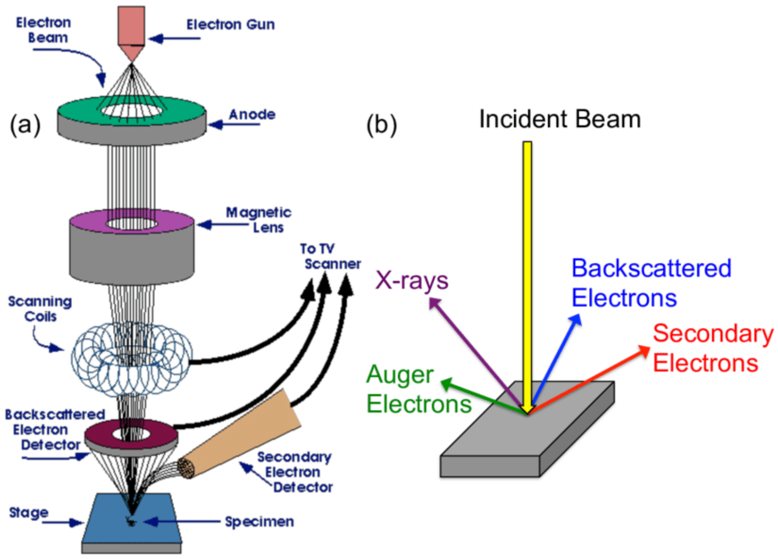

Figure 3. 11 *(a) Schematic representation of and working principle of SEM (b) the sample-beam interactions and electronic signals generated [166].*

In this work, a Joel 7000 scanning electron microscopy was used to carry out the surface imaging of the samples. SEM samples were prepared by adhering the electrospun membranes to an aluminium stub using carbon tape. The surface of the samples must be electrically conductive to generate sufficient electronic signals. Because the surface of the polymeric samples was not conductive, 8 nm of iridium coating was applied using a sputter coating system. After that, the samples were loaded inside the sample chamber of SEM. A voltage of 10 kV and 10 mm of working distance was used, and images were taken from different magnification levels.

3.7.3.2 3D Optical Profilometer

A profilometer is an instrument used to measure a sample`s surface profile to investigate its roughness values. Mainly, there are two types of profilometers: contact and non-contact. There are several techniques in non-contact profilometers, such as laser triangulation, confocal microscopy, digital holography, etc. Among these techniques, confocal microscopy is considered the most reliable and fast one. The schematic representation of the working principle of a 3D profilometer is given in Figure 3.12.

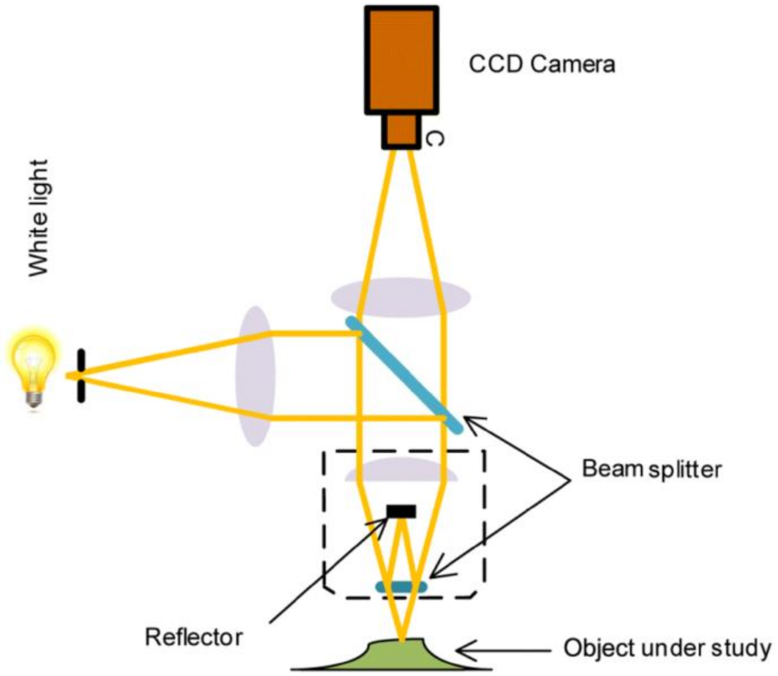

Figure 3. 12 *Working principle of a 3D profilometer [167].*

In this work, a Zeta-20 3D profilometer was used to investigate surface topography from 341 µm x 268 µm. Surface roughnesses, Ra, were also calculated with the same device from the 200 µm x 0.01 µm.

3.8 Performance Evaluations of Prepared Surfaces

3.8.1 Centrifugal Ice Adhesion Test

According to the centrifuge method, ice adhesion tests were performed to investigate the adhesion strength between ice and the substrate, using a homemade setup [168-170]. In this method, the sample is attached to one end of an aluminium beam (30cm x 32mm) and a balance weight should be located to the other end. Then this beam is started to rotate with a constant acceleration in a climate chamber. The speed of rotation at which ice detached from the aluminium beam needs to be noted to calculate ice adhesion strength. The centrifuge method consists of a three steps procedure:

1. The sample was put in one of the extremities of small beams, and 1.3 g of ice was grown on the sample in a cold room.
2. Prepared beams then were attached to the centrifuge system and started rotating with an acceleration of 30 RPM per second until the ice detached from the sample surface.
3. The ice adhesion is evaluated as a function of centrifugal force as the iced beam is rotated in a centrifuge at an accelerating rate until it detaches.

For this work, briefly, a glaze ice block with a 1.3 g mass was attached to the sample surface in a -10 °C chamber for the measurement. Figure 3.13 shows the schematic illustration of the ice-adhesion setup. Ice adhesion strengths were calculated using Eq. (3.8).

$$\tau = \frac{F}{A} = \frac{mr\omega^2}{A} \qquad \text{Eq. (3.8)}$$

Where ϖ is the rotation speed at ice detachment, F is the centrifugal force, m is the ice mass, and r is the length of the beam [171].

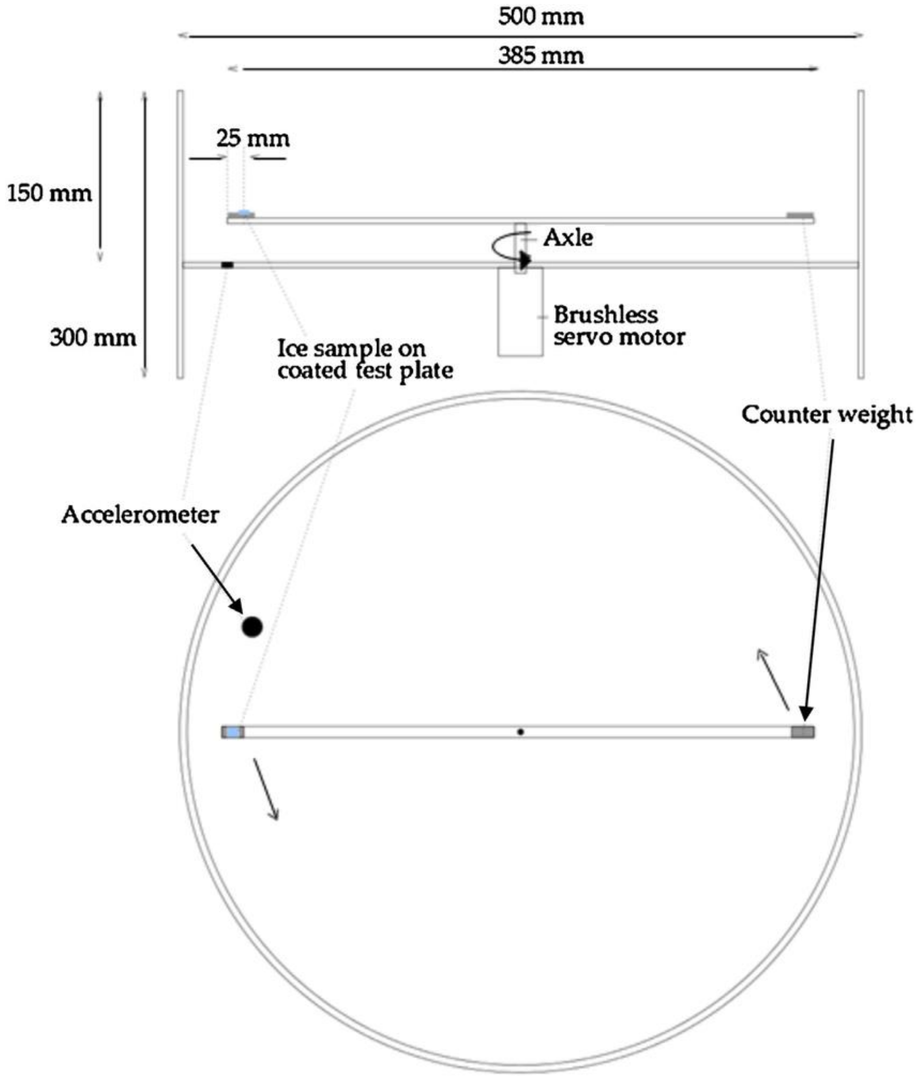

Figure 3. 13 *Schematic diagrams of the centrifuge ice adhesion test device [143] consist of a carbon fibre rotor driven by a brushless servo motor and housed in a stainless-steel casing.*

3.8.2 Droplet Icing Time

The droplet icing time tests were performed using a cold plate set at -10 °C. Five droplets with 4 µL of volume were located on the sample, and their icing times were calculated by observing the water droplets [171]. The cold plate used for the icing time measurements is given in Figure 3.14.

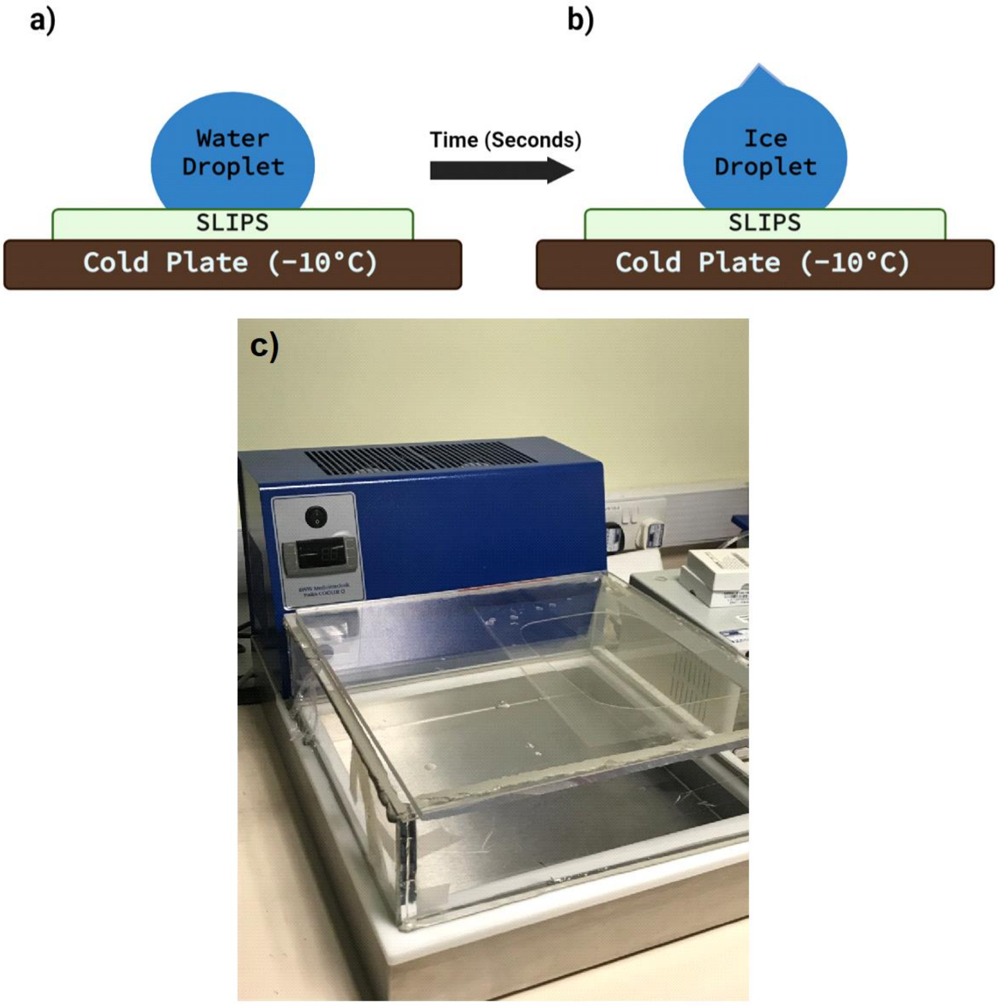

Figure 3. 14 *The test of droplet icing time, (a) water droplet on the sample located inside a cold plate, (b) ice droplet formation during the test, and (c) cold plate used for icing time measurements.*

The average icing duration was recorded to evaluate the delay of icing performance, and images every 10 seconds were taken until complete freezing of the droplet. Figure 3.14 shows the cold plate used during the icing time measurements.

3.8.3 Measurements of Static and Dynamic Contact Angle

The static contact angle of a solid surface is measured using a droplet of liquid where the liquid-vapour interface meets. It provides essential information about the mobility of the droplet on the surface. On the other hand, the dynamic contact angle is defined as the contact angle during the wetting (advancing contact angle) or de-wetting (receding contact angle) of the solid material. Contact angle hysteresis, an indicator of required activation energy for the mobility of the droplet, is calculated using advancing and receding contact angles.

In this work, the FTA200 dynamic contact angle system was used to measure the static and dynamic contact angles of the samples prepared. Static contact angles were measured at 4 μl of drop size, while the dynamic contact angles measured between 3 and 7 μl with a flow rate of 10 μl/min. The contact angle hysteresis of samples was calculated using Eq. (3.9).

$$\theta_{hyst} = \theta_{adv} - \theta_{rec} \qquad Eq.(3.9)$$

Where θ_{hyst} is contact angle hysteresis, θ_{adv} and θ_{rec} are the advancing and receding contact angles, respectively.

3.8.4 Electromagnetic Shielding Efficiency

Electromagnetic shielding efficiency measurement of the samples was carried out using a flanged coaxial EMI shielding effectiveness (SE) tester modified with a custom-built ASTM D4935-99 for a wide range of measurements smaller-sized samples. The manufacturing drawings and dimensions of the modified small-sample holder are given in Figure 3.15.

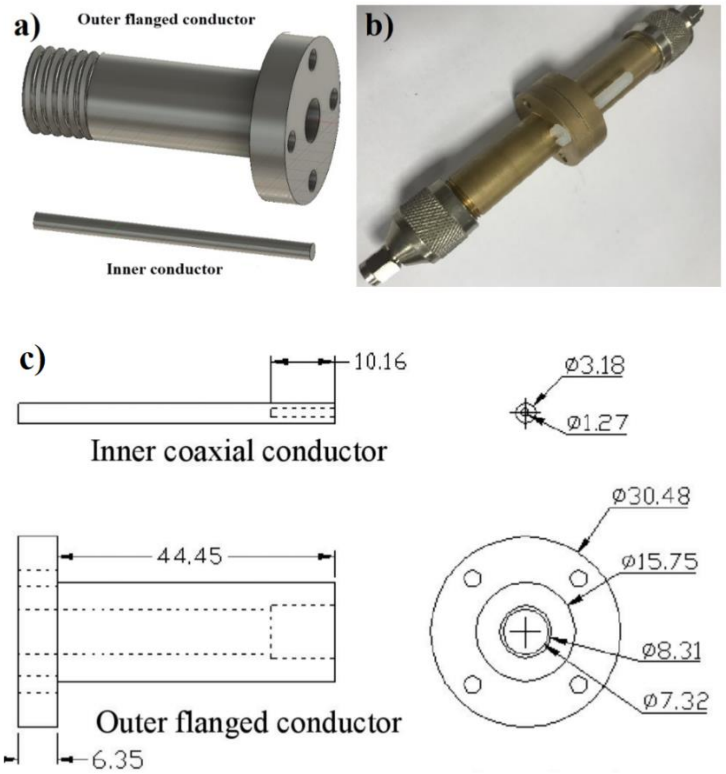

Figure 3. 15 *(a) The drawing of inner and outer conductor (b) appearance of the test fixture (c)The manufacturing drawings and dimensions of the small-sample holder for EMI shielding measurements.*

Approximately a thickness of 1.5 mm was obtained with a few plies of samples for the measurements. A vector network analyzer (Agilent E8362B) was used to measure the S_{21} parameter at the frequency range of 400 MHz to 6 GHz.

Electromagnetic shielding efficiency results are generally provided in decibel (dB) and percentage values. Hence, the following equation (Eq. 3.10) was used to convert dB values to percent.

$$\mathrm{SE}_{\%} = (1 - 10^{-\mathrm{SE}_{\mathrm{dB}}/10}) \times 100 \qquad \textit{(Eq. 3.10)}$$

Where SE% is shielding efficiency in percentages, and $\mathrm{SE}_{\mathrm{dB}}$ is shielding efficiency in Decibel.

3.8.5 Magnetic Hysteresis

In this work, a SQUID (superconducting quantum interference device) was used to measure the magnetic properties of some of the samples. The schematic representation of its working principle is given in Figure 3.16. Briefly, the superconducting quantum interference device (SQUID) forms two Josephson junctions parallelly using two superconductors separated by thin insulating layers.

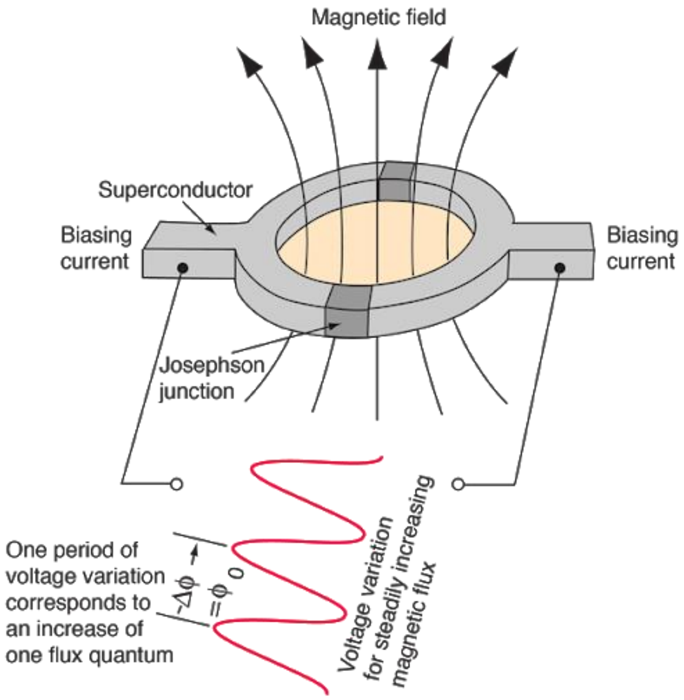

Figure 3. 16 *Working principle of SQUID magnetometer [172].*

The analyses were completed at Sheffield University by Professor Nicola Morley, as a part of Henry Royce Institute Ph.D access scheme funding, using an MPMS SQUID VSM. All measurements were carried out at room temperature between -10 and +10 kOe.

CHAPTER 4

One-Step Fabrication of Superhydrophobic PVDF-co-HFP Membranes Using Electrospinning Technique

4.1 Introduction

The electrospinning technique has been previously utilised to produce superhydrophobic nanofibre membranes [30]. The unique structure of electrospun nanofibre membranes, high porosity, and roughness provided by the randomly collected fibres, affect the wettability of the electrospun membranes, depending on the polymer used. Some of the most popular polymers explored for electrospinning to obtain superhydrophobic surfaces are polyvinylidene fluoride [173], polystyrene [174], and polysulfone [175]. However, the hydrophobic behaviour and surface tension values of these polymers may not be sufficient to achieve superhydrophobicity. Therefore, nanofillers or subsequent surface modification techniques are integrated to impart superhydrophobicity.

P(VDF-co-HFP), which has lower than 25 dynes/cm surface tension, is a copolymer of polyvinylidene fluoride and hexafluoropropylene. Thanks to the 8 fluorine atoms in each repeating unit of the polymer, it has lower than most of the common polymers [176], such as polyethylene terephthalate (42 dynes/cm), polystyrene (34 dynes/cm), polyethersulfone (46 dynes/cm), and polyamide 6 (38 dynes/cm). Thus, due to its low surface energy, it is a promising candidate for the production of superhydrophobic nanofibre membrane surfaces.

Although PVDF-co-HFP has been used to prepare superhydrophobic surfaces before, no approach has offered a one-step production technique, as with the other polymers with higher surface tension. For example, Xu *et al.* [132] employed the electrospinning technique to fabricate nanofibre membranes using a fluorinated polyhedral oligomeric silsesquioxane (POSS) /P(VDF-co-HFP) mixture. The nanofibres produced were collected on a glass substrate, and a superhydrophobic electrospun nanofibre membrane with a high degree of light transmittance was obtained. Tijing *et al.* [136] fabricated PVDF-co-HFP/carbon nanotubes (CNTs) nanocomposite nanofibre membranes to obtain superhydrophobic electrospun membranes. It was reported that the presence of CNTs contributed to the beads, and beads on string fibres, and thus the overall surface roughness increased. As a result, a higher than 156° of water contact angle was achieved. P(VDF-co-HFP)/carbon black nanocomposite nanofibre membranes were produced by Shahabadi *et al.* [177] to achieve both superhydrophobic and superoleophilic properties. A high water contact angle of 160.8°, and significantly low sliding contact angle and contact angle hysteresis values (7.0° and 5.3°, respectively) were achieved.

As observed, pure polymers without nanofillers or post-treatments do not appear to be a promising choice in achieving superhydrophobic properties. It is generally required to combine the electrospinning method with the addition of nanofillers to obtain nanocomposite layers, or subsequent surface treatment/functionalisation needs to be applied to achieve superhydrophobicity.

In this study, a one-step process, without using nanofillers or applying any post-treatment, was utilised to fabricate superhydrophobic electrospun nanofibre membranes using low-surface energy polymer PVDF-co-HFP. The proposed one-step method provided cost-effective, fast, and scalable productions compared to the multistep production methods previously proposed in the literature. The four main electrospinning parameters, applied voltage, polymer concentration, solvent, and flow rate, were varied to optimise the surface roughness properties. Additionally, contribution percentages were calculated using the Taguchi Method to understand the effect of each parameter on the surface properties and contact angle values.

4.2 Surface Imaging and Roughness of Samples

SEM images of the nanofibre membranes produced are shown in Figure 4.1. All productions provided different morphologies, including beads, smooth fibres, flat film structures, and the combination of these three primary morphologies, depending on the production and solution parameters used. It was observed that smooth fibres were formed for Ac/DMF-12.5 and Ac/DMF-15, which used the same solvent; acetone and DMF mixture (50/50 wt.%). The diameters of these fibres varied from 200 nm to 650 nm. However, although these smooth fibrous structures are promising for many applications, especially membrane filtration, they generally have relatively homogenous structure and lower surface roughness than samples consisting of both beads and fibres. DMF-10, Ac/DMF-10, DMF 12.5, DMF-15 presented a structure consisting of both fibres and beads. The diameter of fibres of these samples was between 60 and 90 nm, while the size of beads was up to several microns. The high surface tension of DMF and the low concentration values that offer lower viscosities are the main reason for these specific morphologies. It is also worth noting that much thinner fibre structures were obtained compared to other samples, which provides higher fibres per unit area. The samples, sharing the same polymer concentration of 10 wt.%, DMF-10, DMAc-10, and Ace/DMF-10, did not provide smooth fibre structures but beady fibres, because of the low viscosity of the polymer solutions trialled. Moreover, flat film morphology was obtained instead of smooth fibres or beady structures when DMAc was used as the solvent. The size of the beads on the DMAc used samples was relatively smaller compared to other beady samples with approximately between 400 nm and 2 microns.

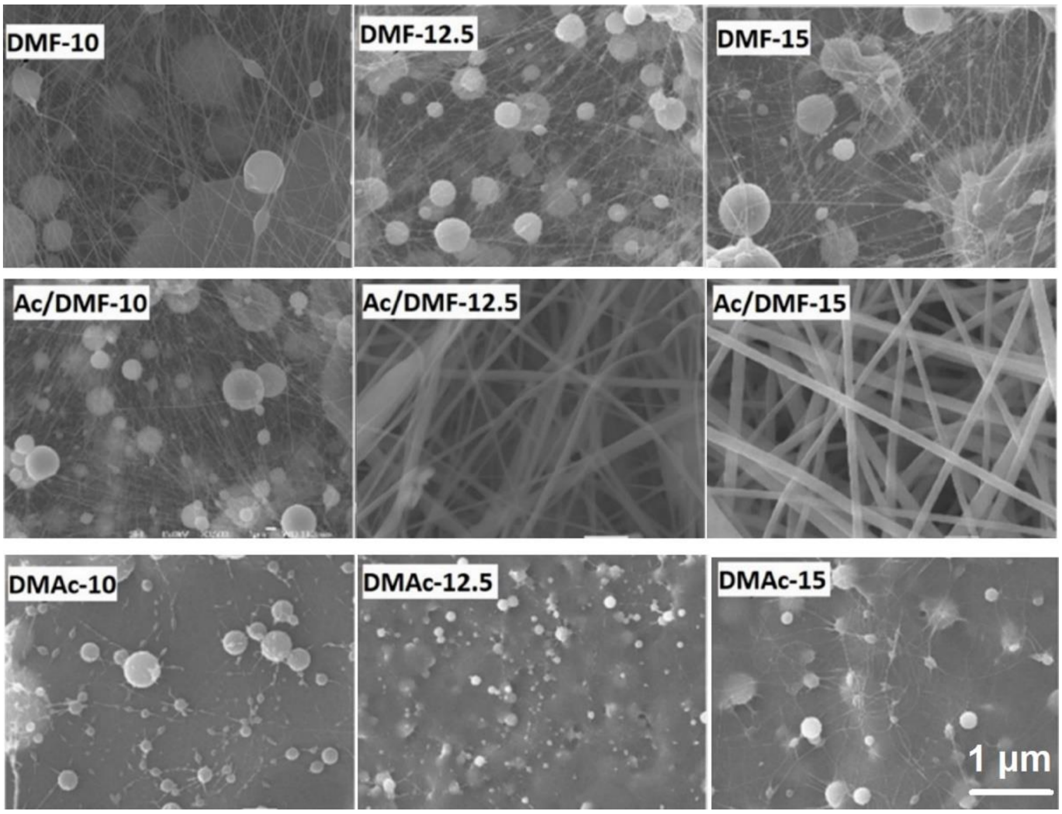

Figure 4. 1 *Surface appearances of the electrospun membranes produced (see Table 3.6 for production parameters).*

Figure 4.2 summarizes the roughness values of the electrospun nanofibre membranes with 3D topographic images of the samples having the highest (a) and the lowest (b) roughness values. It was seen that the beads and fibres significantly influenced the roughness values, as expected. The highest surface roughness was achieved on Ac/DMF-10 (5.77 µm), which only processed micro-beads structure with nanoscale fibres while the lowest roughness (0.15 µm) was obtained from DMAc-15 which had a film structure with a limited number of beads and fibres.

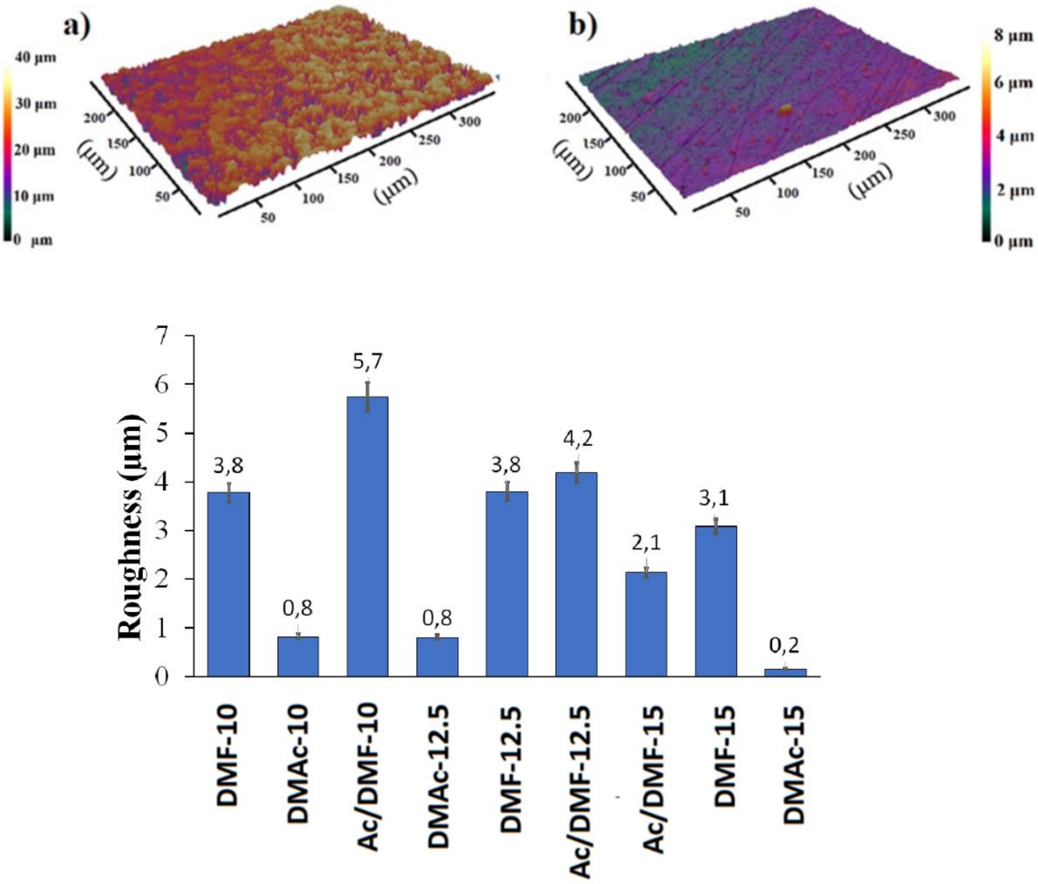

Figure 4. 2 3D topography of Ac/DMF-10(a) and DMAc-15 (b), Ra roughness values of samples (c).

It is understood from the results that the hybrid structure consisting of both beads and fibres contributes significantly to the roughness of the membranes. The other two samples, DMF-12.5 and DMF-10, which had similar morphological structures with Ac/DMF-10, exhibited close roughness values of 3.8 µm. On the other hand, DMAc-10 and DMAc-12.5, which had the film morphology with limited beads, had the second and third lowest roughness values of 0.8 µm. Thus, all three DMAc used samples were provided with the lowest roughness values regardless of production parameters, demonstrating the importance of solvent choice.

4.3 Surface Wettability Properties of the Samples

The average of five static contact angle measurements of the produced samples is shown in Figure 4.3 (a), together with the roughness values. It was seen that DMAc-10, DMAc-12,5, and DMAc-15, which had the lowest surface roughness values, had the lowest three contact angles as 113°, 112°, and 111°, respectively. Contact angles of other samples were higher than 140°, albeit only two, DMF-10 and DMF-15, were considered superhydrophobic with contact angles of 150.40° and 155.42°.

Unexpectedly, Ac/DMF-10, which had the highest roughness value of all samples, did not exhibit superhydrophobicity, but it still showed a good hydrophobic surface property with around 145°. The reason could be the effect of the size of the beads and the diameters of the fibres on the contact angle results. Although Ac/DMF-10 had the highest roughness values, the beads on the structure were too big to trap the air between the water droplet and the surface. According to the results of ANOVA and Tukey posthoc test, which are the statistical methods used to understand if the difference between three or more data groups is significant or not, the difference between DMF-10 and DMF-15, Ac/DMF-10 and DMF-12,5 and all three samples of DMAc were not significant. All other comparisons were significant statistically. The relation between the roughness and contact angles of all samples was also investigated statically, using the Pearson correlation test, which measures the statistical relationship, or association, between two continuous variables. The correlation factor, R, was higher than 0,75, which means there was a significant correlation.

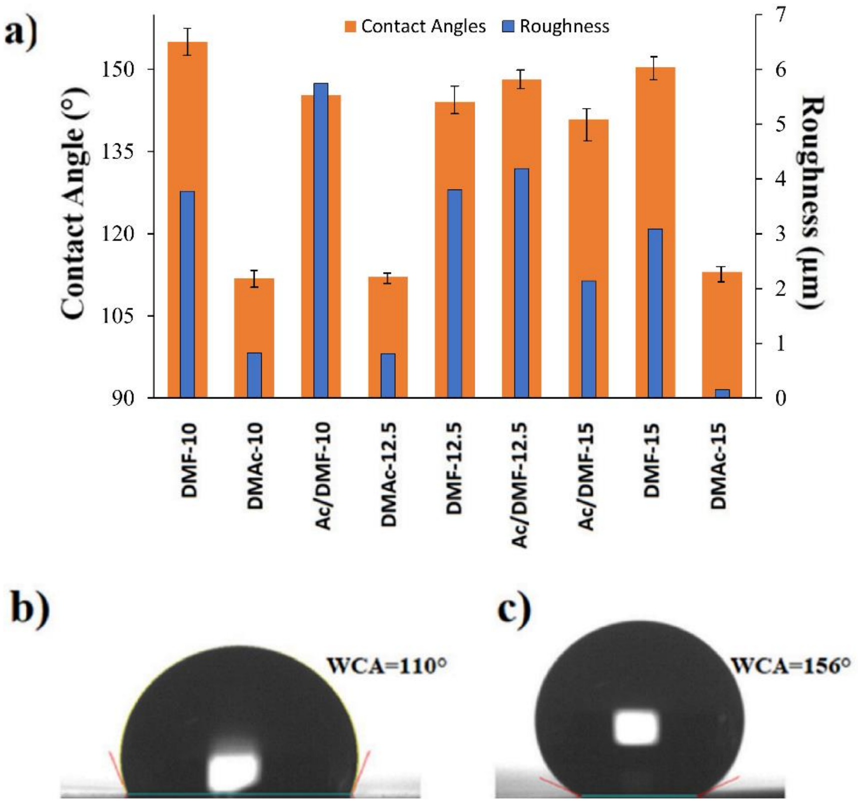

Figure 4. 3 *Contact angle and roughness comparison of the produced samples (a), contact angles of DMAc-15 (b) and DMF-10 (c).*

The advancing and receding contact angles of the samples are shown in Figure 4.4, with values collected between 1.75 and 6.25 µl sessile volume. There was a significant correlation between static and dynamic contact angle results, as expected. It was observed that the highest advancing contact angle was obtained from the sample, which had the highest static contact angle. DMAc-10, DMAc-12,5, and DMAc-15, which exhibited the lowest static contact angle values, showed the lowest advancing and receding contact angle results as well. A similar trend was also found in the sample with the high advancing contact angle. It was also noteworthy that when the volume of the sessile increased for the high advancing contact angle samples, the advancing contact angles increased. For the ideal surfaces, advancing and receding contact angles should remain constant regardless of the volume of the droplet. However, this phenomenon is not applicable for chemically heterogeneous or rough surfaces, and the sessile volume can significantly affect the measurement because of the gravitational force.

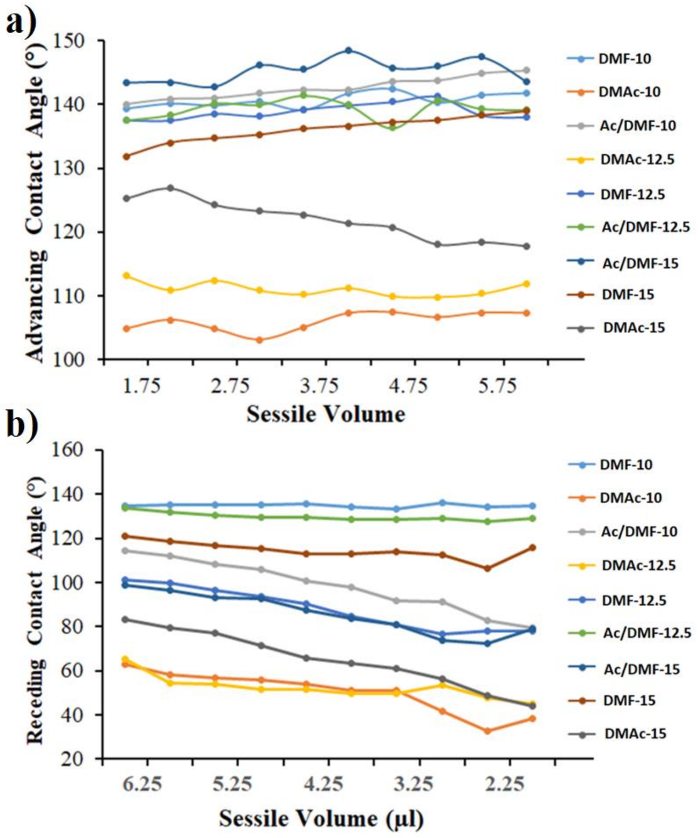

Figure 4. 4 *(a) Advancing and (b) receding contact angles of the samples.*

The calculated contact angle hysteresis (CAH) values are given in Figure 4.5. Low CAHs, which are an important indicator of the high mobility of the water droplet on the sample surface [177], were provided by three samples, DMF-15, Ac/DMF-12.5, and DMF-10. It is also notable that these samples demonstrated the highest static water contact angle values as well. Unlike other samples, these three samples revealed relatively stable CAHs regardless of the volume of water droplets. The contact angle hysteresis has thermodynamic and dynamic components. The thermodynamic component is affected by surface roughness and surface heterogeneity. These parameters lead to the drop occurring in different metastable states, which in turn translate to discrepancies in the contact angle measurement results. The dynamic component is related to the following phenomena:

- Chemical interaction of water droplet-surface,
- Penetration of the measuring liquid into the pores.

The hydrophobic nature of the PVDF-co-HFP contributed to the second component and prevented droplets from penetrating inside the pores. In addition, thanks to its low surface energy, the chemical interaction between the surface and the water droplet were minimized. Different surface morphologies and roughness values were achieved by changing production and solution parameters of electrospinning, which provided different levels of the first component. According to the results, DMF-15, Ac/DMF-12.5, and DMF-10 had the optimum surface roughness and heterogeneity level to achieve low CAH.

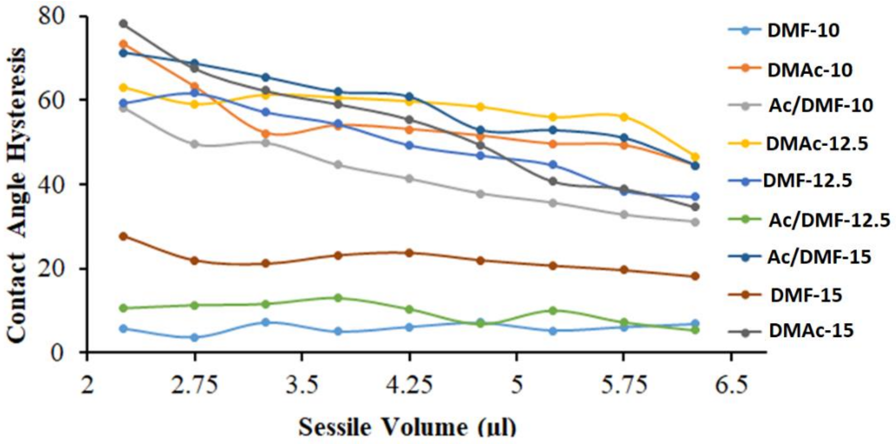

Figure 4. 5 *Contact angle hysteresis of the samples.*

Some key results published in the literature on superhydrophobic electrospun nanofibre membranes are summarized in Table 4.1. As seen, pure polymers without nanofillers or post-treatment methods are not considered promising for superhydrophobicity. Most of the methods proposed involve an additional step of functionalisation or the addition of some nanoparticles to increase the surface roughness of the fibres produced, which result in higher costs, use of chemicals and energy compared to the one-step methods. As the novel side of our study, we have managed to achieve superhydrophobicity without an additional functionalisation step or nanofiller, thanks to the hierarchical structure of electrospun nanofibre membrane and low surface energy of PVDF-co-HFP used.

Table 4.1 *Some of the up-front studies on superhydrophobic electrospun nanofibre membranes.*

Author (s)	**Materials and methods used to impart superhydrophobicity**	**CA Achieved**	**Ref.**
Yoon *et al*.	Poly (3-hydroxybutyrate-co-3-hydroxy valerate) electrospun nanofibre membranes were fabricated, and plasma treatment with CF_4 was applied to achieve superhydrophobicity**.**	158°	[116]
Islam *et al*.	PULL/PVA electrospun membranes were fabricated, then a silanization agent was used to modify the surface of the fibres and achieve superhydrophobicity.	155°	[117]
Wang *et al*.	Thermoplastic polyurethane nanofibre membranes were fabricated, then a surface immersion method with nano-silica was carried out to improve the hydrophobicity of the membranes.	156°	[118]
Malarmohan *et al*.	Polycaprolactone electrospun nanofibres were fabricated. Significant improvement of CA was reported after modification of the surface with PFDTES.	154°	[120]
Zhan *et al*.	A multi-nozzle electrospinning system was used to obtain polystyrene nanofibres and microbeads together to achieve high roughness and CA.	154°	[125]

Wang *et al*.	Three different polymers fed to the electrospinning system at the same time resulting in high surface roughness and chemically heterogeneous structures.	158.5°	[126]
Su *et al*.	Simultaneous electrospraying and electrospinning were carried out with nano-silica particles and PVDF respectively.	163°	[127]
Hong *et al*.	Nanocomposite PVDF/SiO_2 nanofibre membranes fabricated, superhydrophobicity achieved with higher than 1 wt% of SiO_2.	161°	[130]
Liu *et al*.	PVDF and ZnO nanocomposite nanofibre membranes were prepared. It was reported that it is only possible to achieve 146° CA with pure PVDF and the addition of ZnO is required to achieve superhydrophobicity.	171°	[134]
Tijing *et al*.	Nanocomposite PVDF/carbon nanotube nanofibres were fabricated, some protruding CNTs were observed on the nanofibre surface.	156°	[136]
Sun *et al*.	PVDF/modified SiO_2 nanocomposite nanofibre membranes fabricated, the effect of nanofiller amount on the wettability of the surface was investigated.	160°	[137]
Vanithakumari *et al*.	PVA/ tetraethyl orthosilicate nanofibre membrane coating on stainless steel was carried out and different surface morphologies were obtained exhibiting superhydrophobicity.	169.2° ± 2.1°	[178]

Although the proposed technique is promising to fabricate nanofibre membranes with superhydrophobicity, some challenges remain, such as low mechanical properties. It was reported previously [179] that compared to homogenous, smooth nanofibre membranes, bead-on-string structures have lower mechanical properties. Thus, developed superhydrophobic nanofibre membranes may not be suitable for harsh conditions. Moreover, to achieve superhydrophobicity by only altering electrospinning parameters, polymer selection is critical as only low surface tension polymer can provide a superhydrophobic effect using this technique, which limits the use of other types of polymers and narrows the applications areas.

4.4 Analysing of Taguchi Method Outcomes

Calculated plots of signal-to-noise ratios (SNR) are given in Figure 4.6. Minitab 17.2.1 was used to calculate these values according to the "larger is better" characteristic equation. The SNR outcomes were used for percentage contribution calculations, and results were shared in Table 4.2. A subjective method was used to evaluate the fibre formation by giving values from 1 (no fibre formation) to 4 (smooth fibre formation) and the values are given were used to calculate the signal-to-noise ratios of fibre formation ability.

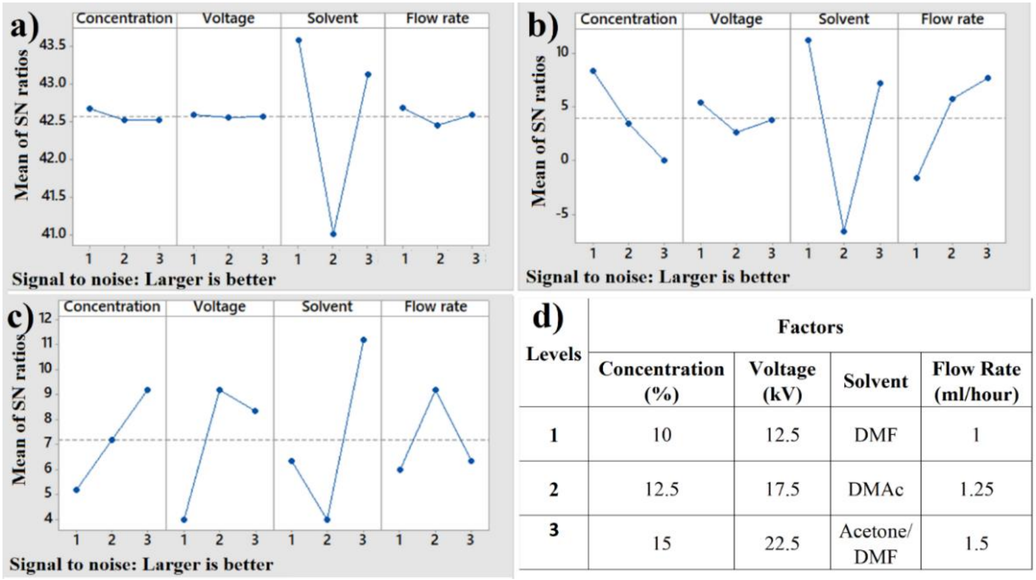

Levels	Factors			
	Concentration (%)	Voltage (kV)	Solvent	Flow Rate (ml/hour)
1	10	12.5	DMF	1
2	12.5	17.5	DMAc	1.25
3	15	22.5	Acetone/ DMF	1.5

Figure 4. 6 *Signal-to-noise plots of (a) contact angle, (b) roughness and (c) fibre formation with (d) factors and levels used.*

According to the calculations, the key parameter affecting surface wettability was suggested as the solvent used and its contribution to higher contact angle values was significantly higher than other parameters. The DMF made the highest contribution to superhydrophobicity, while the lowest contribution was made by DMAc due to its significantly low volatility and high boiling point. It was reported that the vapour pressure of DMAc is around 0.17 kPa [158]. Because it is quite low, a longer time for evaporation of the solvent and solidification step is required for the formation of fibres, compared to DMF, which has approximately two times higher vapour pressure with 0.35 kPa. Although the jet formation at the needle tip was observed during the electrospinning, a flat film morphology with a limited number of beads and fibres was obtained. It was because of the lack of solidification step, which usually takes place during the flight of the fibres from the needle tip and the collector and is significantly affected by the vapour pressure value.

Table 4.2 *Percentage contribution of concentration, voltage, solvent, and flow rates.*

Factors	**Contact Angle**	**Roughness**	**Fibre Formation**
The effect of concentration (%)	0.53	16.99	15.21
The effect of the voltage (%)	0.02	15.98	15.21
The effect of the solvent used (%)	98.6	54.09	60.86
The effect of the flow rate (%)	0.83	12.92	8.69

The reason DMF revealed the highest contribution to the high roughness values and water contact angle was another important feature of the DMF: its high surface tension. It was reported that in the electrospinning process, solvents with higher surface tension tend to result with bead and bead on string structures [38, 65, 180]. Beads and bead-on-string fibres, generally considered "defects" in electrospun nanofibre membranes, offered improved roughness and surface hydrophobicity. A hybrid structure consisting of both beads and nanofibres was obtained using DMF, an ideal combination to achieve high roughness and water contact angle values.

Taguchi calculation outcomes showed that all the parameters trialled had essential roles in the ability of fibre formation. DMF/Acetone solvent system (50:50 wt.%) could be used when it is aimed to obtain smooth fibres, which was an ideal solvent thanks to its moderate surface tension. Moreover, results confirmed that the increasing solution concentration also contributed to the formation of smooth fibres. The applied voltage and the flow rate were important in terms of smooth fibre production and the optimum values were determined as 17.5 kV and 1.25 ml/h, respectively.

Table 4. 3 *Optimum design of the factors for aimed properties.*

Aimed Property	**Solution Conc. (wt.%)**	**Applied Voltage (kV)**	**Solvent used**	**Flow Rate (ml/h)**
High roughness	10	12.5	DMF	1.50
Smooth fibres	15	17.5	DMF/Acetone	1.25
High CA	10	12.5	DMF	1.0

The effect of solvent selection and their physicochemical properties on polymer spinnability, surface wettability, and other critical properties was reported in the literature, which is consistent with our results [181, 182]. Overall, the diameter and morphology of the fibres, spinnability of the polymer solution, and crystallinity of the nanofibres obtained are affected by the solvent properties especially vapour pressure, surface tension, electrical conductivity, density, and viscosity [22].

4.5 Chemical Analyses of the Samples

Some spectroscopic and thermal analysis of the initial polymer and superhydrophobic electrospun membranes has been carried out. The primary purpose of these measurements was to verify that the superhydrophobic effect was caused by the surface change rather than a change in chemical composition.

The Raman spectra of the initial polymer and the electrospun membrane between 400 and 1600 cm^{-1} are given in Figure 4.7. Characteristic peaks for P(VDF-co-HFP) were detected at 790 cm^{-1} for the alpha phase and 840 cm^{-1} for the beta phase for both samples [154] with characteristic CH stretching vibration at 1439 cm^{-1} [183]. Two samples had identical Raman spectrums, proving there was no change during solution preparation and electrospinning process.

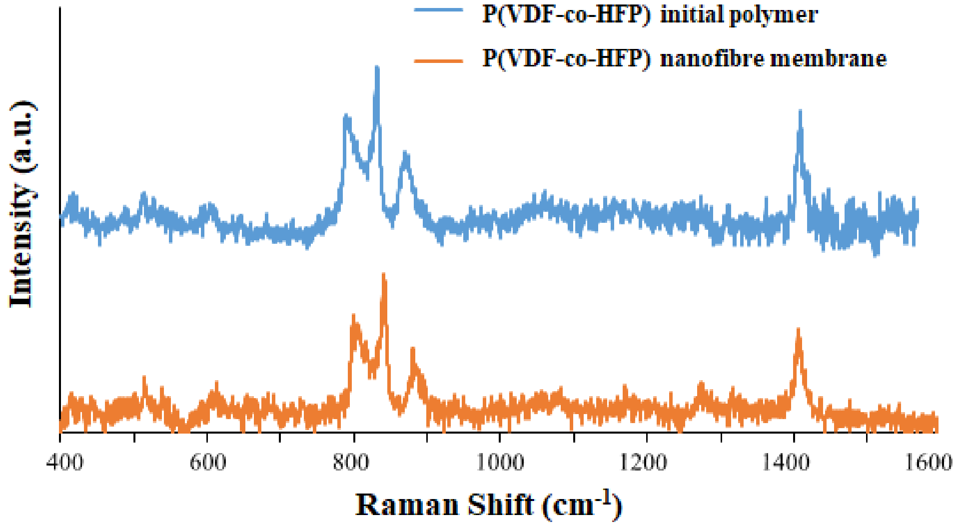

Figure 4. 7 *Raman spectra of the electrospun membrane and initial polymer.*

Moreover, FT-IR results are shown in Figure 4.8 in the region between 600 and 3200 cm^{-1}. The FTIR spectrums of initial polymer and electrospun samples were the same again, just like the Raman spectrums. There was no change in the chemical structure of the PVDF-co-HFP during the solution preparation or electrospinning process. Asymmetric and symmetric vibrations of the C-H band were observed at

2987 and 3015 cm^{-1}, respectively, for both samples. Characteristic absorption peaks of C-F were detected at 1191 and 1405 cm^{-1} [184]. The results also prove that all the solvent used during electrospinning was evaporated and did not cause any reaction during the electrospinning process.

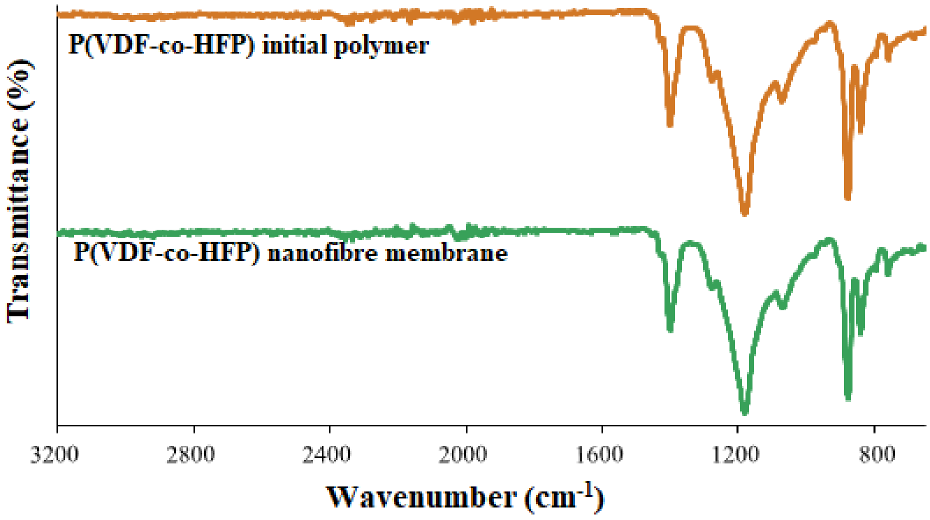

Figure 4. 8 *FT-IR spectra of the electrospun membrane and initial polymer.*

4.6 Investigation of the Thermal Properties of Electrospun Membrane and the Starting Polymers

TGA analyses were performed to compare the thermal decomposition behaviours of the initial polymer and superhydrophobic electrospun membrane. The results are given in Figure 4.9. From the heating curve, there was no significant weight change between 50 and 465 °C. The thermal decomposition of the superhydrophobic P(VDF-co-HFP) electrospun membrane occurred at around 465 °C under nitrogen. Compared with the initial polymer, there was no noticeable change in the decomposition temperature. Residual ash for both samples after 800 °C is approximately 17.5 wt.%. These results were in coherence with both Raman and FTIR results. Because no significant difference was determined on the chemical structure of the samples, the thermal properties of the samples remained the same with no noticeable change.

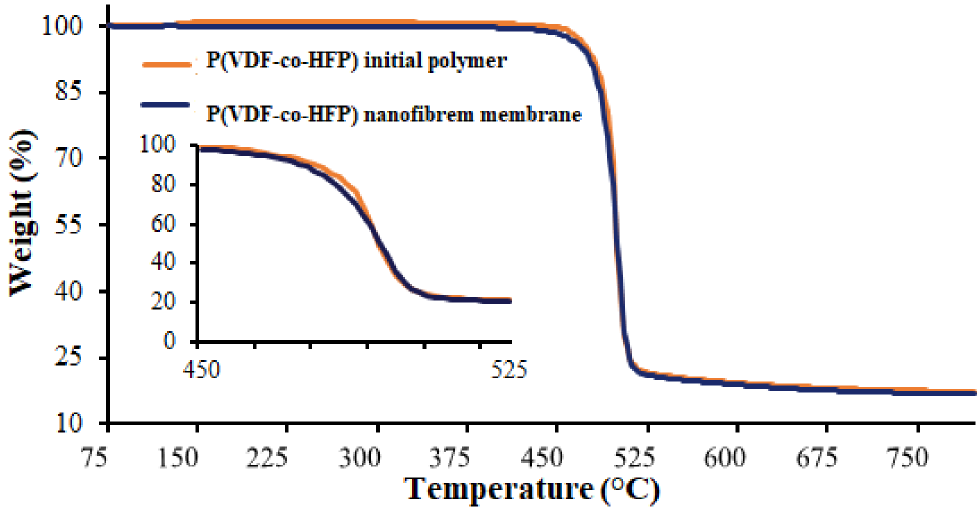

***Figure 4. 9** Weight loss (wt.%) versus temperature for nanofibre membrane and initial polymer.*

The DSC results of the initial polymer and superhydrophobic electrospun membrane are presented in Figure 4.10 (endo up). The superhydrophobic electrospun membrane indicated an endothermic melting peak at around 146 °C, which was only 1 °C lower than the initial polymer, with a melting enthalpy ($\Delta H_{melting}$) of 26.28 J/g. The crystallinity of the nanofibre membrane is calculated as 25.10%, assuming $\Delta H_{melting}$ 100% crystalline P(VDF-co-HFP) as 104.7 J/g [185].

The specific heat capacity of the initial polymer and nanofibre membrane between 30 and 110 °C is shown in Figure 4.11. As expected, specific heat capacity increases with the increasing temperature. The specific heat capacities of the initial polymer and nanofibre membrane were approximately 1.10 J/(g.°C) and 1.16 J/(g.°C) at 30 °C, respectively. Additionally, the thermal analyses confirmed no solvent or contamination left after electrospinning, and the crystallinity degrees have remained the same. The slight change in specific heat capacities was considered as the effect of higher surface area.

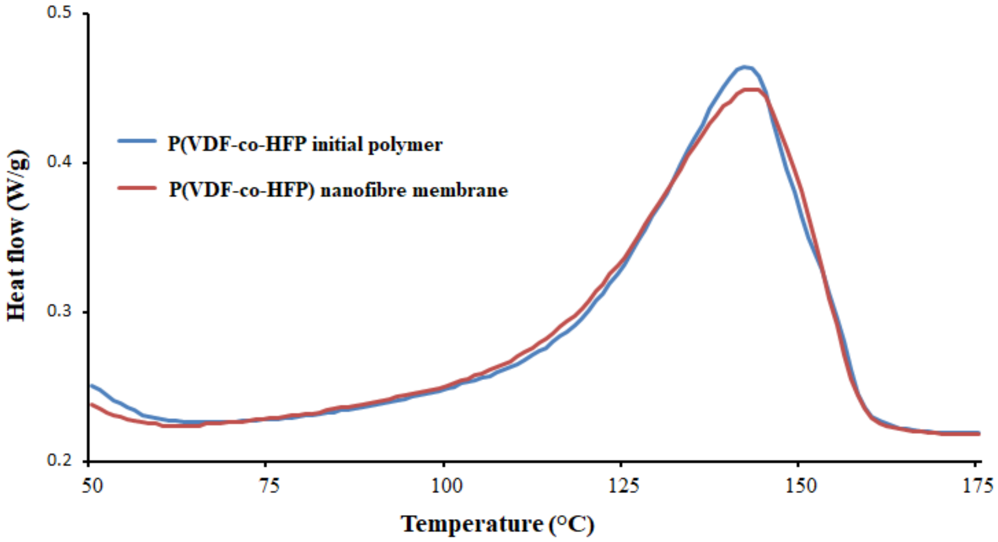

Figure 4. 10 *DSC result of the nanofibre membrane and initial polymer.*

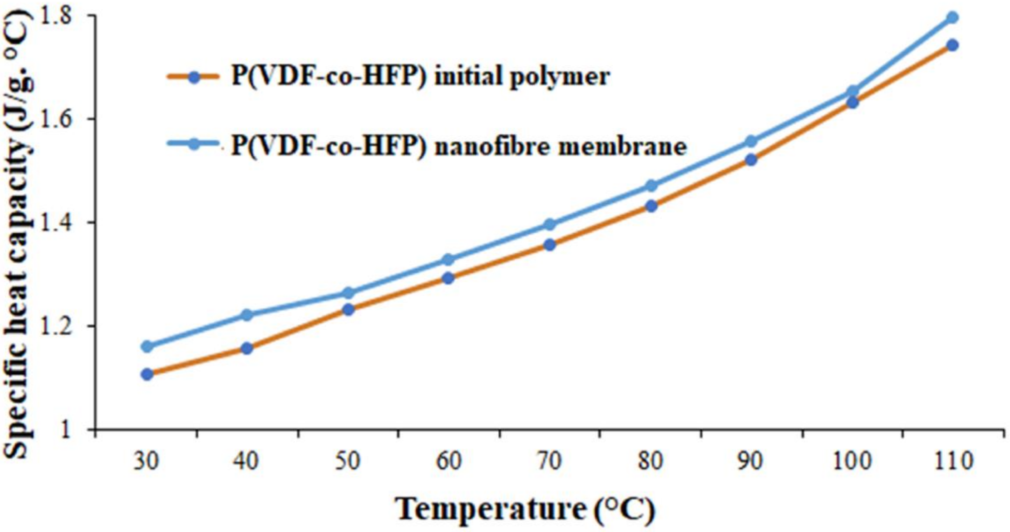

Figure 4. 11 *Specific heat capacity of the nanofibre membrane and initial polymer at different temperatures.*

4.7 The Role of Solution and Production Parameters on Surface Morphology of PVDF-co-HFP Electrospun Membrane

Solution parameters (such as viscosity, surface tension, volatility of the solvents, the chemical structure of the solvents, molecular weight of the polymer used etc.) and production parameters (such as applied voltage, the distance between nozzle and collector flow rate etc.) are the major parameters that affect the electrospinning process. It is possible to obtain polymer surfaces with different structures such as fibres, beads, ribbons, or even flat films, by altering these major parameters [186, 187].

All three solvents chosen to dissolve PVDF-co-HFP had quite similar solubility parameters. All of them were considered suitable solvents for PVDF-co-HFP before by several research groups. The Hansen solubility parameters have been used to confirm the solubility of a polymer in the three different solvent systems. It is related to the following interactions:

- δ_p (polar forces between molecules)
- δ_p (molecular dispersive power) and,
- δ_h (hydrogen bonds)

Hansen solubility parameters of PVDF-co-HFP, acetone, DMF, DMAc and DMF:acetone mixture and calculated $\Delta\delta_{iP}$ values of the solvents are given in Table 4.4. To calculate the interaction between polymer and solvent system ($\Delta\delta_{iP}$), Equation (4.1) has been used.

Table 4.4 *Hansen solubility parameters and calculated* $\Delta\delta_{iP}$ values of the chemicals used.

	$\boldsymbol{\delta_d}$	$\boldsymbol{\delta_p}$	$\boldsymbol{\delta_h}$	$\boldsymbol{\Delta\delta_{iP}}$
PVDF-co-HFP	17.2	12.5	8.2	-
Acetone	15.5	10.4	7.0	2.96

DMF	17.4	13.7	11.3	2.56
DMAc	16.8	11.5	10.2	2.27
Acetone/DMF (1:1)	16.4	12.1	9.2	2.46

$$\Delta\delta iP = [(\delta \mathrm{pi} - \delta_{\mathrm{pP}})^2 + (\delta \mathrm{di} - \delta_{\mathrm{dP}})^2 + (\delta \mathrm{hi} - \delta_{\mathrm{hP}})^2]^{1/2} \qquad (Eq.\ 4.1)$$

Where *i* and *p* are solvents and polymer, respectively.

According to the results, it was found that the solubility of the polymer in these three solvents is significantly enough. So that the level of the solubility of the PVDF-co-HFP in these solvents was not a parameter, but the effect of their properties, such as viscosity and the surface tension, was discussed.

Beads and beaded fibres contribute to the surface roughness and provide additional properties. The formation mechanism of beads and beaded fibres is related to production and solution properties and the jet instabilities during the electrospinning process. There are mainly three types of jet instability during the electrospinning process. Generally, it is believed that Varicose and Rayleigh types of instabilities are beneficial for the amount and formation of the beads, while the whipping instability mainly reduces the number of them. If these three types of instabilities are dominant during electrospinning, it is possible to obtain hybrid structures with beads and fibres [179].

Surface tension, charge density and viscosity are the main parameters that can easily cause these three types of instabilities, and thus, bead formation is mainly related to these factors [179, 188]. The outcomes of the Taguchi experimental design of our study confirmed this information. The solvent used had a significant role in the formation of the beads, with a contribution percentage of 50%, followed by the applied voltage and solution concentration. The whipping instability is caused by the electrical forces on the outer surface of the jet. It fluctuates the surface charge, and when it overcomes a threshold, the jet splits into numerous smaller branches and provides nanoscale polymer fibres.

An adequate charge density is critical during electrospinning to provide the stretching force to elongate the solution. If the charge density is not adequate, low elongation will cause Raleigh instability, resulting in bead formation. The schematic representation of the formation of beads by the charge density during electrospinning is given in Figure 4.12.

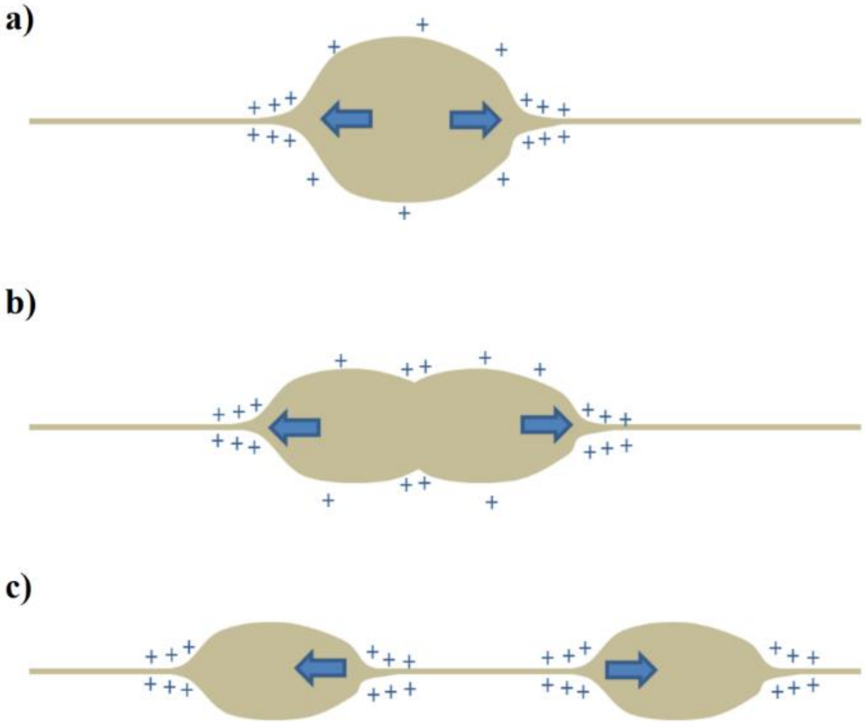

Figure 4. 12 *Schematic representation of the formation of beads during electrospinning process (a) repulsive force at both ends of the bead, (b) splitting apart of the bead and the increasing charge density at the centre (c) moving further apart of the beads because of the charge concentration at the ends.*

It is also notable that the samples with the lowest polymer concentrations (DMF-10, DMAc-10 and Ac/DMF-10) also provided beady structures. Additionally, according to the Taguchi outcomes, the concentration used was the second most important parameter that plays a role in preparing rough surfaces. The effect of the low polymer concentration on the bead formation was discussed before by several groups [188-191]. The main reason for this phenomenon is the relation between solution viscosity and polymer concentration. When the viscosity of the solution is low, the process turns into electrospraying from electrospinning. There is a critical value of polymer concentration in which both fibres and beads are produced together. Above that critical value, it is possible to achieve smooth fibre or below it, only beads can be obtained (Figure 4.13).

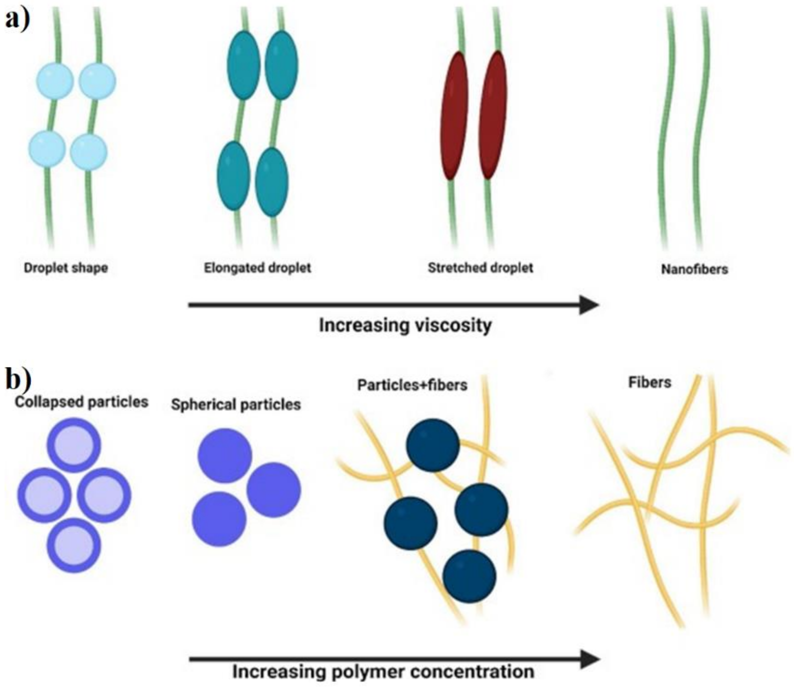

Figure 4. 13 *The effect of (a) increasing viscosity and (b) increasing polymer concentration on bead formation [192].*

As seen from the SEM and 3D profilometer results, beads are the main factor that provide higher surface roughness. They caused a chaotic surface structure with the contribution of bead and fibre mixtures instead of a relatively smooth surface with the contribution of only fibres. The schematic illustration of chaotic beads and fibres structure is given in Figure 4.14.

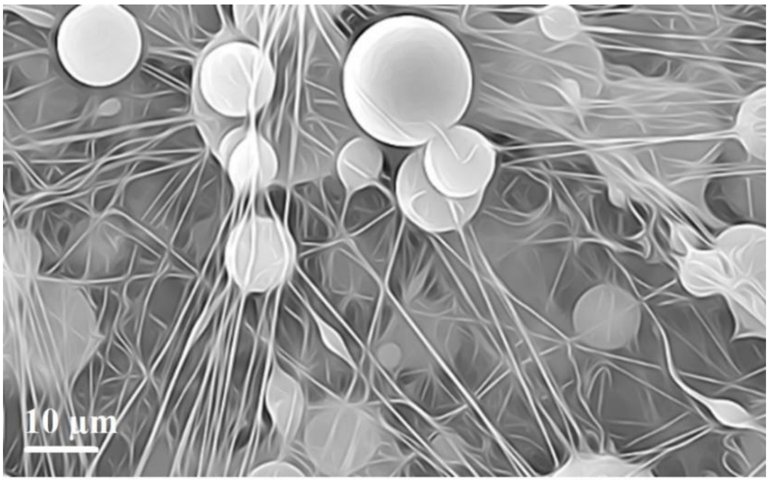

Figure 4. 14 *Schematic illustrations of chaotic beads and fibre structure.*

The surface height profiles of DMF-10, which consists of fibres and beads together, and Ac/DMF-15, which consists of only smooth fibres, are given in Figure 4.15. It is clear that the presence of the beads significantly contributed to the roughness of the surface. The sample without beads had much lower surface height profiles compared to the sample Ac/DMF-15.

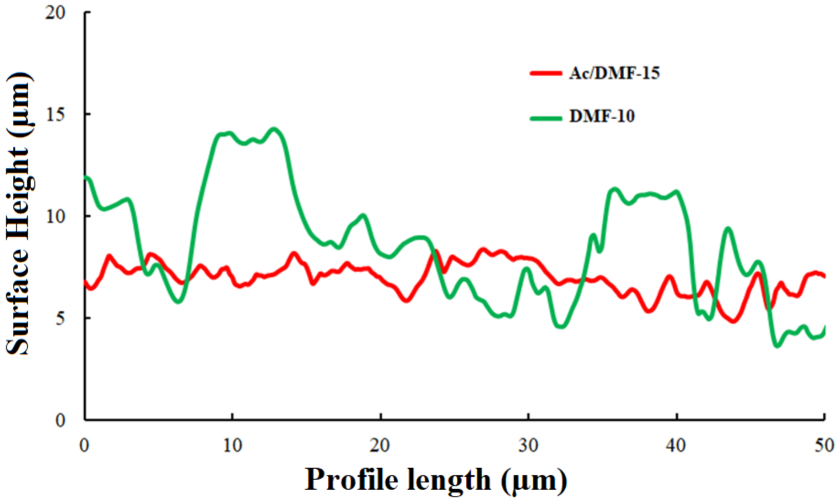

Figure 4. 15 *The surface height profiles of DMF-10 and Ac/DMF-15.*

The samples of DMF-15, DMF 12.5 and DMF-10, were provided with much chaotic and rough surfaces because of the bead structures with smooth fibre formation. The main reason was the surface tension of the solvent used for these samples, which was DMF. When the surface tensions of the solutions are considered, it can be seen that DMF has the highest surface tension compared to DMF/Acetone mixture and DMAC (Some key properties of the solvents used are given in Table 3.1). The addition of 50 wt.% of acetone to the DMF offered a lower surface tension, explaining why the smooth, non-beady samples were obtained from DMF and Acetone mixtures. According to the literature [193], the surface tension of the DMF/acetone mixture (1:1 by volume) is around 30.6 mN·m-1 which was much lower than DMF.

Additionally, in the electrospinning process, solution viscosity and surface tension are two main parameters of whipping instability, which leads to the jet splitting into many small branches [179]. Due to the splitting of the jet, much narrower fibres (lower than 50 nm) were obtained from the solutions with lower concentrations (DMF-10 and Ace/DMF-10) and from the solutions with higher surface tension (DMF-10, DMF-12.5, and DMF-15). However, DMAc-10 was an exception: when DMAc-10 was used as a solvent, solidification could not be completed, and mostly film structures were obtained instead of narrower fibres. It is believed that the main reason is the very low vapour pressure of DMAc (0.17 kPa at 20 °C) which limited the evaporation of the solvent during the flight of the jet, between the needle and the collector.

Similar results were obtained by Supaphol's group about the effects of solvents on the electrospinning process of polystyrene solution and obtained polystyrene surface morphologies. It was reported that the surface morphology of the polystyrene nanofibres was majorly dependent on the solvent used for the electrospinning process, and some properties of the solvent have a significant influence on the electrospun membranes surface properties [194]. Additionally, Reneker's group [195] reported that alongside fibre and bead structures, branched fibres, flat ribbons, ribbons, and some other specific morphologies could be obtained through the electrospinning process. The solvent used is considered as the significant parameter to the formation of the different morphologies.

4.8 The Influence of surface morphology on superhydrophobicity of PVDF-co-HFP electrospun samples

The chemical composition and roughness of a surface determine the surface wettability properties. In this chapter, the chemical composition of electrospun membranes remained the same, while the surface roughness properties of the membranes changed with the changing electrospinning parameters. Thus, this section discussed the effect of surface roughness rather than the chemical compositions. The roughness can affect the contact angle in two different ways: (i) with the increasing surface areas and (ii) with the sharp edges surfaces consisted.

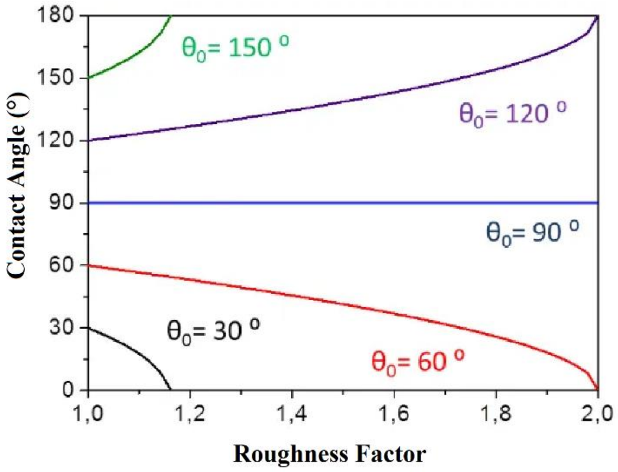

Figure 4. 16 *Contact angle values (θ_0) of rough surfaces as a function of roughness factor (R_f) for different smooth surface contact angle materials (adapted from [196]).*

For a polymeric membrane produced by electrospinning, the effect of sharp edges is negligible. On the other hand, if the droplet size is smaller than the roughness details, it will not affect the contact angle as well. However, in our study, the size of the water droplet was much bigger than the details of the roughness. Thus, there must be a significant effect of the roughness on the contact angle values of the samples. The effect of the roughness on surface wettability for various contact angles of smooth surfaces is given in Figure 4.16.

As known, when the contact angle of a smooth solid surface is lower than 90°, it is considered as a wettable surface. If the surface of the same material is roughened, the contact angle will decrease and become even more wettable. On the other hand, if a smooth solid surface has a greater than 90° of contact angle, it can be considered a non-wettable surface. When the surface of the same material is roughened, it provides higher contact angles and becomes more non-wettable. Wenzel already provides this relation between the contact angle and surface roughness:

$$\cos\ \theta = R_\mathrm{f} \cos\ \theta_0 \qquad \textit{(Eq.4.2)}$$

where R_f is $\frac{A_\mathrm{SL}}{A_\mathrm{F}}$ (A_SL is a solid-liquid contact area, and A_F is a flat contact area).

As seen, cos θ is negative for contact angles greater than 90°; according to this equation, the apparent contact angle is larger. However, this equation is only valid for the Wenzel state and according to this equation, all rough surface wets by the water, and it is assumed there is no air pockets left after water contact. The effect of the air pockets is considered by using the Cassie-Baxter equation, by considering the composite interlayer (consisting of two fractions, solid-liquid interface (f_{SL}) with a contact angle of θ_{SL} and air-liquid interface(f_{AL}) with a contact angle of θ_{AL}) according to the equation below [197]:

$$\cos\ \theta = R_\mathrm{f} f_\mathrm{SL} \cos\ \theta_0 - f_\mathrm{LA} \qquad \textit{(Eq.4.3)}$$

where $f_\mathrm{SL} + f_\mathrm{AL} = 1$. The schematic representation of the composite interlayer is also given in Figure 4.17.

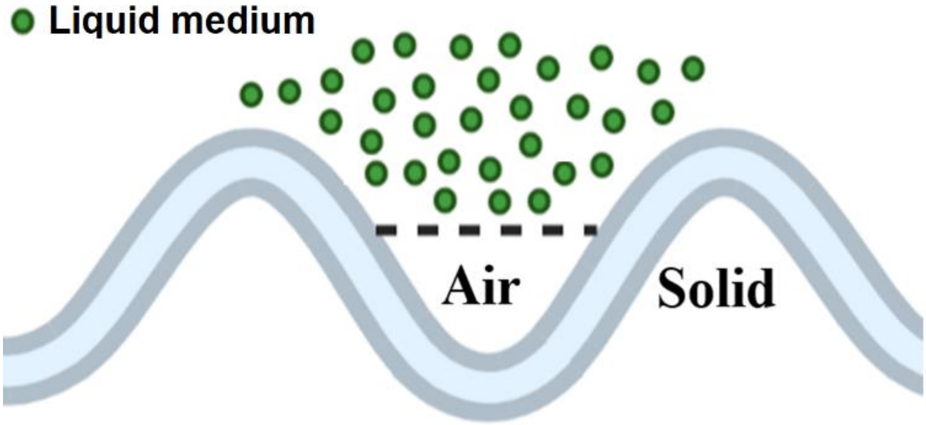

Figure 4. 17 *Formation of the composite solid-liquid-air interface in Cassie-Baxter state.*

As the smooth PVDF-co-HFP surface provide higher than 90°of contact angle [198], it was possible to increase the contact angle by roughening the surface, which led to a change in the ratio of f_{SL} and f_{AL} by changing the electrospinning parameters, it was possible to produce electrospun membranes with different surface morphologies, structures, and roughness values. The numbers, size and homogeneity of beads and diameter of the fibres are considered the two main factors in electrospun membranes that provide higher roughness values. When the roughness increases, the effective free energy of the solid/liquid interface also increases, making the surface more hydrophobic [199]. It was clear that the presence of microbeads had a critical effect on roughness. The main reason was the increasing f_{AL} which meant higher air pillows between the surface and water droplet. DMF-10, Ac/DMF-10, DMF-12.5 and DMF-15, which had a good mixture of beads with fibres, revealed the higher roughness values, and their contact angle values were much higher than the others having lower roughness values. Figure 4.18 summarized the effect of the roughness on hydrophobicity

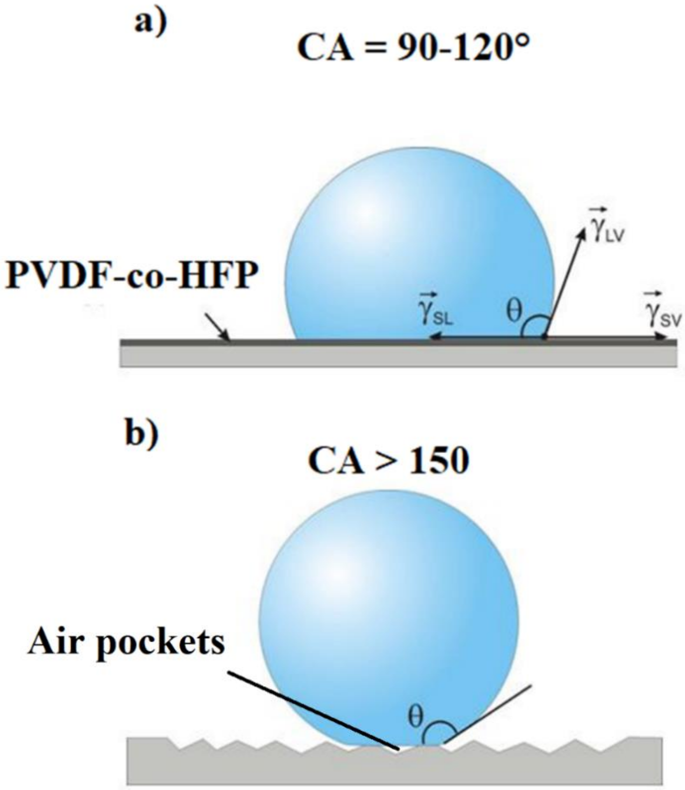

__Figure 4. 18__ Schematic representation of the effect of surface structure on contact angle (a) flat PVDF-co-HFP (90~120°) and (b) high-roughness surface PVDF-co-HFP (>150°).

The second factor affecting the hydrophobicity of the electrospun membrane was the diameter of the fibres. When the fibre diameter decreases, the numbers of the fibres increase, meaning more fibres in a unit area. From SEM analysis, DMF-10, Ac/DMF-10, DMF-12.5 and DMF-15 had much narrower fibres (less than 50 nm) than the other fibrous membranes. This structure prevented water droplets from being infused through the gaps; as the fibre diameter decreased and the numbers of fibres increased, the gaps also decreased. Smaller and denser air gaps make it hard for the droplets to infuse into the structure, as indicated in Figure 4.19.

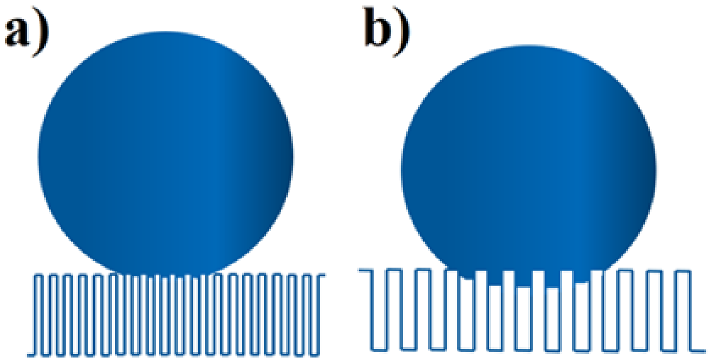

Figure 4.19 *Schematic illustration of the effect of fibre gaps on the contact angle of the electrospun membranes (a) with small gaps and (b) with large gaps.*

4.9 Summary

In the first part of the study, superhydrophobic PVDF-co-HFP membranes were fabricated in a one-step electrospun process. Compared to the literature, no nanofillers, post-treatment methods or additional functionalization steps were used to achieve superhydrophobicity which was the novelty of this work. It was also confirmed by the FTIR, Raman and thermal analysis results, that the electrospinning process did not affect the chemical structure or properties of the polymer used. However, it was also found that the parameters used had a significant effect on the electrospun membranes' surface properties. The selection of the solvent played a critical role in the surface wettability properties of the membranes, due to their dominating effect on the morphology and surface roughness values; a result of the key properties such as vapour pressure, surface tension, boiling point, and dielectric constant. These properties of the solvents created some instabilities during the electrospinning process, resulting in the formation of beads. The hybrid fibre and bead structure provided the Wenzel state, and the composite liquid-surface interface produced increased roughness values. We used the Taguchi method to investigate the contribution of key factors in surface roughness, water contact angle, and fibre formation. We found that it was possible to produce superhydrophobic PVDF-co-HFP membranes with low contact angle hysteresis without any additional filler, subsequent surface treatment, and functionalization. It was also demonstrated that the surface superhydrophobicity of the produced membranes was attributed to the specific structures consisting of beads and nanofibres. Overall, optimized designs for higher contact angle, higher roughness, and smooth fibre production, were calculated and presented in the study.

CHAPTER 5

Electrospun Nanofibre Membrane Based Transparent Slippery Liquid-Infused Porous Surfaces with Icephobic Properties

5.1 Introduction

The important question of possible relationships between icephobicity and superhydrophobicity has been discussed by researchers over the last decade. It has been shown that superhydrophobic surfaces which exhibit the Wenzel state can be promising for icephobic applications. However, the mechanism of the icephobic effect is different from the superhydrophobicity. Thus, specific material designs with different mechanism concepts need to be used to achieve sufficiently low ice adhesion strength. Using SLIPS for icephobic applications is a promising topic, and there have been many improvements since it was proposed by Aizenberg [10].

Although several challenges remain for applying SLIPS in harsh conditions, such as evaporation of lubricants, the durability of the structure, or the contamination of the surface with dust, the production of significant icephobic properties has been achieved. However, although the selection of lubricants for SLIPS is relatively easy, the formation of the porous structure is still an important challenge, which consists of both the selection of the material and the method to produce the porous structure.

Many valuable works have been undertaken, focusing on the production of porous structures for SLIPS [199-203], as self-assembly [204, 205], laser writing [206], phase separation [207], and electrospraying [208] methods have all been used to fabricate the porous part of the SLIPS. However, although the methods proposed are reasonably efficient, some disadvantages remain, such as the necessity for high laser energies [209], technical barriers for large-scale implementations [210], and limitations in polymer selection [211].

On the other hand, for the application of icephobic materials on windows, curtain walls or energy harvesting systems, transparency is of critical importance [212]. When the icephobic layer does not have enough optical transparency, it can prevent sunlight from reaching the solar system, and a significant reduction in efficiency can occur. However, the studies that have considered transparency while designing icephobic surfaces are relatively limited [213-215]. Wu *et al.* fabricated optically transparent icephobic surfaces using bio-based epoxy. It has also been reported that the fabricated surface revealed a 50 kPa of ice adhesion strength at -20 °C, and the transparency of the surface was around 81% [212]. Self-cleaning and transparent icephobic coatings were produced by Chen *et al.* using modified SiO_2 nanoparticles. Approximately 58 kPa ice adhesion strength was achieved at -15 °C, and the transparency of the surface was reported as high as 97.8% [213]. In another study, porous cellulose lauroyl ester films were fabricated by Chen *et al.* using a nanoprecipitation technique. Perfluoropolyether was used as the lubricant, and optical transmittance of 30-80% was achieved with effective de-icing properties [214].

In this study, unlike previous studies, we designed and produced the porous structure of the SLIPS via a simple, cost-effective, and scalable electrospinning technique, instead of previously proposed complicated, high-energy required and expensive methods as mentioned above. Freestanding, highly porous nanofibrous polymeric lightweight surfaces were obtained to fabricate transparent icephobic SLIPS. Three types of lubricants (silicone oil, fluorinated oil, and paraffin liquid) were used to prepare the SLIPS. We investigated the key properties, including droplet icing time, ice adhesion strength, and optical transmittance in the visible light spectrum.

5.2 Surface Imaging and Topography of the Nanofibre Membranes

Porous fibrous membrane and high porosity between the fibres (71.6 ±4.1%) were obtained from the electrospinning process, as shown in Figure 5.1. The total porosity of the membrane was calculated using bulk mass and true mass of the sample using the following formula, where ρ_{Bulk} is the bulk density and ρ_{True} is the true density:

$$\%Porosity = \left(\frac{\rho_{Bulk}}{\rho_{True}}\right) \times 100 \qquad \textit{(Eq. 5.1)}$$

It was reported by Gaharwar *et al.* [216] that nanofibre membranes with beady structures tend to exhibit lower mechanical properties. Because the smooth fibre structures provide better mechanical properties [216] than beady membranes, production parameters optimized according to the Taguchi method in Chapter 4 were used for these productions.

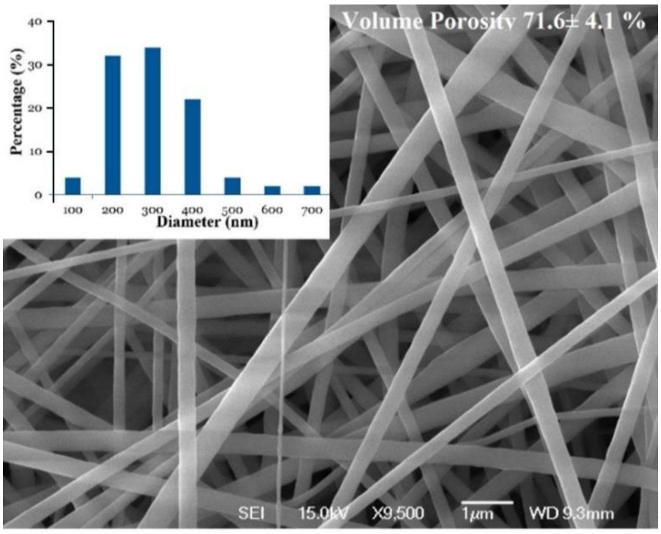

Figure 5.1 *SEM analyses of the as-prepared electrospun membrane (Inset: distribution of fibre diameter).*

The average fibre diameter was found as 330 ± 63 nm, and more than 90% of the fibres had a diameter range between 100 and 400 nm, which can offer a high surface area. It is important because the high surface area can provide more contact area between the lubricant and the fibres, resulting in good oil storage. Additionally, because the PVDF-co-HFP fibres are highly oleophilic, a higher contact area can offer a better capability of containing the lubricant, which is one of the primary concerns of SLIPS.

Surface height profiles of the samples, before and after lubricant infusion, are shown in Figure 5.2. It was found that the membrane surfaces without lubricant had the maximum peak-valley heights of approximately 15 μm. The pores in the structures provided the valleys, while the overlapping fibres provided the peaks.

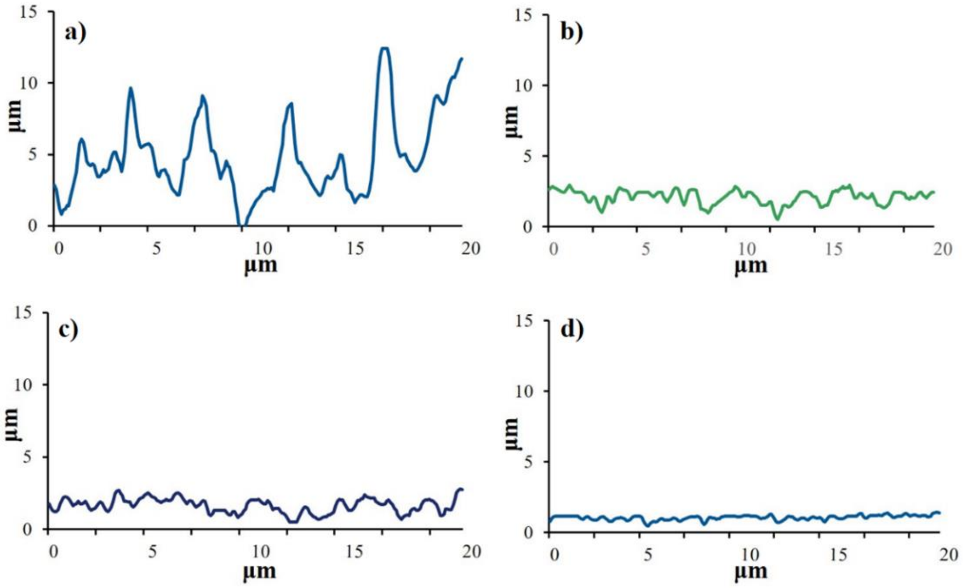

Figure 5.2 *Height profiles of the (a) PVDF-co-HFP electrospun membrane and SLIPS with (b) silicone oil, (c) paraffin oil, and (d) PcTFE.*

After the infusion of the lubricants, the maximum peak-valley heights of the samples had decreased to approximately less than 3 μm range, which is an indication that the lubricant had filled most of the pores. The schematic representation of the roughness of nanofibre membrane before and after lubricant infusion and the effect of over-coating is given in Figure 5.3. As seen, after infusion of lubricants, all pores were filled with it, and a thin oil layer over-coated the electrospun membrane. This is an essential criterion for SLIPS structures to exhibit their unique properties.

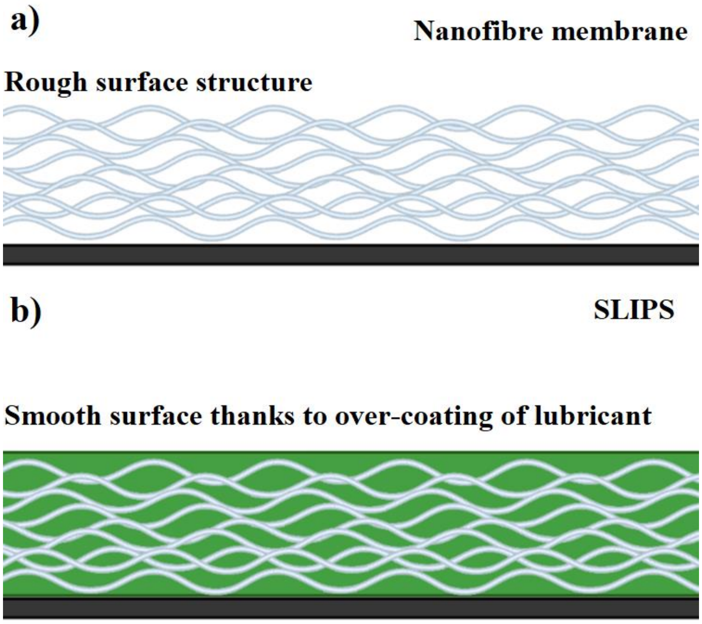

Figure 5. 3 *Schematic representation of roughness of (a) PVDF-co-HFP and (b) SLIPS.*

As seen once the pores filled with the lubricant, SLIPS achieved a much smoother surface structure than nanofibre membrane. All SLIPS exhibited low peak-valley heights, and there was no significant difference between the three lubricants explored, according to height profiles. It was mainly because the viscosity values (870, 1000 and 910 mPa.s for PcTFE, silicone oil and paraffin wax respectively) and the oil contact angles (2, 5 and 0° for PcTFE, silicone oil and paraffin wax respectively) of these three lubricants with nanofibre membrane were quite close. All three lubricants had similar behaviour inside the porous structure.

As the height profiles were measured around 24 hours after lubricant was infused, it was also clear that the lubricants were not too volatile inside, which was confirmed with the low vapour pressure values of 0,0017, 0,6 and 0,13 for PcTFE, silicone oil, paraffin wax respectively. The nanofibre membrane was a good porous structure to keep the lubricant inside the pores. The 3D topographic images of the samples, which were measured using a Zeta-20 optical profilometer, are given in Figure 5.4. The fibrous structure of the electrospun membranes can be reflected in Figure 5.4 (a), a lubricant-free structure. After the infusion of the lubricant, no fibrous structure could be observed. The roughness of the electrospun membrane also decreased dramatically, consistent with the height profile results.

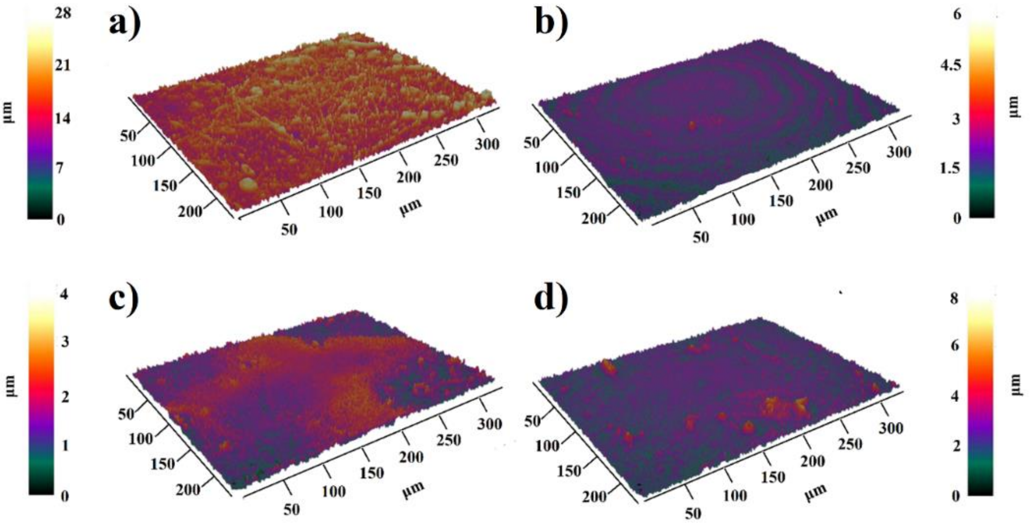

***Figure 5.4** 3D topographic images of (a) PVDF-co-HFP electrospun membrane (b) SLIPS with PcTFE, (c) SLIPS with silicone oil, and (d) SLIPS with liquid paraffin.*

5.3 Surface Wettability of the Samples and Droplet Mobility on the surfaces

Water contact angles of the PVDF-co-HFP and SLIPS are shown in Figure 5.5. The electrospun PVDF-co-HFP membranes possessed an average contact angle of 141.2° which was quite close to the superhydrophobic region, thanks to its fluorinated structure, offering low surface energy. However, there was a significant reduction after the infusion of the lubricants. The SLIPS containing PcTFE, silicon oil, and paraffin oil exhibited water contact angles between 102-110°, which were much lower than PVDF-co-HFP itself, but still in the hydrophobic region. The reason for this reduction was the lower surface roughness values and the effect of infinite soft substrate (lubricants). As known, it is only possible to achieve 120° of water contact angle using a soft and homogenous structure according to the Youngs equation [73]. To exceed 120°, surface roughening has to be carried out. Thus, it was expected to have a lower than 120° of contact angle from the SLIPS prepared, as the lubricant infusion inside the pores of the electrospun membranes provided a much smoother surface structure.

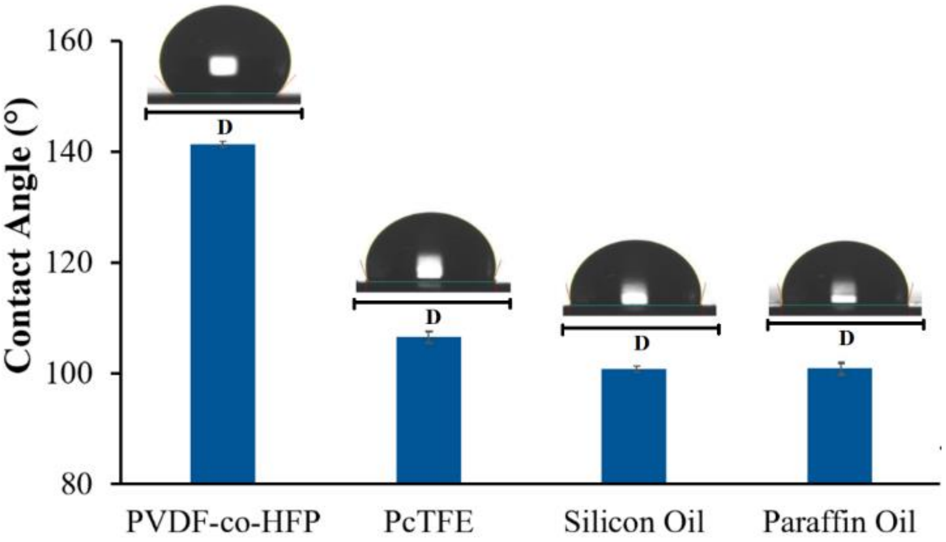

Figure 5.5 *Static contact angles results of the as-produced membrane and SLIPS (D=3.0 mm).*

Contact angle hysteresis of the samples is shown in Figure 5.6. Although the PVDF-co-HFP provided the highest static water contact angle (141.2°) thanks to fluorinated chemical composition and rough surface structure, it also offered the highest contact angle hysteresis, which was around 49° at the 2.25 µl sessile volume, and 35° at 5.25 µl sessile volume. As explained before, higher contact angle hysteresis means lower water droplet mobility, making the high static contact angle values almost useless. Additionally, the ice adhesion strength is mainly related to the mobility of the water droplet on the surface, rather than the static contact angles. Several times [8], it was reported that obtaining high water contact angle values is not significantly improving icephobicity. However, it is critical to achieving good droplet mobility on the surfaces to obtain icephobic surfaces.

On the other hand, although lower static contact angles have been achieved with SLIPS, they also offered much lower contact angle hysteresis than PVDF-co-HFP itself. Therefore, good mobility of water droplets on the SLIPS surface is achieved. At the 5. 25 µl of sessile volume, all SLIPS provided around 6° of contact angle hysteresis.

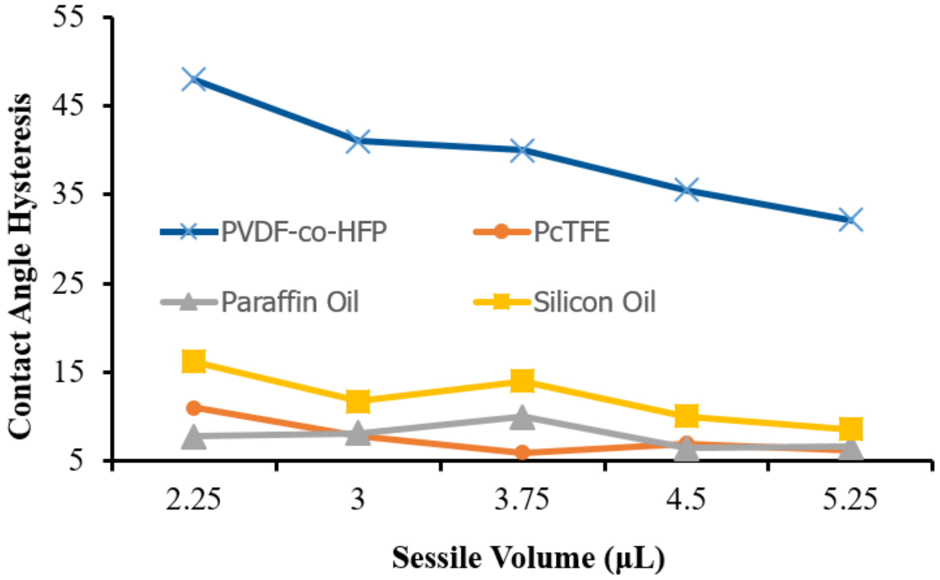

Figure 5.6 *Contact angle hysteresis of PVDF-co-HFP nanofibre membrane and PcTFE, paraffin oil and silicon oil SLIPS.*

The surface roughness and chemical composition of the samples were changed significantly after lubricant infusion. Thus, the values of contact angles measured mainly were the characteristic of the lubricants used in SLIPS, not the fibres as they have been covered with the lubricant as well. Moreover, the air pockets on the surface have critical importance on its wettability in Cassie-Baxter state. However, the air pockets would be significantly reduced with the lubricants after the lubricant infusion. Therefore, the effect of both air pockets and the roughness of electrospun

PVDF-co-HFP were minimized (Figure 5.7). This has resulted in a dramatic decrease in contact angles of SLIPS compared to nanofibre membrane, which consisted of both air pockets and high roughness values. However, it is also worth noting that the contact angles of SLIPS were higher than >90°, which meant they were still in the hydrophobic region. When paraffin and silicone oils were used as the lubricants, both SLIPS revealed similar contact angles of about 98°. However, PcTFE-based SLIPS displayed much higher water contact angles around 108°, which were attributed to the low surface energy of PcTFE thanks to the high fluorine content of its chemical structure.

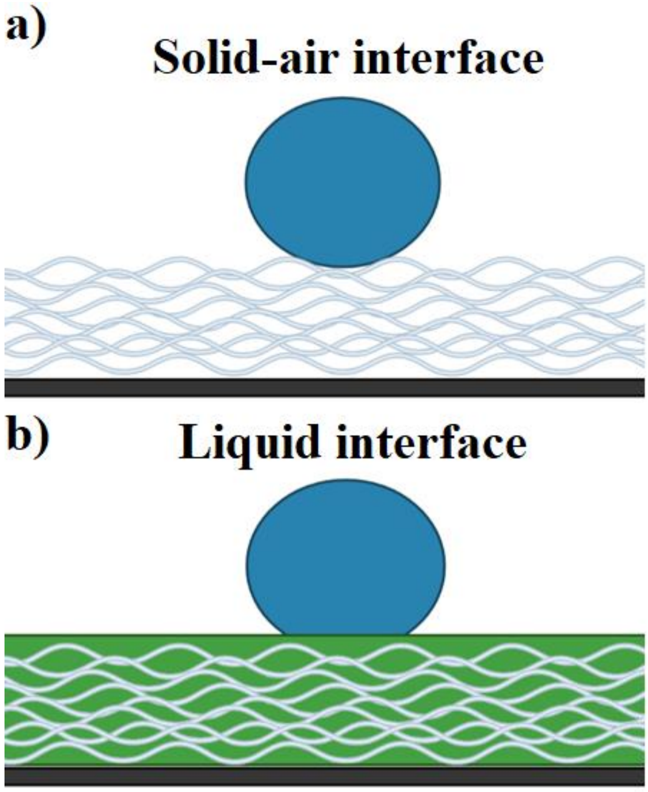

Figure 5.7 *Water-substrate interfaces without oil infusion (a: solid-air interface) and after oil infusion (b: liquid interface).*

Although lower static contact angles were achieved using all SLIPS compared to PVDF-co-HFP nanofibre membrane, much lower contact angle hysteresis values were also achieved. Results confirmed that all SLIPS had much better droplet mobility on their surface than as-produced nanofibre membranes despite the lower contact angle and higher droplet/surface interface. These results were consistent with the literature which investigated the droplet mobility on the surface of SLIPS [217]. Another important point was the stability of the contact angle hystereses against the change in volume of the droplet on SLIPS. However, the droplet volume had a critical effect on the CAH values of the PVDF-co-HFP in contrast to SLIPS. PcTFE-based SLIPS displayed the lowest contact angle hysteresis among all the samples fabricated with 5.5° for the 3.75 µL droplet size.

5.4 Ice Adhesion Strengths and Droplet Icing Times of Samples

The results of the ice adhesion strength test are shown in Figure 5.8. An aluminium plate, a commonly used material to investigate the icephobic properties of different coatings, was used as the reference material for comparison.

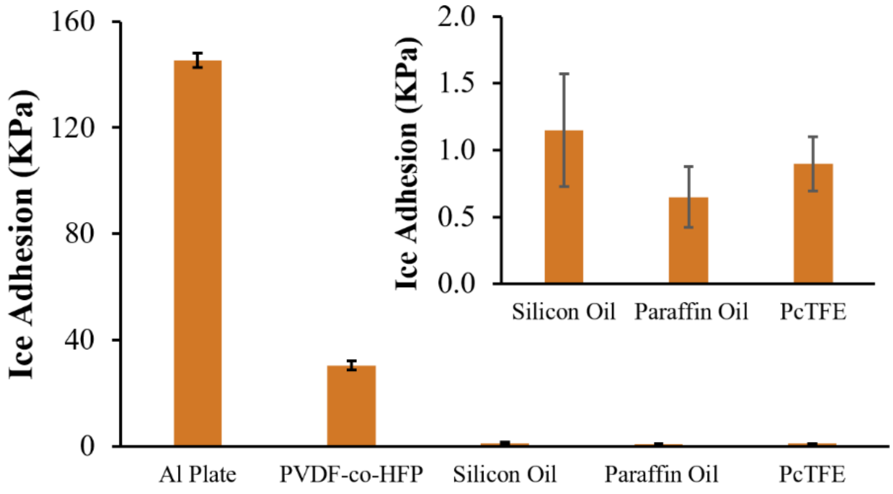

Figure 5.8 *Ice adhesion strengths of samples (Inset: ice adhesion test result of SLIPS with silicone oil, paraffin oil, and PcTFE, respectively).*

The PVDF-co-HFP nanofibre membrane exhibited a lower ice adhesion strength with 40 kPa than the aluminium plate. Even lower ice adhesion strength values were achieved with the infusion of the lubricant. Paraffin oil-based SLIPS revealed the lowest ice adhesion strength with about 0.65 kPa, while the other SLIPS prepared had around 1 kPa, lower than most of the studies published [145]. Three critical points would associate the low ice adhesion strength achieved: 1) The oil-water interface immiscibility prohibited anchoring the ice inside the SLIPS; 2) The ultra-smooth surface of SLIPS provided a slippery structure for the ice accumulated; and 3) Thanks to the low surface tension of the SLIPS offered, the water-lubricant interface was prevented from forming strong adhesion. Moreover, all the SLIPS displayed a much lower ice adhesion strength compared to superhydrophobic surfaces, which are considered promising for icephobic applications [9].

A summary of some up-front studies reported in the literature is given in Table 5.1. As seen, many approaches improved to achieve lower ice adhesion strength. However, only a relatively low number of works focused on the fabrication of the polymer substrate-based SLIPS. As reported elsewhere [218], most of the polymers have unique oil affinity which makes them promising to fabricate SLIPS structure. The interaction between oil and polymer can provide better durability, as well as an easier fabrication process. As the electrospun nanofibre membranes fabricated in this study had significantly high porosity, they were good storage for the oil, and more, electrospun nanofibre-based SLIPS exhibited less than 1 kPa of ice adhesion strength, one of the lowest ice adhesion values reported, which was promising compared to the literature. The other benefit of using the electrospinning technique is its unique advantages such as the scalability, easy processability and tunable porosity of the membranes produced. As seen from Table 5.1, usually expensive, high technology required systems are considered to fabricate porous parts of the SLIPS. However, in our study, a homemade electrospinning setup with easy to find chemicals and polymers was enough to prepare porous electrospun nanofibre membranes for SLIPS applications.

Table 5.1 *A brief summary of up-front studies reported on icephobic SLIPS.*

Author(s)	**Methods and key findings**	**Icephobicity achieved**	**Ref.**
Vogel *et al.*	Colloidal templating was used to fabricate nanoporous surfaces, Krytox 100 was infused to obtain SLIPS with closed-cell architecture.	10 ± 7 kPa, at -40 °C	[219]
Kim *et al.*	Textured polypyrrole coatings were carried out on aluminium surface using electrodeposition technique, perfluoroalkylether was used as the lubricant.	15.6 ± 3 kPa, at -10 °C	[220]
Irajizad *et al.*	Magnetic slippery surfaces were fabricated on aluminium surfaces using iron oxide nanoparticles and lubricant mixture, self-healing icephobicity was achieved.	2 Pa, at -10 °C	[221]
Zhang *et al.*	perfluoropolyether based double-layered SLIPSs were fabricated on magnesium substrate, corrosion-resistant coating with delay in icing and low ice adhesion was achieved.	40 ± 3 MPa, at -10 °C	[222]
Tao *et al.*	Polysiloxane and POSS based SLIPS were fabricated using hydrosilylation of three different siloxanes, durable icephobicity was achieved.	3.8 kPa, at -10 °C	[223]
Coady *et al.*	Porous Al oxide-silicon oil-based SLIPS were fabricated, durable icephobicity achieved by the addition of UV-cured siloxane resins.	Less than 10 kPa, at -10 °C	[224]
Wang *et al.*	SiO_2-ultrahigh molecular weight polyethylene dispersion with kerosene oil was used to fabricate icephobic SLIPS coatings.	Not given.	[225]
Liu *et al.*	Transparent, and omniphobic SLIPS were fabricated by infusion of fluorinated oil in PTFE, multifunctional properties with icephobicity and ice delaying were achieved.	Not given.	[226]

Araz *et al.*	Highly flexible LbL technology used to design SiO_2 surfaces with high roughness levels of, fluorinated oil was used to achieve SLIPS structure.	Less than 5 kPa, at -10 °C	[227]
Liu *et al.*	Textured anodic aluminium oxide was used to fabricate SLIPS with silicon oil as the lubricant. The high viscosity of lubricant was found to be promising for icephobic applications.	2.7 kPa, at -10 °C	[228]
Cui *et al.*	A low-cost rod-coating method was used to fabricate SLIPS, silicone oil was used as the lubricant.	Less than 55 kPa, at -10 °C	[229]
Ludmila *et al.*	Superhydrophobic coatings-based SLIPS were fabricated using Kyrox as the lubricant, ice adhesion results of superhydrophobic coating and SLIPS prepared compared and SLIPS found to be promising for icephobic applications.	Less than 20 kPa, at -10 °C	[230]

Besides the advantages of electrospun nanofibre membranes, some issues need to be addressed, such as the low mechanical properties compared to metal-based porous materials. The weaker mechanical properties may decrease the application areas of electrospun nanofibre-based SLIPS. However, this issue can be resolved using different approaches such as post-treatments, the addition of nanofillers and by using a combination of different polymers together.

Moreover, it is only possible to use soluble polymers in electrospinning, which is another issue in applications of electrospun nanofibre-based SLIPS. Relatively cheaper polymers such as polyethylene and polypropylene, and some engineering polymers (polyimides, PTFE, etc.) are not suitable for the electrospinning process and so, it is not possible to prepare electrospun nanofibre membranes using these polymers in electrospinning.

The last serious issue of icephobic applications of SLIPS, which is already reported in the literature, is the stability of the lubricant in the porous structure. Although the developed electrospun nanofibre membrane has an advantage of good affinity between oil and electrospun nanofibre membrane compared to literature, this would help slow the evaporation of lubricant, but not enough to stop evaporation or leaking of lubricant from the designed SLIPS. In this case, an environment-friendly lubricant should be chosen, or the durability of the lubricant needs to be improved. More works on the environmental effect of lubricant evaporated needs to be investigated in depth.

The droplet icing times test results are shown in Figure 5.9, with icing images of the samples during the test. The results prove that the SLIPS structures designed had exceptional anti-icing properties compared to the aluminium plate. Moreover, the best result was revealed by the PVDF-co-HFP nanofibre membrane itself, which consists of 70% of porosity, with approximately 40 seconds of droplet icing time. There is only a limited number of studies reported in the literature on anti-icing applications of porous structures, which aim to delay or prevent ice formation. Shen *et al.* [231] investigated the role of nanostructures on icing delay times and found that thanks to air-pillows trapped in the details of nanostructure has significant importance on anti-icing ability. They achieved around 170 s of icing time with the prepared nanostructured surface at -10 °C. Similarly, Li *et al.* [232] prepared different microstructured surfaces for icing delay applications and they obtained around 406 to 600 s of icing delay at -2.2 °C. Tao *et al.* [233] studied the ice delaying performance of Ti_6Al_4V substrate and its hierarchically textured forms. They reported that while Ti_6Al_4V exhibited around 11 s of ice delaying, using proper texture, it was possible to achieve higher than 700 s at -10 °C.

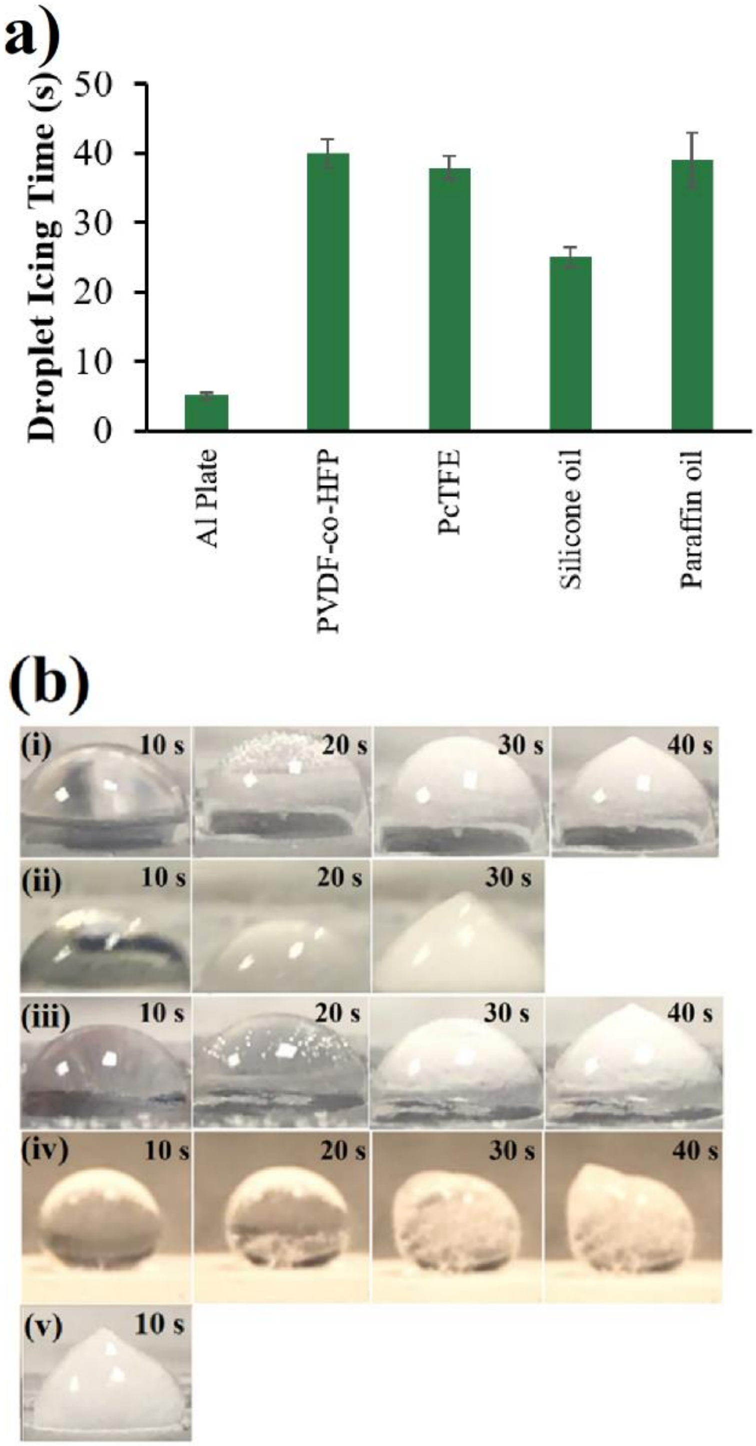

Figure 5.9 *(a) Droplet icing times of samples, the images during the icing from the samples of SLIPS, and (b) Images during the icing time measurements for each sample ((i) paraffin oil, (ii) silicon oil, (iii) PcTFE, (iv) PVDF-co-HFP nanofibre membrane and (v) Al plate).*

Compared to the literature, we have achieved only a limited capability of icing delay of a maximum of 40 s. However, it should be noted that the presented results were focused on anti-icing applications of the materials prepared. In our study, our ultimate aim was to achieve low ice adhesion strength, rather than longer icing times, and we have achieved one of the lowest ice adhesion strengths in the literature. Although the anti-icing and de-icing properties are related to icephobicity, they have different mechanisms of effect, it is not possible to achieve both properties considering only one mechanism. The increasing icing times were associated with the heat transfer capability of the structures designed. The thermal insulating effect of the air inside the pores prevented water droplets from freezing. The PcTFE and paraffin oil-based SLIPS displayed similar droplet icing times as a result of their low thermal conductivities of 0.065 and 0.12 W/mK respectively.

However, SLIPS with silicone oil showed a much lower icing time because of its much higher heat conduction ability. The thermal conductivities of PcTFE, liquid paraffin, and silicone oil are 0.065, 0.12, and 0.6 W/mK, respectively [218]. The water contact angle would also affect the droplet icing time. A lower contact angle of the droplet means a larger contact area, which provides a higher heat transfer rate. The heat resistance between the tested surface and the droplet would be reduced, causing a decrease in icing time.

5.5 Investigation of Optical Properties of the Samples and the Theoretical Explanations of Transparency Achieved

Optical transmittances of the samples are shown in Figure 5.10. PVDF-co-HFP electrospun membrane did not show significant transmittance in the visible light spectrum, between 300 and 900 nm wavelengths. The relationship between deposition time of electrospinning and transparency of PVDF-co-HFP has been discussed before [234]. It was found that when the deposition time, or the thickness of the membrane, increased, the transmittance of the electrospun membrane is decreased.

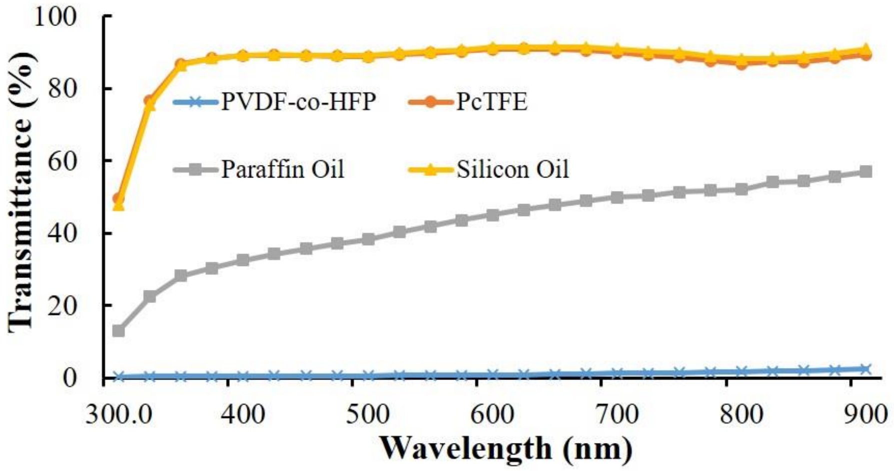

Figure 5.10 *Optical transmittances of samples (UV-Vis spectrums of PcTFE and silicon oil overlapped).*

It is well known that transparent materials are made up of components with uniform refractive indices, and for multi-component structures, a mismatch of the refractive indices results in opacity [235, 236]. For a two-phase system, the reduction of light intensity due to scattering is given by the following formula, Equation 5.1.

$$T = \exp\left\{-\left[\frac{3\Phi r^3}{4\lambda^4}\left(\frac{n_p}{n_m} - 1\right)\right] s\right\} \qquad \textit{(Eq. 5.2)}$$

Where T is transmittance, ϕ is the volume fraction of particles, r is particle radius, λ is the wavelength of light, s is film thickness, n_p is refractive index values of the particles, and n_m is the refractive index value of the matrix phase.

The difference between n_p and n_m is defined as the RI mismatch (Δn); decreasing Δn decreases scattering loss and increases transmittance. In other words, the possibility of light passing through a medium or not depends on the homogeneity of the refractive index of the final structure [237]. Infusion of the lubricant contributed drastically to the excellent transparency of the electrospun membrane, depending on the refractive index of lubricant used (Figure 5.11).

When silicone oil and PcTFE, which have quite similar refractive indices as PVDF-co-HFP, were used as lubricants, they both provided transmittance higher than 90% because of the uniform refractive index of the entire structure. The lowest transmittance obtained was lower than 40% when paraffin oil was used as a lubricant, which has a large discrepancy compared to the refractive index of PVDF-co-HFP. These results are promising because the produced SLIPS may be used for energy harvesting systems where the transparency of the top surface would directly influence the efficiency of the solar panels [238].

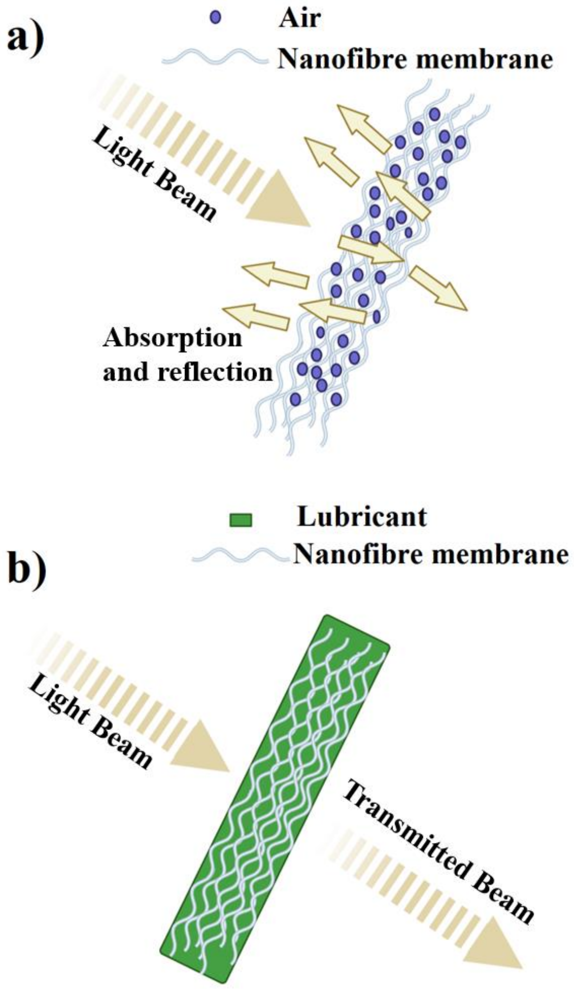

Figure 5.11 *The effect of refractive index (a) mismatch and (b) matching on two-phase composite systems*

5.6 The Theory of Icephobic Behaviour of SLIPS

As explained before, the mobility of a droplet on the surface is a critical characteristic that plays a major role in the ice adhesion strength of the surface. SLIPS provides good droplet mobility upon the thin lubricant layer, which makes it promising for icephobic applications. However, some important conditions need to be met for the SLIPS to exhibit good droplet mobility on the surface. When a water droplet is placed on top of SLIPS, three distinct wetting regimes can take place. The first one is called the impaled regime, where the infused lubricant is replaced by the water (Figure 5.12a) and in this scenario, there is a clear, direct contact between the water droplet and porous structure. Because of that, the water droplet can not slide freely but be pinned on the surface of SLIPS.

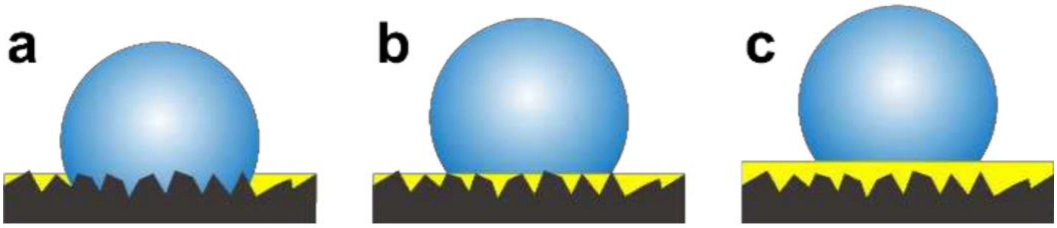

Figure 5.12 *Schematic representation of (a) impaled, (b) emerged and (c) encapsulated regimes on PVDF-co-HFP electrospun nanofibre membranes/Lubricant systems (black=substrate, yellow=lubricant and blue=water droplet) [239].*

In the second scenario, the porous structure is impregnated with infused lubricant. However, the top edges of the solid structure emerge and make direct contact with water droplets called impregnated/emerged regime. (Figure 5.12b). In the third and last scenario, the porous structure is completely encapsulated by the lubricant which provides no direct contact between the water droplet and porous structure, and the water droplet sits entirely on a thin film of lubricating liquid (Figure 5.12c). To provide high water droplet mobility and low ice adhesion strength, the encapsulated regime is required to be achieved. The thin film of lubricating liquid between the water droplet and porous material enables the water droplets to slide freely on the surface. For the impaled and emerged regimes, water droplets are pinned onto the SLIPS and provide no mobility for the water droplets, increasing the ice adhesion strength.

According to Varanisi *et al.* [240], the lubricant spreading coefficient value on solid underwater is important for achieving the encapsulated regime, and it must be higher than 0 [240]. This value can be calculated from the following formula:

$$S = \sigma_p - (\sigma_{\mathrm{l}} + \sigma_{\mathrm{pl}}) \qquad \textit{(Eq. 5.2)}$$

Where *S* is spreading coefficient, *p* is the surface tension of porous structure, *l* is the surface tension of lubricant, and *pl* is interfacial tension of porous structure and lubricant.

As seen from the formula, when the surface tension of lubricant becomes smaller, the spreading coefficient *S* becomes positive. That was why the low surface tension lubricants were chosen for this study. It was easily possible for the PVDF-co-HFP electrospun nanofibre membrane/low surface tension lubricant systems to achieve the positive value of S and encapsulated regime. The sliding angle results also supported that the encapsulated regime has been achieved as the droplet is not pinned on the surface. It should also be noted that the spreading factor is not dependent on the surface texture but only depends on the chemical properties of both lubricant and porous structure.

The substrate and lubricant characteristics are key factors to consider when fabricating slippery surfaces having an anti-icing property. For the lubricants used in SLIPS, parameters such as viscosity, chemical structures, and organic liquid affect anti-icing properties. The lubricants used in liquid-infused systems are mostly organic fluids, such as fluorinated components or silicon oils. Some characteristics, including low surface energy and fluidity, apply to both mentioned lubricants. Low-surface-energy liquids reduce intermolecular interactions, such as hydrogen-bonding, between ice and solid surfaces and thereby affect ice adhesion. Smooth lubricants can also cover the surface completely and, therefore, decrease the possibility of anchoring between ice and the textured substrate, which commonly occurs for superhydrophobic surfaces. The icing mechanism on a SLIPS is shown in Figure 5.13. As a result of the oil layer between ice and water droplet, ice cannot anchor inside the pores and because of the very low adhesion between oil and the ice, low ice adhesion strength values can be easily achieved by the SLIPS structure. Additionally, the three lubricants used had extremely low vapour pressures and therefore, it limited the concern of evaporation and loss of lubricant.

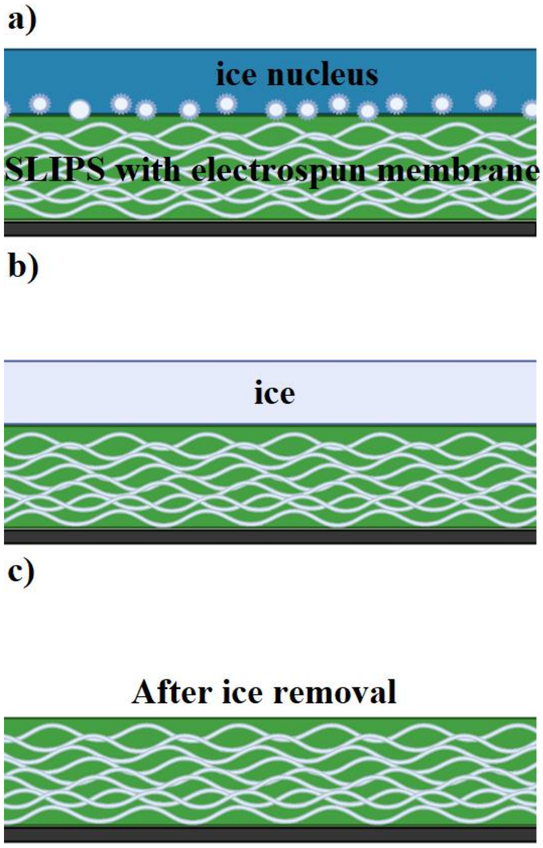

***Figure 5.13** The icing mechanism on electrospun SLIPS (a) ice nucleation, (b) lubricant-ice interface and (c) the effect of ice removal.*

5.7 Summary

In this study, we present a cost-effective and scalable electrospinning technique to produce freestanding nanofibrous polymeric surfaces to fabricate transparent icephobic SLIPS. The electrospun membrane was produced using the outcomes of the Taguchi method from Chapter 4, to obtain a smooth fibrous structure with an average fibre diameter of 330 ± 63 nm. Three liquids (PcTFE, silicone oil, and paraffin liquid) were used as lubricants with low surface energy and low vapour pressure for the SLIPS. The topographical images of the samples showed that infusion of the lubricant provided a smooth surface, which is one of the critical parameters for icephobic application. The contact angle values also decreased after lubricant infusion, compared to the as-prepared PVDF-co-HFP electrospun membrane, due predominantly to the change in roughness and the nature of the lubricants used. We also found that the mobility of the droplets on the SLIPS was enhanced dramatically, compared to the as-produced PVDF-co-HFP electrospun membrane, due to the slippery behaviour of the lubricants. Because of the similarity in the refractive indices of lubricants and polymer, SLIPS with silicone oil and PcTFE showed transmittance as high as 90% in the visible light spectrum, between 300 and 900 nm wavelength. All SLIPS exhibited low ice adhesion strength down to 1 kPa, which was significantly lower than the PVDF-co-HFP electrospun membrane itself, and icing delay times obtained were from 5 to 41 seconds which indicates a good anti-acing ability at -10 °C. Considering the observed properties, icephobicity, and transparency, the SLIPS prepared was promising for possible applications on solar panels and window glasses etc.

CHAPTER 6

Recycled PET/Magnetite Nanocomposite Electrospun Membranes for Outdoor Electromagnetic Shielding Applications

6.1 Introduction

Among the wide range of superhydrophobic and icephobic surfaces applications, outdoor electromagnetic equipment has received increasing attention. It is crucial to protect such equipment from the excess weight of ice and corrosion. However, an additional function, electromagnetic shielding efficiency, is expected from the surfaces designed from electrospun membranes for this application. This chapter discusses our design and production of multifunctional electrospun membranes, offering electromagnetic shielding efficiency, icephobicity and superhydrophobicity for outdoor electromagnetic shielding applications. As distinct from chapters 4 and 5, this work aims to provide an additional function, i.e., electromagnetic shielding efficiency, alongside superhydrophobicity and icephobicity. Additionally, to broaden the possibilities of using recycled materials, recycled PET bottles were used as the starting material for this work, instead of virgin polymers. The use of recycled plastic materials could demonstrate alternative benefits that may help to boost recycling incentives for PET, working towards recyclable economic approaches.

Although there are several studies published investigating new materials for outdoor EMI shielding applications [241-243], those authors did not conduct any studies exploring materials developed with superhydrophobicity, coupled with icephobicity properties; this could be a critical feature applied to outdoor electronic equipment, especially for those based in cold-weather regions [218]. Some works considering the combination of superhydrophobicity and EMI shielding efficiency in a single material system are summarized as follows:

Zhenge *et al.* prepared multifunctional PVDF/carbon (graphene and multi-walled carbon nanotube) porous composite materials and reported achieving electromagnetic shielding efficiency of 28.5 dB at a frequency of 8 – 12 GHz. They also evaluated these materials' superhydrophobic properties, which produced water contact angles (WCA) of 155° [241]. Megaridis *et al.* prepared PTFE/carbon nanofibre nanocomposites and reported EMI shielding efficiency of 25 dB in the range 8.2 – 12.4 GHz, along with a WCA of up to 158° [242]. Ma *et al.* produced cotton fabrics treated with Nafion/multi-walled carbon nanotube dispersions, which achieved 9 dB EMI shielding efficiency along with a WCA of 154° [244]. Lee *et al.*, who produced surface-modified carbon nanotube films, achieved a contact angle of 153°, along with sheet resistance of 4.1×10^4 Ω/square [245]; they suggested that these materials could also potentially be applied to electromagnetic shielding applications. Zhai *et al.* prepared nanocomposite coatings using carbon nanotubes with conjugated block co-polymer (rrP3HT-b-PS), which achieved an electrical conductivity of 30 – 100 S cm^{-1}, along with a water contact angle of above 158° [246]. Although the above studies reported impressive EMI shielding and contact angle measurements, the materials explored are relatively expensive compared to a naturally abundant material, such as magnetite, and have yet to achieve suitably efficient scale-up production.

The randomly oriented fibrous structure and high amount of air pockets on the surface due to the high roughness exhibited by electrospun nanofibre membranes make them a strong candidate for icephobic applications considering the Cassie-Baxter icing state. Moreover, polymer-based EMI shielding composites have become more and more popular and replaced traditional EMI shielding materials, which are metal-based, due to their unique advantages of easy processability, their lightweight nature and corrosion resistance [247]. It was also reported that thin nanofibrous membranes are promising for EMI shielding applications thanks to their porous structure which led to an increase in multi-reflection loss [238]. Additionally, the possibility to fabricate nanocomposite fibre membranes using electrospinning allows imparting specific properties such as high dielectric constant which is an important parameter for EMI shielding [248, 249].

In this study, recycled PET, obtained from waste bottles, was investigated as the matrix phase for developing electrospun membranes. The multifunctional nanofibre membranes were prepared via a two-step fabrication process. In the first step, magnetite/r-PET nanocomposite nanofibre membranes were produced, and as the second step, surface functionalization with fluorinated silane functionalized SiO_2 (FSFS) was carried out. We then measured the superhydrophobic and icephobic properties of the as-prepared membranes, using the static and dynamic contact angle measurement system and centrifuge method. Furthermore, the effect of magnetite content on electromagnetic shielding efficiency was investigated using the coaxial transmission line method.

6.2 Surface imaging and topography measurement

SEM images of r-PET and r-PET/magnetite nanocomposite membranes are shown in Figure 6.1.

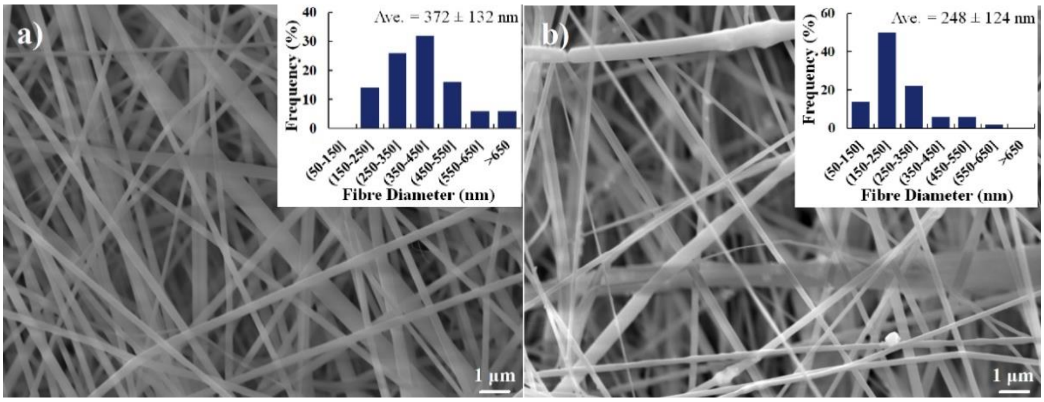

Figure 6. 1 *SEM images of the (a) pure r-PET and (b) r-PET/magnetite nanocomposite fibre membrane (20% wt. magnetite) (inset: fibre diameter distributions of samples).*

Although there was a significant colour change from white (r-PET) to black (r-PET/magnetite nanocomposites) with the addition of 20 wt.% of magnetite inside the polymer, as a result of the solution mixing method, magnetite nanoparticles mainly were enclosed within the fibres. Even though probe sonication was used to agitate the magnetite nanoparticles thoroughly, some agglomerated particles were observed, most likely caused by the high surface energy and high concentration of magnetite nano particles as seen inside the circles, in Figure 6.2. However, the effect of these agglomerated particles on the surface properties was limited, as they did not cause an elemental heterogeneity but only a restricted morphological change. When the polymer and nanoparticles are mixed homogeneously, theoretically, nanoparticles would be enclosed inside the fibre or covered with the polymer layer after solvent evaporation (Figure 6.2), which provides an elementally homogenous electrospun surface in both cases.

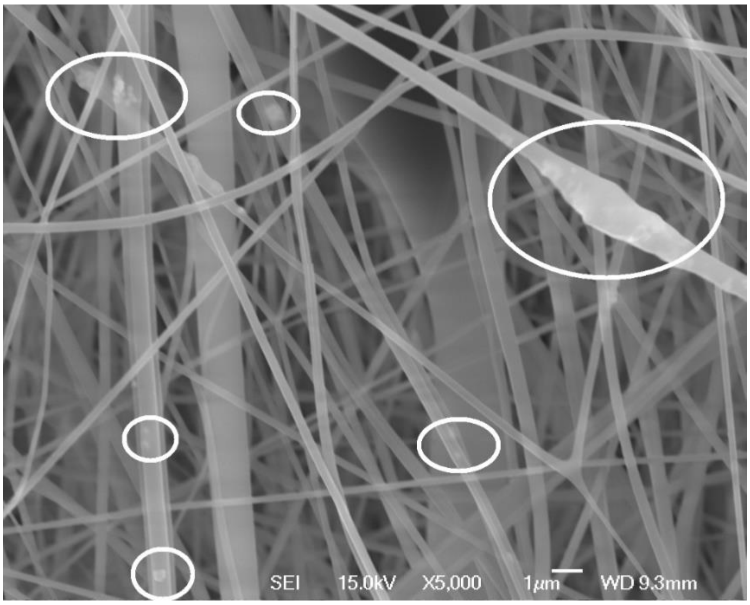

Figure 6. 2 *Agglomerated magnetite nanoparticles and their effect on the morphology of the electrospun membrane (circles: agglomerated magnetite nano particles).*

The average fibre diameter of the r-PET electrospun membrane was calculated as 372 ± 132 nm using the imageJ from 50 measurements, and the majority of the fibres were between 150 and 550 nm in diameter. However, the addition of magnetite to the polymer revealed a dramatic change in the distribution of fibre diameters. Although the average fibre diameter of magnetite/r-PET was within the error (248 ± 124 nm), the majority of the fibres had a diameter between 50 and 350 nm, which makes clear that magnetite's effect on the fibre diameter distribution. This change was attributed to the whipping instability related to surface tension and the viscosity of the polymer solution.

The whipping instability of the polymer jet changed due to alteration of the surface tension and surface charge repulsion. The viscosity of the solution also altered due to the incorporation of magnetite nanoparticles which triggered the electrified liquid jet to split into smaller branches during the electrospinning process [250].

After dip coating with FSFS carried out, both the surface chemistry and morphology had been changed significantly. The SEM image of the FSFS coated r-PET/magnetite nanofibre membrane is given in Figure 6.3. As seen, the FSFS nanoparticles were accumulated on the surface of the fibres. This structure can be promising to achieve superhydrophobicity by not only the change on the surface chemistry but also relatively hierarchical structure. Electrospun nanofibre membrane already has a rough surface because of the randomly oriented fibres. The addition of nanosized FSFS on the surface provided an additional level of roughness.

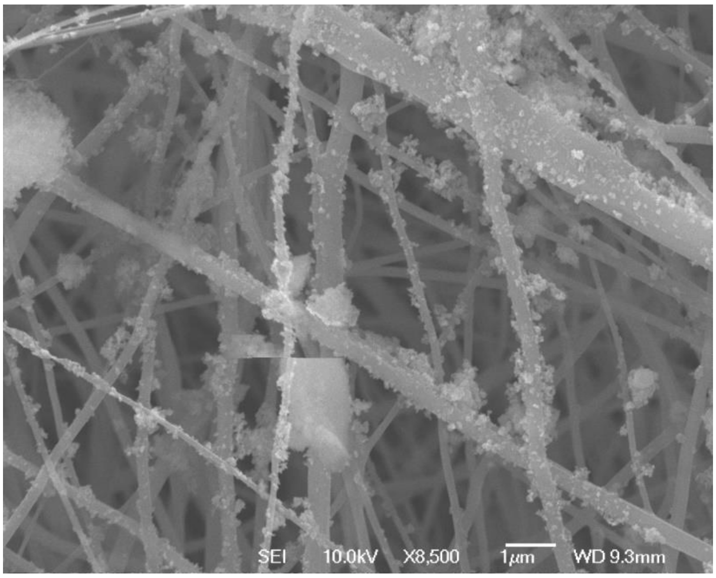

Figure 6. 3 *The SEM image of FSFS coated r-PET/magnetite nanofibre membrane.*

The surface appearance and topographical image comparison of the r-PET nanofibre membrane before and after the FSFS treatment are shown in Figure 6.4. As the method used for topographical images was microscale, it did not show a significant difference after the FSFS coating, which was a nanoscale change. To understand this difference, the roughness of the fibres, instead of the whole electrospun membrane could be measured. However, it is still clear that the membranes produced had a good roughness thanks to the method used, electrospinning. The randomly distributed fibres, different diameters, agglomerated magnetite particles, and FSFS particle presence had majorly contributed to the roughness of the electrospun membranes.

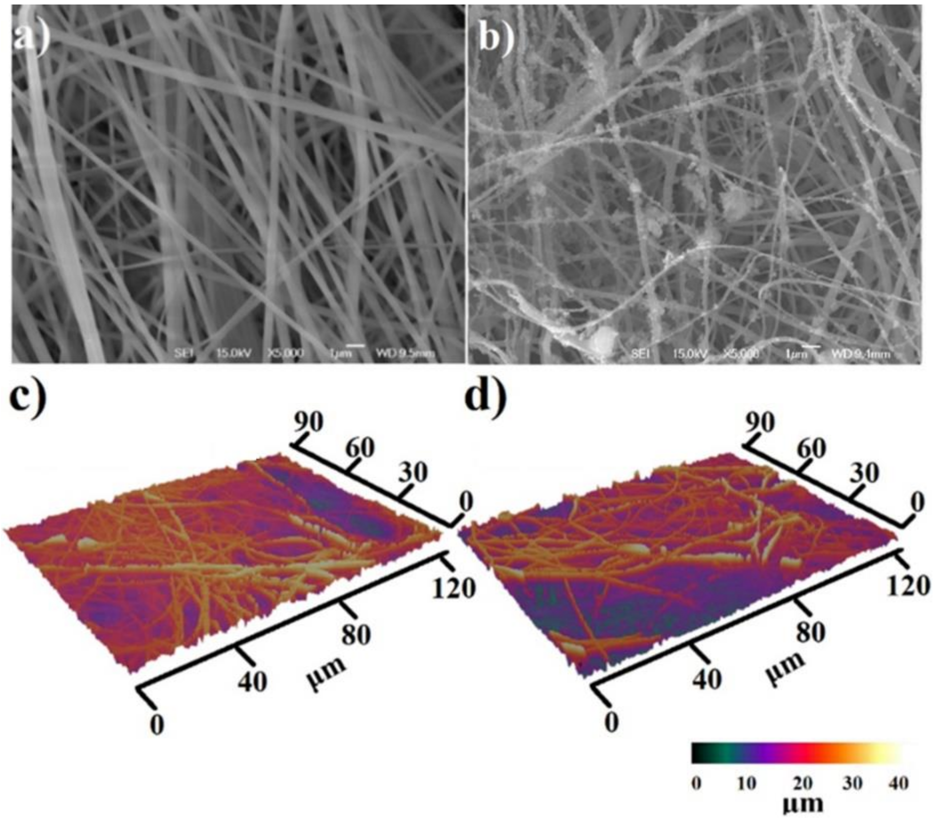

Figure 6. 4 *SEM and 3D topographical images of (a and c) r-PET/magnetite nanocomposite fibre membrane and (b and d) FSFS treated r-PET/magnetite nanocomposite fibre membrane.*

6.3 Analysis of Chemical Compositions

The FT-IR spectra of SiO_2, PFTOES, and FSFS are shown in Figure 6.5 over a wavenumber range of 650-2000 cm^{-1}. The main peaks expected from SiO_2 were Si-O-Si and Si-O peaks in this range as there is no other chemical bonding in the structure of SiO_2 As expected Si-O-Si stretching, and Si-O bending bands were observed at around 1080 and 802 $cm^{-1,}$ respectively [251, 252]. On the spectrum of PFTOES, characteristic peaks of CF_2 and CF_3 were found between 1325 and 1100 cm^{-1} [253]. Even though the Si-O-Si band and the characteristic peaks of PFTOES occurred in the same region, which led to the overlapping of the peaks, the spectrum of FSFS reaffirmed that SiO_2 particles had been successfully modified.

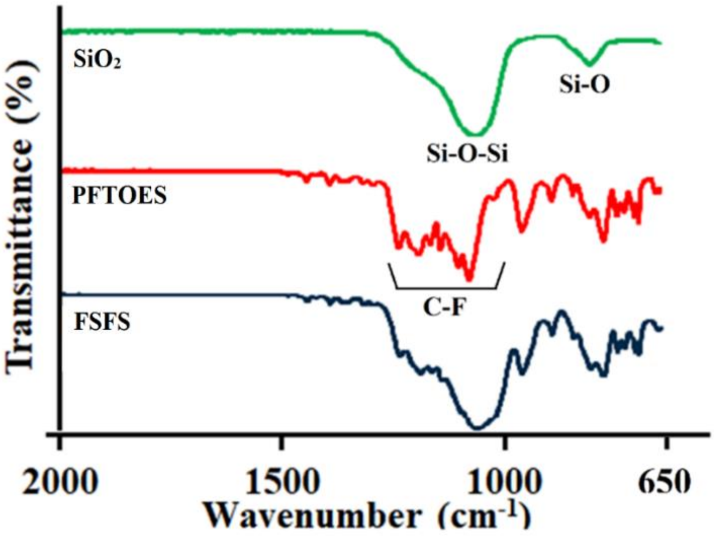

Figure 6. 5 *FT-IR spectra of SiO_2, PFTOES, and FSFS.*

The EDX mapping images of r-PET/magnetite and XPS spectrum of FSFS treated r-PET/magnetite are shown in Figure 6.6. The EDX mapping results revealed a homogenous distribution of iron on all the surfaces. As seen, the O content was significantly higher compared to the Fe content. The reason was that both r-PET and magnetite had oxygen content, and a higher level of O signal was observed. Moreover, the XPS spectrum confirmed the F and Si contents on the FSFS treated r-PET/magnetite electrospun sample's surface.

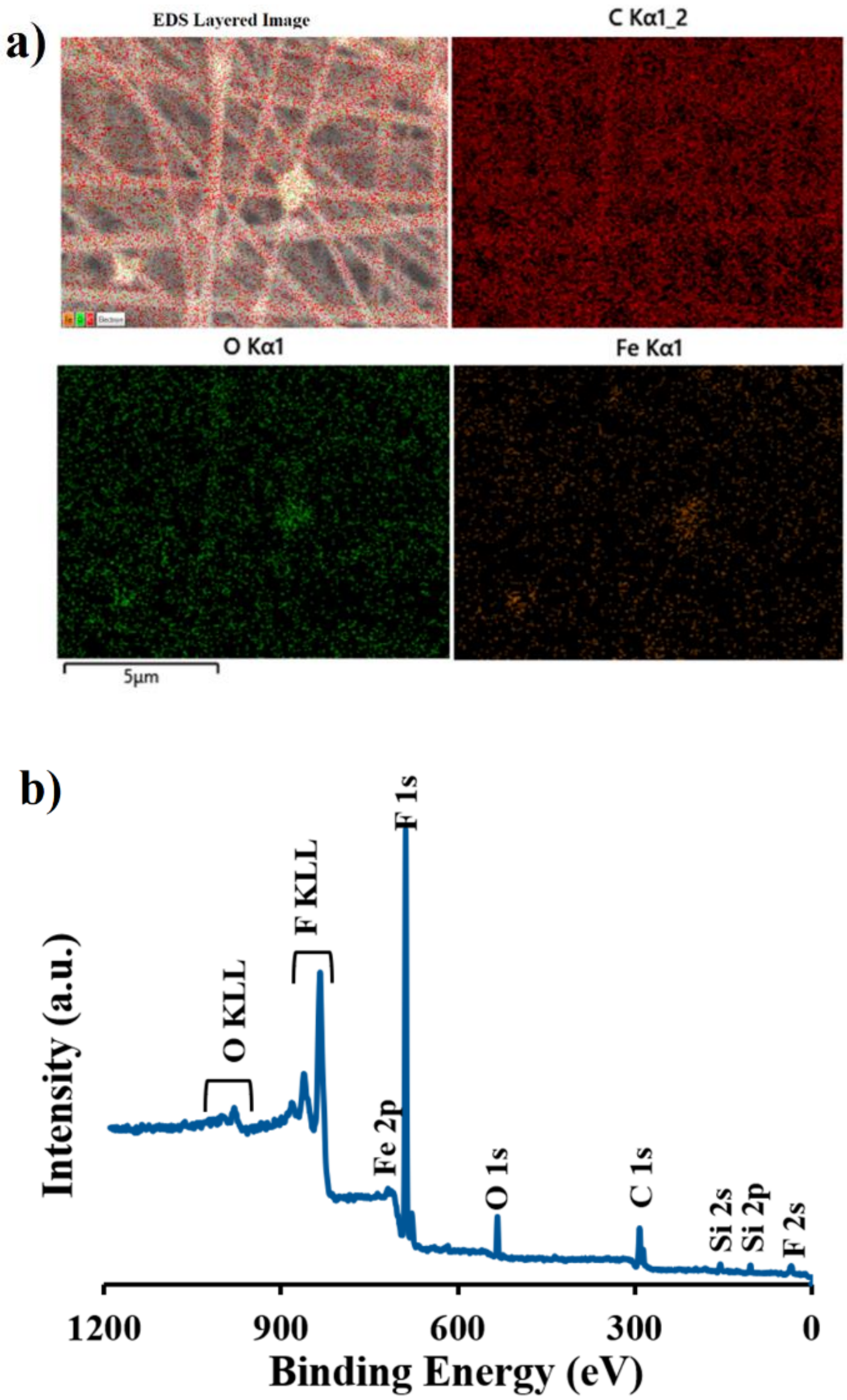

Figure 6. 6 *(a) EDX mapping image of r-PET/magnetite nanocomposite fibres and (b) XPS spectrum of FSFS treated r-PET/magnetite nanocomposite fibres.*

According to Figure 6.6b, Si peaks were found at 155 eV and 104 eV, the Si 2s and Si 2p, respectively. Moreover, the O1s signal was found at 533 eV. Because the sample with FSFS coating was not a thin film but had relatively heterogenous nano-granular surface roughness, the intensities of the peaks are disregarded. It is also noteworthy that according to the XPS results, the content of the Fe on the surface is significantly low. Considering that Fe was around 20 wt.%, this is clear proof that the magnetite particles are inside the fibres, or at least covered with polymer film during solution mixing. Otherwise, there would be a dominant peak of Fe on the spectrum of XPS.

6.4 Effect of FSFS treatment on surface wettability

Static, advancing and receding contact angle (CA) values of the samples before and after FSFS coating are highlighted with their CA hysteresis in Table 6.1. r-PET and magnetite/r-Pet nanocomposite electrospun membrane exhibited similar wetting behaviour with a water contact angle of 137.8 and 137.6°, respectively. The addition of magnetite only had a minimal effect on the wetting properties of the samples. It was because the majority of the magnetite nanoparticles were inside the fibres, not on the surface. The limited amount of magnetite on the surface was covered by the r-PET as proofed by XPS spectrum and SEM images. As such, the chemical composition of the surface of the r-PET/magnetite sample remained similar to the r-PET. Also, although a difference in fibre diameter distributions between r-PET and r-PET/magnetite nanofibre membranes was obtained, it was insufficient for affecting surface wettability. The samples without FSFS treatment showed high static contact angle values (higher than 133°), and their contact angle is considered as hydrophobic surface. However, the contact angle hysteresis of this sample was higher than 46°, which indicated that the droplet's mobility was significantly limited due to the high surface tension of PET (44.6 mJ/m [254]). Therefore, the sliding angle could not be measured for samples without FSFS treatment, as the droplets were pinned to the surface regardless of the tilt angle.

Table 6. 1 *Static, advancing, and receding CA values of r-PET, magnetite/r-PET, and FSFS treated magnetite/r-PET samples with their CA hysteresis and sliding angles.*

Sample	**Static CA (°)**	**Advancing CA (°)**	**Receding CA (°)**	**CA Hysteresis (°)**	**Sliding Angle (°)**
r-PET	137.8±2.6	136.3±1.2	82.6±3.2	55.6±3.0	>90°
20 wt.% mgt/r-PET	137.6±0.1	133.3±0.4	86.6±2.5	46.6±2.6	>90°
FSFS treated 20 wt.% mgt/r-PET	>160°	158.2±3.3	154.6±4.2	3.8±3.7	<1°

Surface chemistry and surface topography are the major parameters used in identifying the wettability behaviour of the materials. After the FSFS treatment, the sample displayed exceptional superhydrophobicity, most likely due to the dramatic change in surface chemistry and morphology. The static contact angle of the FSFS treated sample could not be measured because of the droplet's immediate 'rolling-off' from the surface. However, as the droplet stayed pinned to the needle in the dynamic contact angle measurements method, it was possible to measure advancing and receding contact angles used to calculate the CA hysteresis. The FSFS treatment process resulted in a significant decrease in the surface energy of the final structure compared to the r-PET electrospun membrane. Moreover, the FSFS coating on the fibres contributed to a hierarchical surface structure, which also played a vital role in surface wettability. The effect of hierarchical structure is described in Figure 6.7. Combining these changes drastically improved the surface hydrophobicity in terms of contact angle and contact angle hysteresis.

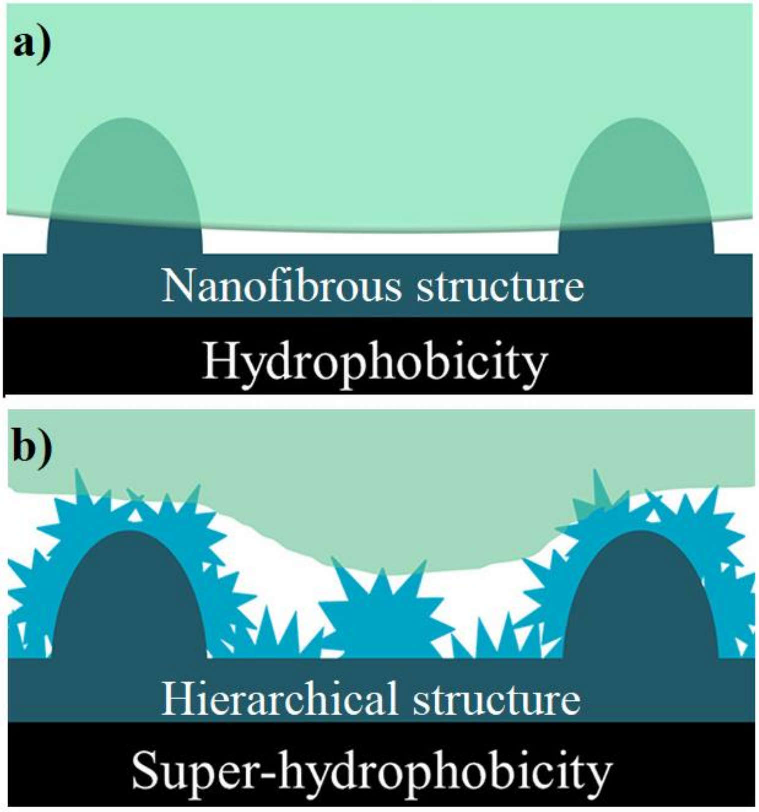

Figure 6. 7 *The effect of (a) roughness and (b) hierarchical structure of nanofibre membrane on surface wettability.*

The wetting state of Cassie-Baxter instead of Wenzel is generally required to achieve superhydrophobic properties. The FSFS treatment changed the wetting state of the sample from Wenzel to Cassie-Baxter state. It can be easily understood because, after FSFS treatment, the droplet did not penetrate between the fibres but sat on the air pockets known as the Cassie-Baxter state.

6.5 Ice Adhesion Strength and the Relevant Mechanisms of the Nanocomposite Membranes

To compare the ice adhesion strengths, an Al plate (used as a reference) and r-PET, FSFS treated r-PET, and FSFS treated r-PET/magnetite samples were all subjected to centrifuge testing. The lowest ice adhesion strength results were taken from the FSFS treated r-PET and FSFS treated r-PET/magnetite samples with 51 and 59 kPa, respectively. The r-PET sample without an FSFS treatment showed much higher ice adhesion strength with around 105 kPa. However, it was found that without the FSFS treatment, the r-PET was damaged during the ice adhesion strength test, while the ice was detaching from the surface (see inset Figure 6.8a). Basically, it was because the adhesion between ice and the electrospun membrane was significantly higher than the strength of the electrospun membrane.

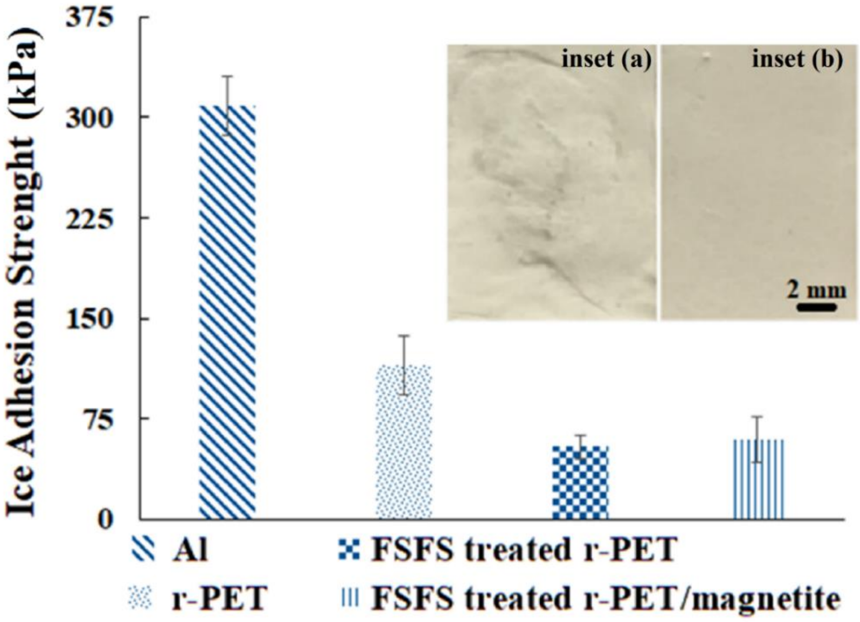

Figure 6. 8 *Ice adhesion strength values of the aluminium reference versus r-PET, FSFS treated r-PET and FSFS treated r-PET/magnetite electrospun membranes (Surface appearance after ice adhesion test for (inset: a) untreated and (inset: b) FSFS treated samples).*

There are two leading states when water droplets contact rough surfaces (i) Cassie-Baxter state and (ii) Wenzel State. In the Cassie-Baxter state, the droplet of water sits on top of the roughness structures and air pockets, while in the Wenzel State, the water droplet thoroughly wets the roughness structures [255]. The samples without FSFS treatment showed the Wenzel state when contacting water, which resulted in water penetration into the air gaps between the fibres. Moreover, whilst ice accretion occurred, it was anchoring inside the nanofiber membrane, within the space between the fibres, which could have caused high adhesion between ice and the nanofibre membrane due to potential mechanical interlocking at the ice-surface interface. These ice-filled nanofibre regions may have moved away from the surface with the detached ice glaze and caused the damaged structure (as depicted in the inset in Figure 6.8).

Additionally, the state of wetting has a critical role in the icing interface between ice and nanofibre membrane. The work of adhesion in Wenzel state ice can be explained with the following equation:

$$W_{sl}^{W} = r \cdot W_{sl}^{smooth} \qquad \textit{(Eq.6.1)}$$

Where W_{sl}^{W} is work of adhesion in Wenzel state, *r* is the ratio of actual surface area to the apparent one and W_{sl}^{smooth} is the work of adhesion for a smooth surface. Because *r* is larger than 1 according to the Wenzel state, the work of adhesion increases significantly. However, an opposite situation is taken place in Cassie-Baxter state, which can be summarized in the following equation:

$$W_{sl}^{CB} = r_f \cdot f \cdot \sigma_{lv}(1 + \cos\theta_{sl(r)}^{smooth}) = r_f \cdot f \cdot W_{sl}^{smooth} \qquad \textit{(Eq. 6.2)}$$

Where W_{sl}^{CB} is the work of adhesion in Cassie-Baxter state, f is the wetted area, and r_f is the roughness factor of wetted areas. As r_f is significantly lower in the Cassie-Baxter state than the smooth surface contact area, the work of adhesion would be decreased with it [256]. The schematic representation of the effect of the wetting state on the cross-sectional area of the ice-substrate interface is described in Figure 6.9.

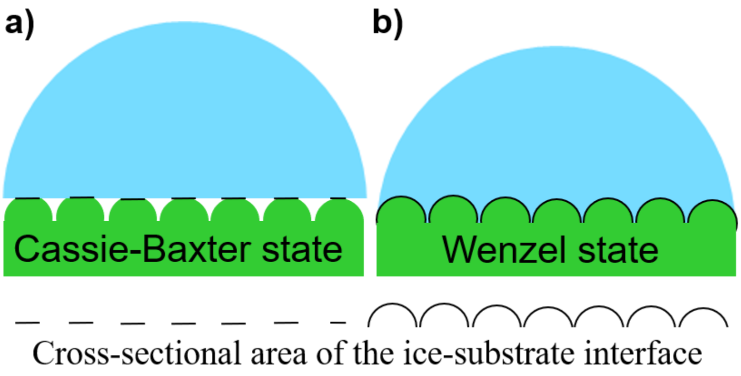

Figure 6. 9 *The effect of (a) Cassie-Baxter state and (b) Wenzel state on the interface between ice-nanofibre membrane.*

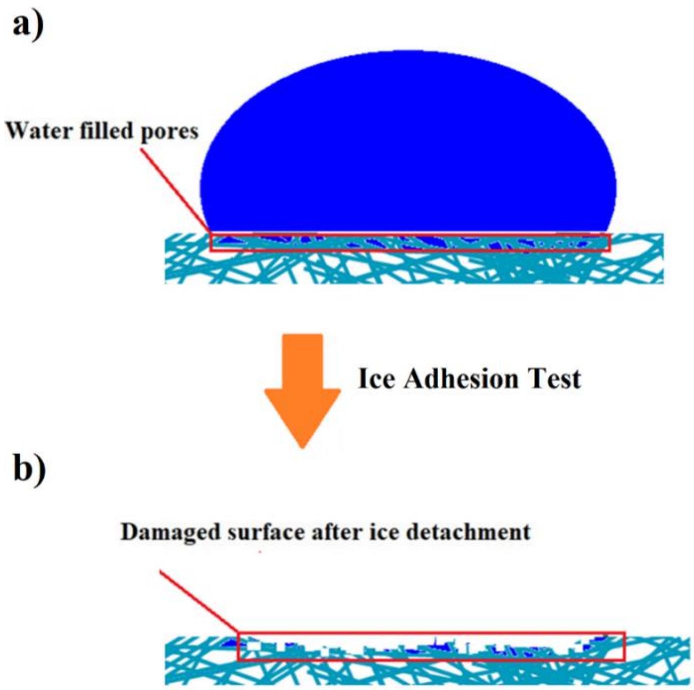

Figure 6. 10 *The effect of Wenzel State on the surface damage during the ice-adhesion test for untreated r-PET/magnetite nanofibre membranes, (a) before and (b)after ice adhesion test.*

It is also possible that the high surface tension and high contact angle hysteresis contributed to the high adhesion strength. About 105 kPa ice adhesion strength was obtained for the samples without FSFS treatment. However, due to the damage of the surfaces, the actual ice adhesion strength of the samples without FSFS treatment was expected to be higher.

After FSFS treatment, the samples achieved clean non-damaged surfaces, with a much lower ice adhesion strength of around 51 kPa. The reduction in ice adhesion strength was at least 60% and the main reason for the dramatic decrease in ice adhesion strength was probably due to the Wenzel to Cassie-Baxter transition. In Cassie-Baxter state, the water could not infuse into the gaps between the fibres but stayed in the air pockets due to the lower wettability. The ice adhesion strength is significantly reduced when this is combined with a much lower interface area between ice and electrospun membrane due to fibrous and porous structure.

As proved, among superhydrophobic surfaces, only Cassie-Baxter state-based superhydrophobic materials were found to be promising for icephobic applications [257]. Summary of some important literature on Cassie-Baxter icing state-based icephobic materials is given in Table 6.2.

Table 6.2 *Cassie-Baxter icing state-based icephobic material designs from the literature.*

Author (s)	**Production methods and key findings**	**Icephobicity achieved**	**Ref.**
Subramanyam *et al.*	Frost formation and ice adhesion on superhydrophobic surfaces fabricated were studied via direct microscale imaging. It was reported that “Cassie ice”-promoting textures are promising for icephobic applications.	15 times lower than the control sample (Wenzel ice)	[258]
Kulinich *et al.*	The effect of contact angle hysteresis on the ice adhesion strength of superhydrophobic surfaces was investigated. They found that the high contact angle hysteresis, which points to Wenzel State, provide a large ice-solid area upon icing and high ice adhesion strength.	65 kPa	[259]

Fu *et al.*	Superhydrophobic sol-gel coatings with different roughness and surface energy were prepared on a glass substrate and a stable Cassie ice state was achieved.	75 kPa	[260]
Gleason *et al.*	Fluoropolymer coated Si substrates exhibiting Cassie-Baxter state were fabricated to achieve low ice adhesion strength.	185 kPa, 6 times lower than bare Si	[261]
Kulinich *et al.*	Anti-icing properties of superhydrophobic nonwovens were investigated and fibrous structures were found to be promising to achieve the Cassie-Baxter state.	55 kPa	[262]
Choi *et al.*	superhydrophobic surfaces with different surface roughnesses and wettabilities were fabricated and their icephobic properties were studied to investigate the correlation of icephobicity with the different surface properties	Less than 20 N for a droplet volume of 120 µL	[263]
Zhong *et al.*	Triple-scale micro/nanostructured superhydrophobic surface fabricated via a combination of ultrafast laser ablation and chemical oxidation. The samples fabricated were exhibited good Cassie state stability.	Less than 2 kPa	[264]
Uzoma *et al.*	The spray coating process was used to fabricate superhydrophobic nanocomposite coatings exhibiting Cassie-Baxter icing state, using nanodiamonds and siloxane-acrylic resins.	44.56 kPa	[265]
Bonaccurso *et al.*	Silicone nanofilament based icephobic coating fabricated n on anodic metal oxide surfaces for aircraft applications.	13 kPa	[266]

As seen from the literature, 50 kPa of ice adhesion, which we have managed to achieve, is a good level of icephobicity for Cassie-Baxter icing-based materials. As the novel part, electrospinning which is a straightforward and scalable method was first time used for icephobic applications as a part of our study. Moreover, reported studies are usually beyond some high-tech production methods and some of them may not be suitable for large-scale fabrication processes. However, the electrospinning method can be easily adapted for commercial production systems. The FSFS modified magnetite/r-PET nanocomposite membranes have also unique flexibility, breathability and light-weightiness properties, which makes it much easier to apply them to any surface compared to the metal-based icephobic materials.

There are mainly two concerns of the designed structure in this study. As the icephobic effect was offered by FSFS nanoparticles on the surface of the fibres, their durability is important for both the service life and environmental aspects. More studies need to be carried out to figure out if the nanoparticles migrating to the environment and if so, the potential effects of these nanoparticles on the environment need to be investigated in depth. Secondly, As the r-PET used is a soluble polymer, it is also possible to recycle designed materials using chemical recycling processes many times. However, possible weakening in mechanical properties due to broken polymer chains during the dissolution of the material should be considered.

6.6 Magnetic properties and electromagnetic shielding efficiency of the nanocomposite membranes

The hysteresis loops of the nanocomposite membrane and r-PET itself were measured to study the magnetite nanoparticles' impact on the nanocomposite films' magnetic behaviour. The measurements were carried out at room temperature and the results are shown in Figure 6.11. As expected, there was no magnetic response from the r-PET sample, however, with a loading of 20 wt.% magnetite, a high saturation magnetization with approximately 4.22 emu/g was obtained which proved that although strong solvents (TFA and DCM) were used to prepare the samples, magnetite had not been affected by them which is an important point in terms of electromagnetic shielding efficiency as revealed by the magnetic properties of nanoparticles used.

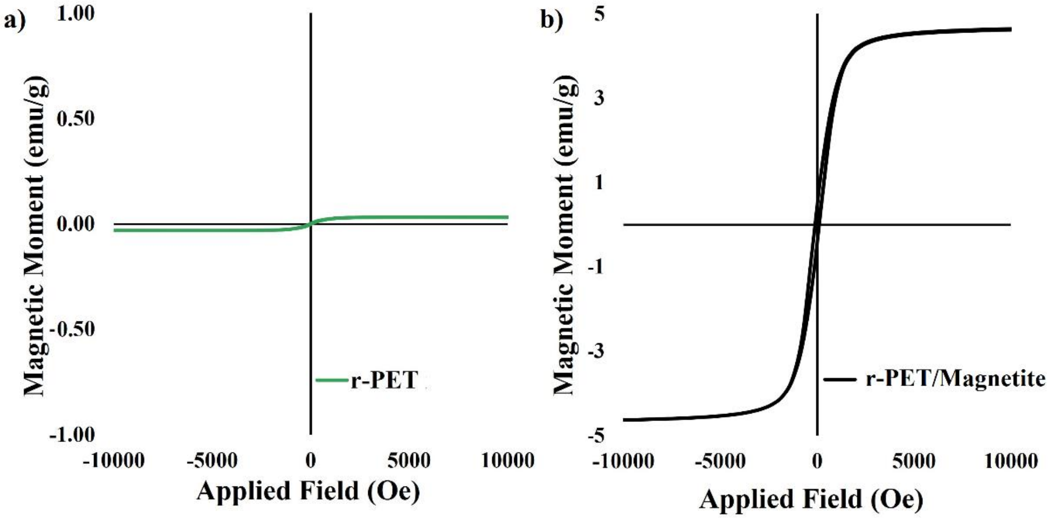

Figure 6. 11 *Magnetic hystereses of (a) r-PET and (b) r-PET/magnetite electrospun samples.*

EMI shielding property of the magnetite is already known as reported in the literature [267-271]. The S_{21} parameter was used to investigate the sample shielding efficiencies, representing the power transferred from Port 2 to Port 1. The electromagnetic shielding efficiency results of r-PET and 20 wt.% mgt/r-PET samples between the range of 400 MHz and 6 GHz are shown in Figure 6.12.

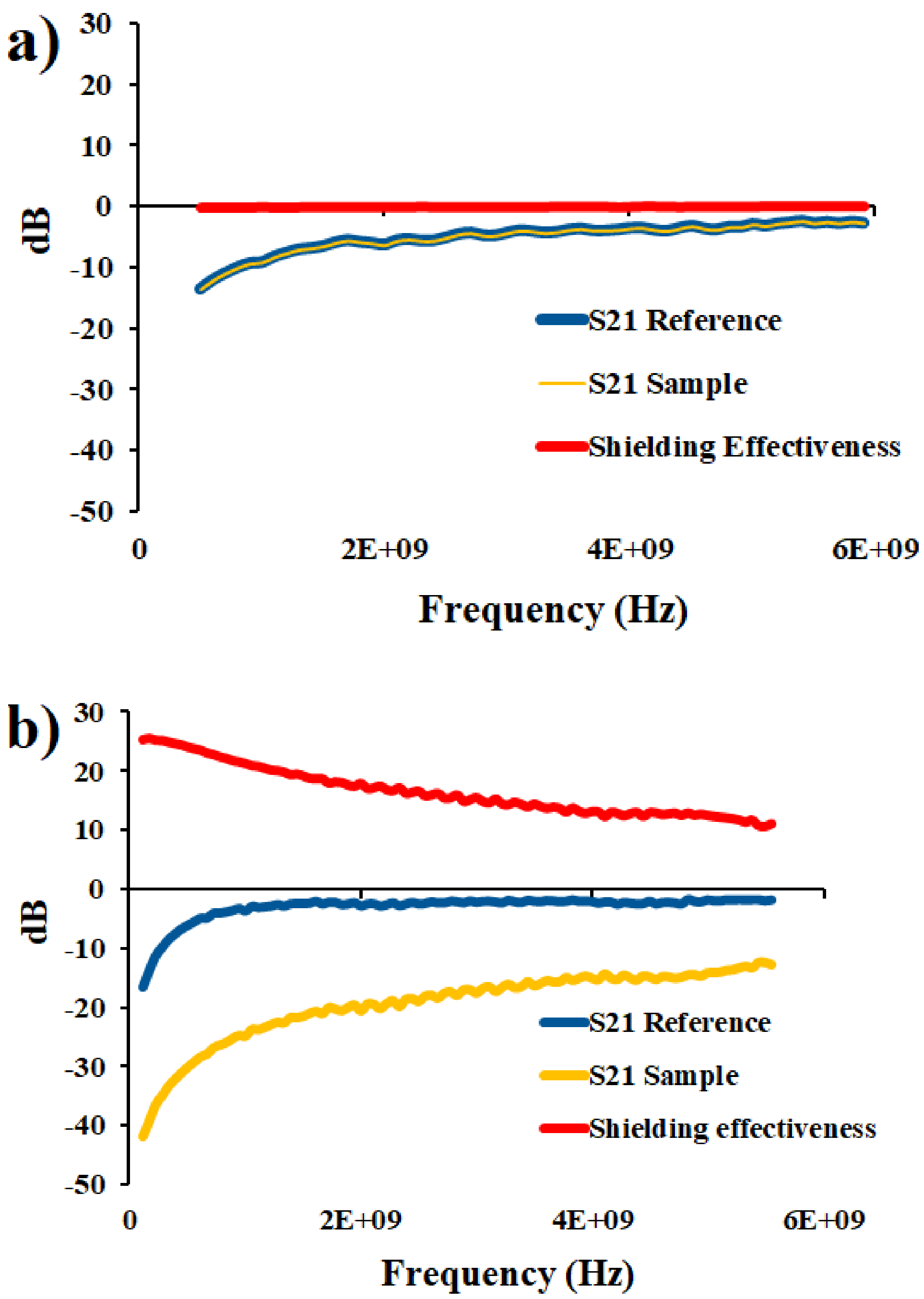

Figure 6. 12 *Electromagnetic shielding efficiency of (a) r-PET and (b) 20 wt.%mgt/r-PET samples (blue line: reference, yellow line: sample and red line: shielding efficiency).*

The r-PET itself did not exhibit any electromagnetic shielding. However, the addition of magnetite provided an efficiency of over 22 dB, corresponding to around 99% shielding efficiency. The combination of the prepared materials' superhydrophobicity and icephobicity properties could prove to be highly suitable EMI shielding materials for outdoor applications (especially in colder climates).

There are three attenuation or loss mechanisms involved in EMI shielding: absorbance, reflectance, and multi-reflectance [272]. As reported previously, reflectance is the major attenuation mechanism when materials with high electrical conductivity and low magnetic permeability are used for electromagnetic shielding because of the impedance mismatch. However, impedance matching needs to be achieved to design a good electromagnetic shielding absorber. Magnetic materials such as magnetite which were used in our study, are known as good electromagnetic absorbers, as they satisfy the impedance matching condition due to the electric permittivity of the magnetite being close to the magnetic permeability in the GHz range. Hence, the major attenuation mechanism of the samples produced was absorption. However, it is also noteworthy that, because of the high conductive behaviour of magnetite, they can easily produce eddy current losses, which may cause reduced permeability at MHz frequencies and the absorption mechanism can be weakened.

The mechanism of electromagnetic shielding with a bulky material or electrospun membrane is given in Figure 6.13. As seen, when the electromagnetic wave hits on the surface of the shielding material, a part of it is reflected while the remaining part penetrates inside. A significant amount of the electromagnetic wave is absorbed by the magnetite nanoparticles inside the fibres by generating a small amount of heat, and some portion of it is reflected inside the membrane. These internal reflected waves eventually will be absorbed by the magnetite and increase the shielding efficiency. This all process can be repeated over and over again inside the electrospun membrane due to the existence of the magnetite nanoparticles and high surface area, and finally, a small part of electromagnetic waves can pass through.

The main contribution to the microwave absorption capability of the r-PET/magnetic nanofibre membrane was attributed to ferromagnetic resonance, which is coupling between the electromagnetic wave and the magnetization of the medium it passes through. This effect reduces the power of the electromagnetic wave significantly and radiates a small amount of heat. Moreover, the magnetite nanoparticles have a small coercitivity value, which is an important point for improving the permeability and hence, the magnetic loss.

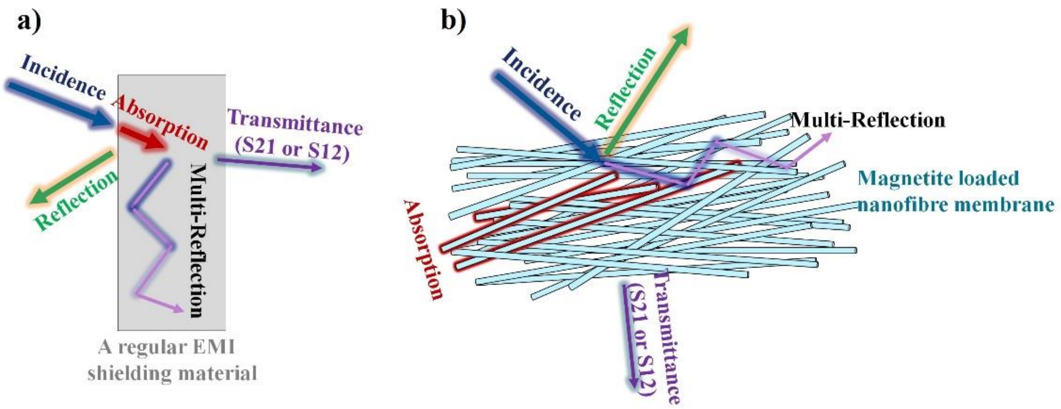

Figure 6. 13 *The schematic representation of the EMI shielding mechanism on (a) bulky materials and (b) electrospun membranes.*

The second factor of good efficiency was the multi-reflection mechanism. In the multi-reflection mechanism, the EMI waves are trapped between two boundaries, as seen in Figure 6.13b. Therefore, the multi-reflection mechanism plays an important role in porous materials and fibrous materials as in electrospun membranes. For the attenuation mechanism of the electrospun membranes, the EMI waves are trapped between the nanofibres, leading to an increase in multi-reflectance loss. Additionally, the large specific surface area of the fibrous membranes may also affect the efficiency of EMI shielding. When the specific surface area of an EMI shielding material increases, the EMI shielding efficiency also increases. It is also notable that the addition of magnetite also affected the fibre diameter distribution, leading to a higher surface area of the electrospun membrane and significantly affecting the multi-reflection loss.

6.7 Summary

In this study, recycled PET-based multifunctional electrospun membranes were produced. Nanoparticle loading and surface modification techniques were used to achieve superhydrophobicity, electromagnetic shielding efficiency, and icephobicity properties. It was found that a 20 wt.% magnetite-loaded nanofibre membrane produced an electromagnetic shielding efficiency of 22 dB, equating to above 99% efficiency. It is believed that the fibrous structure of the electrospun membrane and the pores between the fibres contributed to achieving high efficiency of 22 dB with the increasing multi-reflection loss. Moreover, a low ice adhesion strength compared to the aluminium substrate, and the r-PET electrospun membrane without surface treatment was obtained at around 51 kPa, due to the ability of the FSFS treated surface to exhibit a Cassie-Baxter state instead of the Wenzel state. Due to the icephobic and superhydrophobic properties, the prepared electrospun membranes demonstrate great potential for outdoor EMI shielding applications.

CHAPTER 7

Conclusions and Future Works

7.1 Conclusions

The purpose of this work was to explore the potential of using electrospinning, a versatile method for producing nanofibre membranes, to fabricate superhydrophobic and icephobic surfaces. Electrospun nanofibre membranes having a high surface-to-volume ratio, high porosity, interconnected open pore structures, and adjustable pore sizes were fabricated. The microstructural and performance properties of fabricated electrospun membranes were investigated to explain the mechanism behind the properties achieved.

PVDF-co-HFP, a low-surface polymer, was used to explore the ability of the electrospinning method to fabricate superhydrophobic surfaces using a one-step production method, which offered a shorter fabrication process, more straightforward, and cost-effective, compared to the other methods proposed in the literature. We found that the production and solution parameters have a significant effect on the surface properties of electrospun membranes, as they are dominant parameters that cause the electrospinning instabilities to occur. Varicose and Rayleigh's instabilities contributed to the formation of the beads, which were responsible for the high roughness achieved. In contrast, the whipping instability caused the jet to split into numerous smaller branches and provide nanoscale polymer fibres. The synergetic effect of low surface tension of PVDF-co-HFP, and the high roughness values achieved, provided the superhydrophobicity. The results were also evaluated using the Taguchi method. It was seen that the solvent used was of critical importance in the bead formation, as Rayleigh instability was mostly triggered by the surface tension and volatility of the solvent used. Using different production and solution parameters, surface roughness values between 0.15 μm and

5.77 µm were obtained. As expected, the contact angles were increased with the increasing surface roughness. The highest contact angle value was obtained from DMF-15 at 161°, which revealed one of the highest contact angle hystereses. It was also proved by FTIR and Raman analyses that the electrospinning process did not affect the chemical composition of the PVDF-co-HFP. Hence, the superhydrophobic effect was provided only by changes in the surface properties and the low surface tension of the polymer.

As the electrospun PVDF-co-HFP nanofibre membranes have suitable porosity and oleophilic structure, their potential in being used as the porous part of the slippery liquid-infused porous structures, which is known as one of the promising candidates for icephobic applications, was explored in Chapter 5. For this aim, some outcomes of chapter 4 were used to produce smooth fibrous PVDF-co-HFP electrospun membranes. As a result, an electrospun membrane was produced with a thickness of around 40 µm, and the average fibre diameter was found to be 330 ± 63 nm. More than 90% of the fibres had a diameter between 100 and 400 nm, which offered a high surface area. Thus the high surface area could provide improved contact area between the lubricant and the fibres, resulting in a high level of oil storage. The surface height profile of the sample was also measured, and it was found that the membrane surfaces without lubricant had maximum peak-valley heights of approximately 15 µm. The pores in the structures provided the valleys, while the overlapping fibres provided the peaks. After lubricant infusion, the maximum peak-valley heights of the samples were decreased significantly, indicating that the lubricant had filled most of the pores.

Additionally, the water contact angle of the electrospun membrane was measured as 141°, while the lubricant-infused membranes exhibited significantly lower contact angle values. This reduction was contributed by the lower surface roughness values and the effect of infinite soft substrates (lubricants). However, although all SLIPS have lower static contact angles, they also have significantly lower contact angle hysteresis than the as-produced PVDF-co-HFP electrospun membrane. These results indicated high mobility of the water droplet on the surface and proved that the encapsulated regime, which was critical for low-ice adhesion, had been achieved. It was found that all lubricants provided a low ice adhesion strength, lower than 5 kPa. Droplet icing time values of the samples were improved significantly, from 5 seconds to 40 seconds because of lower thermal convection. Additionally, more than 90% of transparency was obtained using silicone oil and PcTFE as the lubricant, due to the refractive index matching of lubricant and polymer used. The produced SLIPS could be proposed for applications in solar energy harvesting systems, in which both icing and transparency are critical issues.

As some additional properties are required for large applications of superhydrophobic and icephobic surfaces, a novel multifunctional electrospun nanofibre membrane was also designed for outdoor electromagnetic shielding applications. As the SLIPS-like structures are not yet suitable for harsh environmental conditions, icephobic properties were imparted using a surface modification technique. In line with this aim, two main properties were focused on, namely electromagnetic shielding efficiency and icephobicity. For the electromagnetic shielding efficiency, magnetite, a useful electromagnetic absorber, was used as a filler, and a nanofibre-based r-PET/magnetite nanocomposite membrane was fabricated via an electrospinning process. To impart icephobic properties to the fabricated nanocomposite electrospun membrane, fluorinated silane functionalized SiO_2 particles were used. The average fibre diameter of the r-PET electrospun membrane was 372 ± 132 nm, and the majority of the fibres were between 150 and 550 nm in diameter. However, the addition of magnetite to the polymer revealed a dramatic change in the distribution of fibre diameters, whereby the majority of the fibres displayed a diameter of between 50 and 350 nm. This change was attributed to the whipping instability related to surface tension and the viscosity of the polymer solution. After dip coating with FSFS was carried out, both the surface chemistry and morphology changed significantly as the FSFS nanoparticles were accumulated on the surface of the fibres; this can be advantageous in achieving superhydrophobicity, due to the relatively hierarchical structure.

This treatment also changed the wetting state of the electrospun nanofibre membrane. The FSFS treated nanofibre membranes exhibited the Cassie-Baxter state, in which the droplet of water sits on top of the roughness structures and air pockets. In contrast, the samples without FSFS treatment displayed the Wenzel state when contacting water, which resulted in water penetration into the air gaps between the fibres. After this treatment, electrospun nanocomposite membranes exhibited around 50 kPa of ice adhesion strength, significantly lower than those without FSFS treatment. The wetting state played a critical role in the icing interface, dramatically affecting the ice adhesion strength. In the Wenzel state, the required work to remove ice from the surface was much higher due to the high icing interface. However, it was significantly lower when the Cassie-Baxter state was exhibited because of the lower icing interface. Moreover, 10 – 22 dB of electromagnetic shielding efficiency was obtained at 400 MHz and 6 GHz. The main contribution to the microwave absorption capability of the r-PET/magnetic nanofibre membrane was attributed to ferromagnetic resonance, which is coupling between the electromagnetic wave and the magnetisation of the medium it passes through. This effect reduces the power of the electromagnetic wave significantly and radiates a small amount of heat. Additionally, in the attenuation mechanism of the electrospun membranes, the EMI waves are trapped between the nanofibres, leading to an increase in multi-reflectance loss.

7.2 Future Work

The electrospinning method and polymer-based electrospun membranes have great potential for applications in superhydrophobic and icephobic surfaces. However, some issues still need to be addressed in the electrospinning method for commercial applications.

The effect of electrospinning and solution parameters on surface topography and superhydrophobicity of the electrospun membranes needs to be investigated using different polymers with different surface tensions. More importantly, theoretical studies need to be carried out to understand the mechanism behind the beads, cones, and thin fibres formed. It is essential to understand exactly how different polymers are affected by the instabilities of the electrospinning system. After this has been understood, it will be possible to control these instabilities to manipulate the surface structure as needed. For commercial applications, strategies to apply developed superhydrophobic nanofibre membranes to the different types, shapes and sizes of materials should be considered.

Many applications require a significant level of strength in the surface or coating used. Thus, the mechanical properties of electrospun membranes need to be enhanced using post-treatment methods to improve the adhesion of the fibres' interconnected points or nanofillers, to enhance the tensile strengths of nanofibre membranes fabricated. Moreover, the crystallinity level of the fibres, and the effect of the solvent system used on the molecular crystallinity, needs to be understood as this is one of the most important variables affecting the strength of the electrospun membrane.

The real-life applications and the challenges that may be faced should be considered for designed icephobic and superhydrophobic materials. For example, the environmental effect of lubricant evaporated from the SLIPS needs to be studied. Different approaches should be developed to keep the lubricant inside the porous structure without evaporation, for a longer period. Moreover, the samples having nanoparticles also should be investigated further to see if they are spreading around the environment and possible improvements need to be carried out to reduce their environmental effect.

Moreover, the versatility of this method makes it promising for the fabrication of multifunctional surfaces, which can help to overcome many challenges in modern life. However, there is a strong need to understand the particular requirements of specific applications, and to design multifunctional electrospun membranes accordingly. After that, it will be possible to fabricate high-efficiency products by choosing the correct combination of polymer, nanofiller, and post-treatment. This selection is also critical for the durability of the functions achieved, which is a significant challenge that could hinder the commercial adoption of nanofibre-based products.

References

1. Darband, G.B., et al., *Science and Engineering of Superhydrophobic Surfaces: Review of Corrosion Resistance, Chemical and Mechanical Stability*. Arabian Journal of Chemistry, 2020. **13**(1): p. 1763-1802.
2. Lee, C., C.H. Choi, and C.J. Kim, *Superhydrophobic drag reduction in laminar flows: a critical review*. Experiments in Fluids, 2016. **57**(12): 1-20.
3. Jeevahan, J., et al., *Superhydrophobic surfaces: a review on fundamentals, applications, and challenges*. Journal of Coatings Technology and Research, 2018. **15**(2): p. 231-250.
4. Latthe, S.S., et al., *Superhydrophobic surfaces for oil-water separation*, in *Superhydrophobic Polymer Coatings*. 2019, Elsevier. p. 339-356.
5. Datamintelligence. *Superhydrophobic Coatings Market, Size, Share, Growth, Trends, Insight and Industry Forecast, 2021-2028*. 2021 [cited 2021].
6. Zhang, S.N., et al., *Bioinspired Surfaces with Superwettability for Anti-Icing and Ice-Phobic Application: Concept, Mechanism, and Design*. Small, 2017. **13**(48): 1701867.
7. Wu, X.H., et al., *When superhydrophobic coatings are icephobic: Role of surface topology*. Surface & Coatings Technology, 2019. **358**: p. 207-214.
8. Nosonovsky, M. and V. Hejazi, *Why Superhydrophobic Surfaces Are Not Always Icephobic*. ACS Nano, 2012. **6**(10): p. 8488-8491.
9. Kreder, M.J., et al., *Design of anti-icing surfaces: smooth, textured or slippery?* Nature Reviews Materials, 2016. **1**(1): p. 1-15.
10. Wong, T.S., et al., *Bioinspired self-repairing slippery surfaces with pressure-stable omniphobicity*. Nature, 2011. **477**(7365): p. 443-447.
11. Loh, K.J.-H., *Development of Multifunctional Carbon Nanotube Nanocomposite Sensors for Structural Health Monitoring*. University of Michigan, 2008.
12. Zamanian, A. and C. Hardiman, *Electromagnetic radiation and human health: A review of sources and effects*. High Frequency Electronics, 2005. **4**(3): p. 16-26.

13. Li, Y., et al., *Electrical conductivity and electromagnetic interference shielding characteristics of multiwalled carbon nanotube filled polyacrylate composite films.* Applied Surface Science, 2008. **254**(18): p. 5766-5771.
14. Lin, C.T., et al., *Nanograin magnetoresistive manganite coatings for EMI shielding against directed energy pulses.* Progress in Organic Coatings, 2003. **47**(3-4): p. 190-197.
15. Tucker, N., et al., *The History of the Science and Technology of Electrospinning from 1600 to 1995.* Journal of Engineered Fibers and Fabrics, 2012. **7**: p. 63-73.
16. Bhardwaj, N. and S.C. Kundu, *Electrospinning: A fascinating fiber fabrication technique.* Biotechnology Advances, 2010. **28**(3): p. 325-347.
17. Teo, W.E. and S. Ramakrishna*, A review on electrospinning design and nanofibre assemblies.* Nanotechnology, 2006. **17**(14): p. R89-R106.
18. H. Kiyohiko*, Process for manufacturing artificial silk and other filaments by applying electric current*, U.S. Patent No. 1,699,615. 22 Jan. 1929.
19. F. Anton*, Process and apparatus for preparing artificial threads*, U.S. Patent No. 1,975,504. 2 Oct. 1934.
20. De Vrieze, S. and K. De Clerck. *80 years of electrospinning*. in *International conference on Latest Advances in High-Tech Textiles and Textile-Based Materials*. 2009. Ghent University. Department of Textiles.
21. Nayak, R., *Review of Literature: Melt Electrospinning*, in *Polypropylene Nanofibers: Melt Electrospinning Versus Meltblowing*. 2017, Springer International Publishing: Cham. p. 9-39.
22. Taylor, G.I., *Disintegration of water drops in an electric field.* Proceedings of the Royal Society of London. Series A. Mathematical and Physical Sciences, 1964. **280**(1382): p. 383-397.
23. Khalil, A., et al., *Electrospun metallic nanowires: Synthesis, characterization, and applications.* Journal of Applied Physics, 2013. **114**(17): 12_1.
24. Agrahari, V., et al., *Chapter 9 - Electrospun Nanofibers in Drug Delivery: Fabrication, Advances, and Biomedical Applications*, in *Emerging Nanotechnologies for Diagnostics, Drug Delivery and Medical Devices*,

A.K. Mitra, K. Cholkar, and A. Mandal, Editors. 2017, Elsevier: Boston. p. 189-215.

25. Sundarrajan, S., et al., *Electrospun Nanofibers for Air Filtration Applications.* International Conference on Materials for Advanced Technologies (Icmat2013), Symposium W - Advanced Structural and Functional Materials for Protection, 2014. **75**: p. 159-163.
26. Naghibzadeh, M., et al., *Application of electrospun gelatin nanofibers in tissue engineering.* Biointerface Research in Applied Chemistry, 2018. **8**(1): p. 3048-3052.
27. Chen, S.X., et al., *Recent advances in electrospun nanofibers for wound healing.* Nanomedicine, 2017. **12**(11): p. 1335-1352.
28. Sun, G.R., et al., *Electrospinning of Nanofibers for Energy Applications.* Nanomaterials, 2016. **6**(7): 129.
29. Wang, X.F., B. Ding, and J.Y. Yu, *Functional nanofibers in sensor applications.* Functional Nanofibers and Their Applications, 2012(134): p. 209-235.
30. Nuraje, N., et al., *Superhydrophobic electrospun nanofibers.* Journal of Materials Chemistry A, 2013. **1**(6): p. 1929-1946.
31. Kannan, B., H. Cha, and I.C. Hosie, *Electrospinning—Commercial applications, challenges and opportunities*, in *Nano-size Polymers*. 2016, Springer. p. 309-342.
32. Rogina, A., *Electrospinning process: Versatile preparation method for biodegradable and natural polymers and biocomposite systems applied in tissue engineering and drug delivery.* Applied Surface Science, 2014. **296**: p. 221-230.
33. Kamarudin, M.A., et al., *A Review on the Fabrication of Polymer-Based Thermoelectric Materials and Fabrication Methods.* Scientific World Journal, 2013.
34. Garg, K. and G.L. Bowlin, *Electrospinning jets and nanofibrous structures.* Biomicrofluidics, 2011. **5**(1).
35. Deitzel, J.M., et al., *Key parameters influencing the onset and maintenance of the electrospinning jet.* Polymeric Nanofibers, 2006. **918**: p. 56-73.

36. Baumgarten, P.K., *Electrostatic Spinning of Acrylic Microfibers.* Journal of Colloid and Interface Science, 1971. **36**(1): p. 71-90.
37. Reneker, D.H., et al., *Bending instability of electrically charged liquid jets of polymer solutions in electrospinning.* Journal of Applied Physics, 2000. **87**(9): p. 4531-4547.
38. Reneker, D.H. and A.L. Yarin, *Electrospinning jets and polymer nanofibers.* Polymer, 2008. **49**(10): p. 2387-2425.
39. Hohman, M.M., et al., *Electrospinning and electrically forced jets. II. Applications.* Physics of Fluids, 2001. **13**(8): p. 2221-2236.
40. Golecki, H.M., et al., *Effect of Solvent Evaporation on Fiber Morphology in Rotary Jet Spinning.* Langmuir, 2014. **30**(44): p. 13369-13374.
41. Sun, Z.C., et al., *Compound core-shell polymer nanofibers by co-electrospinning.* Advanced Materials, 2003. **15**(22): p. 1929-1939.
42. Qu, H.L., S.Y. Wei, and Z.H. Guo, *Coaxial electrospun nanostructures and their applications.* Journal of Materials Chemistry A, 2013. **1**(38): p. 11513-11528.
43. Kidoaki, S., I.K. Kwon, and T. Matsuda, *Mesoscopic spatial designs of nano- and microfiber meshes for tissue-engineering matrix and scaffold based on newly devised multilayering and mixing electrospinning techniques.* Biomaterials, 2005. **26**(1): p. 37-46.
44. Levorson, E.J., et al., *Fabrication and characterization of multiscale electrospun scaffolds for cartilage regeneration.* Biomedical Materials, 2013. **8**(1): 014103.
45. Jing, P.P., et al., *Hierarchical $SrTiO_3/NiFe_2O_4$ composite nanostructures with excellent light response and magnetic performance synthesized toward enhanced photocatalytic activity.* Nanoscale, 2015. **7**(35): p. 14738-14746.
46. Persano, L., et al., *Industrial upscaling of electrospinning and applications of polymer nanofibers: a review.* Macromolecular Materials and Engineering, 2013. **298**(5): p. 504-520.
47. Jiang, H.L., et al., *Optimization and characterization of dextran membranes prepared by electrospinning.* Biomacromolecules, 2004. **5**(2): p. 326-333.

48. Huang, L., et al., *Engineered collagen-PEO nanofibers and fabrics.* Journal of Biomaterials Science-Polymer Edition, 2001. **12**(9): p. 979-993.
49. Zhao, Z.Z., et al., *Preparation and properties of electrospun poly(vinylidene fluoride) membranes.* Journal of Applied Polymer Science, 2005. **97**(2): p. 466-474.
50. Zhang, C.X., et al., *Study on morphology of electrospun poly(vinyl alcohol) mats.* European Polymer Journal, 2005. **41**(3): p. 423-432.
51. Kim, B., et al., *Poly(acrylic acid) nanofibers by electrospinning.* Materials Letters, 2005. **59**(7): p. 829-832.
52. Son, W.K., et al., *The effects of solution properties and polyelectrolyte on electrospinning of ultrafine poly(ethylene oxide) fibers.* Polymer, 2004. **45**(9): p. 2959-2966.
53. Chen, V.J. and P.X. Ma, *Nano-fibrous poly(L-lactic acid) scaffolds with interconnected spherical macropores.* Biomaterials, 2004. **25**(11): p. 2065-2073.
54. Demir, M.M., et al., *Electrospinning of polyurethane fibers.* Polymer, 2002. **43**(11): p. 3303-3309.
55. Jun, Z., et al., *Poly-L-lactide nanofibers by electrospinning - Influence of solution viscosity and electrical conductivity on fiber diameter and fiber morphology.* E-Polymers, 2003.
56. Hohman, M.M., et al., *Electrospinning and electrically forced jets. I. Stability theory.* Physics of Fluids, 2001. **13**(8): p. 2201-2220.
57. Supaphol, P., C. Mit-Uppatham, and M. Nithitanakul, *Ultrafine electrospun polyamide-6 fibers: Effect of emitting electrode polarity on morphology and average fiber diameter.* Journal of Polymer Science Part B-Polymer Physics, 2005. **43**(24): p. 3699-3712.
58. Ki, C.S., et al., *Characterization of gelatin nanofiber prepared from gelatin-formic acid solution.* Polymer, 2005. **46**(14): p. 5094-5102.
59. Geng, X.Y., O.H. Kwon, and J.H. Jang, *Electrospinning of chitosan dissolved in concentrated acetic acid solution.* Biomaterials, 2005. **26**(27): p. 5427-5432.

60. Buchko, C.J., et al., *Processing and microstructural characterization of porous biocompatible protein polymer thin films.* Polymer, 1999. **40**(26): p. 7397-7407.
61. Zuo, W.W., et al., *Experimental study on relationship between jet instability and formation of beaded fibers during electrospinning.* Polymer Engineering and Science, 2005. **45**(5): p. 704-709.
62. Pelipenko, J., et al., *The impact of relative humidity during electrospinning on the morphology and mechanical properties of nanofibers.* International Journal of Pharmaceutics, 2013. **456**(1): p. 125-134.
63. De Vrieze, S., et al., *The effect of temperature and humidity on electrospinning.* Journal of Materials Science, 2009. **44**(5): p. 1357-1362.
64. Shao, H., et al., *Effect of electrospinning parameters and polymer concentrations on mechanical-to-electrical energy conversion of randomly-oriented electrospun poly (vinylidene fluoride) nanofiber mats.* RSC Advances, 2015. **5**(19): p. 14345-14350.
65. Haider, A., S. Haider, and I.K. Kang, *A comprehensive review summarizing the effect of electrospinning parameters and potential applications of nanofibers in biomedical and biotechnology.* Arabian Journal of Chemistry, 2018. **11**(8): p. 1165-1188.
66. Tan, S.-H., et al., *Systematic parameter study for ultra-fine fiber fabrication via electrospinning process.* Polymer, 2005. **46**(16): p. 6128-6134.
67. Megelski, S., et al., *Micro- and nanostructured surface morphology on electrospun polymer fibers.* Macromolecules, 2002. **35**(22): p. 8456-8466.
68. Zargham, S., et al., *The Effect of Flow Rate on Morphology and Deposition Area of Electrospun Nylon 6 Nanofiber.* Journal of Engineered Fibers and Fabrics, 2012. **7**(4): p. 42-49.
69. Subbiah, T., et al., *Electrospinning of nanofibers.* Journal of Applied Polymer Science, 2005. **96**(2): p. 557-569.
70. Wang, T. and S. Kumar, *Electrospinning of polyacrylonitrile nanofibers.* Journal of Applied Polymer Science, 2006. **102**(2): p. 1023-1029.

71. Bhushan, B. and Y.C. Jung, *Natural and biomimetic artificial surfaces for superhydrophobicity, self-cleaning, low adhesion, and drag reduction.* Progress in Materials Science, 2011. **56**(1): p. 1-108.
72. Gould, P., *Smart, clean surfaces.* Materials Today, 2003. **6**(11): p. 44-48.
73. Dai, X.M., et al., *Slippery Wenzel State.* ACS Nano, 2015. **9**(9): p. 9260-9267.
74. Liu, T.L., Z. Chen, and C.-J. Kim, *A dynamic Cassie–Baxter model.* Soft Matter, 2015. **11**(8): p. 1589-1596.
75. Shoute, L.C.T., et al., *Threshold hydrophobicity for inhibition of salt scale formation on SAM-modified titania nanotube arrays.* Applied Surface Science, 2019. **473**: p. 282-290.
76. Huhtamaki, T., et al., *Surface-wetting characterization using contact-angle measurements.* Nature Protocols, 2018. **13**(7): p. 1521-1538.
77. Ma, M. and R.M. Hill, *Superhydrophobic surfaces.* Current Opinion in Colloid & Interface Science, 2006. **11**(4): p. 193-202.
78. Xue, C.H., et al., *Large-area fabrication of superhydrophobic surfaces for practical applications: an overview.* Science and Technology of Advanced Materials, 2010. **11**(3).
79. Xue, C.-H., et al., *Superhydrophobic surfaces on cotton textiles by complex coating of silica nanoparticles and hydrophobization.* Thin Solid Films, 2009. **517**(16): p. 4593-4598.
80. Bergbreiter, D.E. and K.-S. Liao, *Covalent layer-by-layer assembly—an effective, forgiving way to construct functional robust ultrathin films and nanocomposites.* Soft Matter, 2009. **5**(1): p. 23-28.
81. Ming, W., et al., *Superhydrophobic films from raspberry-like particles.* Nano Letters, 2005. **5**(11): p. 2298-2301.
82. Amigoni, S., et al., *Covalent layer-by-layer assembled superhydrophobic organic− inorganic hybrid films.* Langmuir, 2009. **25**(18): p. 11073-11077.
83. Levkin, P.A., F. Svec, and J.M. Fréchet, *Porous polymer coatings: a versatile approach to superhydrophobic surfaces.* Advanced Functional Materials, 2009. **19**(12): p. 1993-1998.

84. Roach, P., N.J. Shirtcliffe, and M.I. Newton, *Progess in superhydrophobic surface development.* Soft Matter, 2008. **4**(2): p. 224-240.

85. Yuan, Z., et al., *A stable porous superhydrophobic high-density polyethylene surface prepared by adding ethanol in humid atmosphere.* Journal of Applied Polymer Science, 2009. **113**(3): p. 1626-1632.

86. Chen, H., et al., *Preparation, characterization and wettability of porous superhydrophobic poly (vinyl chloride) surface.* Journal of Porous Materials, 2009. **16**(4): p. 447-451.

87. Zimmermann, J., et al., *A simple, one-step approach to durable and robust superhydrophobic textiles.* Advanced Functional Materials, 2008. **18**(22): p. 3662-3669.

88. Xu, B. and Z. Cai, *Fabrication of a superhydrophobic ZnO nanorod array film on cotton fabrics via a wet chemical route and hydrophobic modification.* Applied Surface Science, 2008. **254**(18): p. 5899-5904.

89. Leng, B., et al., *Superoleophobic cotton textiles.* Langmuir, 2009. **25**(4): p. 2456-2460.

90. Xiu, Y., D.W. Hess, and C. Wong, *UV and thermally stable superhydrophobic coatings from sol–gel processing.* Journal of Colloid and Interface Science, 2008. **326**(2): p. 465-470.

91. Latthe, S.S., et al., *Superhydrophobic silica films by sol–gel co-precursor method.* Applied Surface Science, 2009. **256**(1): p. 217-222.

92. Yu, M., et al., *Superhydrophobic cotton fabric coating based on a complex layer of silica nanoparticles and perfluorooctylated quaternary ammonium silane coupling agent.* Applied Surface Science, 2007. **253**(7): p. 3669-3673.

93. Zhang, J.L., J.A. Li, and Y.C. Han, *Superhydrophobic PTFE surfaces by extension.* Macromolecular Rapid Communications, 2004. **25**(11): p. 1105-1108.

94. Shiu, J.Y., et al., *Fabrication of tunable superhydrophobic surfaces by nanosphere lithography.* Chemistry of Materials, 2004. **16**(4): p. 561-564.

95. Yabu, H. and M. Shimomura, *Single-step fabrication of transparent superhydrophobic porous polymer films.* Chemistry of Materials, 2005. **17**(21): p. 5231-5234.

96. Xu, L.B., et al., *Reversible conversion of conducting polymer films from superhydrophobic to superhydrophilic.* Angewandte Chemie-International Edition, 2005. **44**(37): p. 6009-6012.

97. Khorasani, M.T., H. Mirzadeh, and Z. Kermani, *Wettability of porous polydimethylsiloxane surface: morphology study.* Applied Surface Science, 2005. **242**(3-4): p. 339-345.

98. Alchetron.com/, *Polydimethylsiloxane*, in, https://alchetron.com/Polydimethylsiloxane, [cited 2021].

99. Jin, M.H., et al., *Super-hydrophobic PDMS surface with ultra-low adhesive force.* Macromolecular Rapid Communications, 2005. **26**(22): p. 1805-1809.

100. Sun, M.H., et al., *Artificial lotus leaf by nanocasting.* Langmuir, 2005. **21**(19): p. 8978-8981.

101. Ma, M.L., et al., *Electrospun poly(styrene-block-dimethylsiloxane) block copolymer fibers exhibiting superhydrophobicity.* Langmuir, 2005. **21**(12): p. 5549-5554.

102. Zhao, N., et al., *Superhydrophobic surface from vapor-induced phase separation of copolymer micellar solution.* Macromolecules, 2005. **38**(22): p. 8996-8999.

103. Lu, X.Y., C.C. Zhang, and Y.C. Han, *Low-density polyethylene superhydrophobic surface by control of its crystallization behavior.* Macromolecular Rapid Communications, 2004. **25**(18): p. 1606-1610.

104. Feng, X.J., et al., *Reversible super-hydrophobicity to super-hydrophilicity transition of aligned ZnO nanorod films.* Journal of the American Chemical Society, 2004. **126**(1): p. 62-63.

105. Shirtcliffe, N.J., et al., *Porous materials show superhydrophobic to superhydrophilic switching.* Chemical Communications, 2005(25): p. 3135-3137.

106. Hikita, M., et al., *Super-liquid-repellent surfaces prepared by colloidal silica nanoparticles covered with fluoroalkyl groups.* Langmuir, 2005. **21**(16): p. 7299-7302.

107. Shang, H.M., et al., *Optically transparent superhydrophobic silica-based films.* Thin Solid Films, 2005. **472**(1-2): p. 37-43.

108. Ma, M.L. and R.M. Hill, *Superhydrophobic surfaces.* Current Opinion in Colloid & Interface Science, 2006. **11**(4): p. 193-202.

109. Teshima, K., et al., *Transparent ultra water-repellent poly(ethylene terephthalate) substrates fabricated by oxygen plasma treatment and subsequent hydrophobic coating.* Applied Surface Science, 2005. **244**(1-4): p. 619-622.

110. Qian, B.T. and Z.Q. Shen, *Fabrication of superhydrophobic surfaces by dislocation-selective chemical etching on aluminum, copper, and zinc substrates.* Langmuir, 2005. **21**(20): p. 9007-9009.

111. Martines, E., et al., *Superhydrophobicity and superhydrophilicity of regular nanopatterns.* Nano Letters, 2005. **5**(10): p. 2097-2103.

112. Zhai, L., et al., *Stable superhydrophobic coatings from polyelectrolyte multilayers.* Nano Letters, 2004. **4**(7): p. 1349-1353.

113. Rodriguez, C.A.D. and G. Tremiliosi-Filho, *Electrochemical Deposition*, in *Encyclopedia of Tribology*, Q.J. Wang and Y.-W. Chung, Editors. 2013, Springer US: Boston, MA. p. 918-922.

114. Zhang, X., et al., *Polyelectrolyte multilayer as matrix for electrochemical deposition of gold clusters: toward super-hydrophobic surface.* Journal of the American Chemical Society, 2004. **126**(10): p. 3064-3065.

115. Shirtcliffe, N.J., et al., *Dual-scale roughness produces unusually water-repellent surfaces.* Advanced Materials, 2004. **16**(21): p. 1929-+.

116. Il Yoon, Y., et al., *Superhydrophobicity of PHBV fibrous surface with bead-on-string structure.* Journal of Colloid and Interface Science, 2008. **320**(1): p. 91-95.

117. Karim, M.R. and M.S. Islam, *Thermal Behavior with Mechanical Property of Fluorinated Silane Functionalized Superhydrophobic*

Pullulan/Poly(vinyl alcohol) Blends by Electrospinning Method. Journal of Nanomaterials, 2011.

118. Wang, L.F., et al., *Fabrication of superhydrophobic TPU film for oil-water separation based on electrospinning route.* Materials Letters, 2011. **65**(5): p. 869-872.
119. Cakir, M., I. Kartal, and Z. Yildiz, *The preparation of UV-cured superhydrophobic cotton fabric surfaces by electrospinning method.* Textile Research Journal, 2014. **84**(14): p. 1528-1538.
120. Meikandan, M. and K. Malarmohan, *Fabrication of a Superhydrophobic Nanofibres by Electrospinning.* Digest Journal of Nanomaterials and Biostructures, 2017. **12**(1): p. 11-17.
121. Liu, Z.J., et al., *Durable and self-healing superhydrophobic surface with bistratal gas layers prepared by electrospinning and hydrothermal processes.* Chemical Engineering Journal, 2017. **326**: p. 578-586.
122. Cao, S.J., et al., *Superhydrophobic PES/PDA/ODTS fibrous mat prepared by electrospinning and silanization modification for oil/water separation.* Journal of Applied Polymer Science, 2018. **135**(12).
123. Cui, M., et al., *Electrospinning superhydrophobic nanofibrous poly(vinylidene fluoride)/stearic acid coatings with excellent corrosion resistance.* Thin Solid Films, 2018. **657**: p. 88-94.
124. Han, D.W. and A.J. Steckl, *Superhydrophobic and Oleophobic Fibers by Coaxial Electrospinning.* Langmuir, 2009. **25**(16): p. 9454-9462.
125. Zhan, N.Q., et al., *A novel multinozzle electrospinning process for preparing superhydrophobic PS films with controllable bead-on-string/microfiber morphology.* Journal of Colloid and Interface Science, 2010. **345**(2): p. 491-495.
126. Wang, S., et al., *Fabrication of large-scale superhydrophobic composite films with enhanced tensile properties by multinozzle conveyor belt electrospinning.* Journal of Applied Polymer Science, 2014. **131**(1).
127. Su, C.L., et al., *Fabrication of three-dimensional superhydrophobic membranes with high porosity via simultaneous electrospraying and electrospinning.* Materials Letters, 2016. **170**: p. 67-71.

128. Yang, J., et al., *Feedback System Control Optimized Electrospinning for Fabrication of an Excellent Superhydrophobic Surface.* Nanomaterials, 2017. **7**(10): 319.

129. Wu, J., et al., *Rinse-resistant superhydrophobic block copolymer fabrics by electrospinning, electrospraying and thermally-induced self-assembly.* Applied Surface Science, 2017. **422**: p. 769-777.

130. Wang, S.A., et al., *Preparation of a durable superhydrophobic membrane by electrospinning poly (vinylidene fluoride) (PVDF) mixed with epoxy-siloxane modified SiO_2 nanoparticles: A possible route to superhydrophobic surfaces with low water sliding angle and high water contact angle.* Journal of Colloid and Interface Science, 2011. **359**(2): p. 380-388.

131. Hardman, S.J., et al., *Electrospinning Superhydrophobic Fibers Using Surface Segregating End-Functionalized Polymer Additives.* Macromolecules, 2011. **44**(16): p. 6461-6470.

132. Ganesh, V.A., et al., *Superhydrophobic fluorinated POSS-PVDF-HFP nanocomposite coating on glass by electrospinning.* Journal of Materials Chemistry, 2012. **22**(35): p. 18479-18485.

133. Song, Y., et al., *Preparation of a New Superhydrophobic Nanofiber Film by Electrospinning Polystyrene Mixed with Ester Modified Silicone Oil.* Journal of Applied Polymer Science, 2014. **131**(17).

134. Liu, Z.J., et al., *Superhydrophobic poly(vinylidene fluoride) membranes with controllable structure and tunable wettability prepared by one-step electrospinning.* Polymer, 2016. **82**: p. 105-113.

135. Ok, S., et al., *Near superhydrophobic-fluorinated THV fiber-like structures and fibers prepared by electrospinning.* High Performance Polymers, 2016. **28**(2): p. 206-214.

136. Tijing, L.D., et al., *Superhydrophobic nanofiber membrane containing carbon nanotubes for high-performance direct contact membrane distillation.* Journal of Membrane Science, 2016. **502**: p. 158-170.

137. Sun, H.X., et al., *Preparation of superhydrophobic nanocomposite fiber membranes by electrospinning poly(vinylidene fluoride)/silane coupling*

agent modified SiO_2 nanoparticles. Journal of Applied Polymer Science, 2017. **134**(13):44501.

138. Menini, R. and M. Farzaneh, *Advanced Icephobic Coatings.* Journal of Adhesion Science and Technology, 2011. **25**(9): p. 971-992.
139. Zhuo, Y.Z., et al., *One-Step Fabrication of Bioinspired Lubricant-Regenerable Icephobic Slippery Liquid-Infused Porous Surfaces.* ACS Omega, 2018. **3**(8): p. 10139-10144.
140. Zheng, H.K., S.N. Chang, and Y.Y. Zhao, *Anti-Icing & Icephobic Mechanism and Applications of Superhydrophobic/Ultra Slippery Surface.* Progress in Chemistry, 2017. **29**(1): p. 102-118.
141. Irajizad, P., et al., *Magnetic slippery extreme icephobic surfaces.* Nature Communications, 2016. **7**: 1-7.
142. Parent, O. and A. Ilinca, *Anti-icing and de-icing techniques for wind turbines: Critical review.* Cold Regions Science and Technology, 2011. **65**(1): p. 88-96.
143. Murphy, C., et al., *Treatment performance of an aerated constructed wetland treating glycol from de-icing operations at a UK airport.* Ecological Engineering, 2015. **80**: p. 117-124.
144. de Andrés, C.R.d.A., S. Saarinen, and A. Uuskallio, R*eview of ice challenges and ice management in port areas*. Coastal Engineering Proceedings, 2018. **1**(36): p. 79.
145. Shen, Y., et al., *Icephobic materials: fundamentals, performance evaluation, and applications.* Progress in Materials Science, 2019.
146. Cooper, S.J., C.E. Nicholson, and J. Liu, *A simple classical model for predicting onset crystallization temperatures on curved substrates and its implications for phase transitions in confined volumes.* Journal of Chemical Physics, 2008. **129**(12):124715.
147. Petrenko, V.F. and S. Qi, *Reduction of ice adhesion to stainless steel by ice electrolysis.* Journal of Applied Physics, 1999. **86**(10): p. 5450-5454.
148. Subramanyam, S.B., G. Azimi, and K.K. Varanasi, *Designing Lubricant-Impregnated Textured Surfaces to Resist Scale Formation.* Advanced Materials Interfaces, 2014. **1**(2): p. 1300068.

149. Zhang, P., et al., *Stable slippery liquid-infused anti-wetting surface at high temperatures.* Journal of Materials Chemistry A, 2016. **4**(31): p. 12212-12220.

150. Yang, S., et al., *Slippery liquid-infused porous surface based on perfluorinated lubricant/iron tetradecanoate: Preparation and corrosion protection application.* Applied Surface Science, 2015. **328**: p. 491-500.

151. Deng, R., et al., *Slippery liquid-infused porous surfaces (SLIPSs): a perfect solution to both marine fouling and corrosion?* Journal of Materials Chemistry A, 2020. **8**(16): p. 7536-7547.

152. You, I., et al., *Fabrication of a micro-omnifluidic device by omniphilic/omniphobic patterning on nanostructured surfaces.* ACS Nano, 2014. **8**(9): p. 9016-9024.

153. Zhang, J. and S. Seeger, *Superoleophobic coatings with ultralow sliding angles based on silicone nanofilaments.* Angewandte Chemie International Edition, 2011. **50**(29): p. 6652-6656.

154. Wang, Y., et al., *Slippery liquid-infused substrates: a versatile preparation, unique anti-wetting and drag-reduction effect on water.* Journal of Materials Chemistry A, 2016. **4**(7): p. 2524-2529.

155. Radhakrishnan, S., et al., *Recycled Polyester—Tool for Savings in the Use of Virgin Raw Material*, in *Environmental Footprints of Recycled Polyester*. 2020, Springer. p. 49-83.

156. Changizi, F. and A. Haddad, *Stabilization of subgrade soil for highway by recycled polyester fiber.* Journal of Rehabilitation in Civil Engineering, 2014. **2**(1): p. 93-105.

157. Celebioglu, A. and T. Uyar, *Electrospun porous cellulose acetate fibers from volatile solvent mixture.* Materials Letters, 2011. **65**(14): p. 2291-2294.

158. Wu, S., et al., *Strongly Dipolar Polythiourea and Polyurea Dielectrics with High Electrical Breakdown, Low Loss, and High Electrical Energy Density.* Journal of Electronic Materials, 2014. **43**(12): p. 4548-4551.

159. Yoon, K., B.S. Hsiao, and B. Chu, *Formation of functional polyethersulfone electrospun membrane for water purification by mixed solvent and oxidation processes.* Polymer, 2009. **50**(13): p. 2893-2899.

160. Xue, C.H., et al., *Fabrication of superhydrophobic and superoleophilic textiles for oil-water separation.* Applied Surface Science, 2013. **284**: p. 464-471.
161. Wikipedia. *X-ray photoelectron spectroscopy*. 2020 [cited 2021].
162. Labroots, ATR-FTIR, in, Labroots, https://www.labroots.com/tag/atr-ftir, 2020. [cited 2021].
163. Rocha, F.S., et al., *Experimental methods in chemical engineering: Ultraviolet visible spectroscopy—UV-Vis.* The Canadian Journal of Chemical Engineering, 2018. **96**(12): p. 2512-2517.
164. Hitachi. *Principle of Differential Thermal Analysis (DTA)* 2020 [cited 2021].
165. Hitachi. *Principle of Differential Scanning Calorimetry (DSC)*. 2020 [cited 2021].
166. Walock, M.J., *Nanocomposite coatings based on quaternary metal-nitrogen and nanocarbon systems*. 2012: The University of Alabama at Birmingham.
167. Bakhtazad, A. and S. Chowdhury, *An evaluation of optical profilometry techniques for CMUT characterization.* Microsystem Technologies, 2019. **25**(9): p. 3627-3642.
168. Laforte, C. and A. Beisswenger. *Icephobic material centrifuge adhesion test*. in *Proceedings of the 11th International Workshop on Atmospheric Icing of Structures, IWAIS, Montreal, QC, Canada*. 2005.
169. Fortin, G., A. Beisswenger, and J. Perron. *Centrifuge adhesion test to evaluate icephobic coatings*. in *AIAA Atmospheric and Space Environments Conference*. 2010.
170. Janjua, Z.A., et al., *Performance and durability tests of smart icephobic coatings to reduce ice adhesion.* Applied Surface Science, 2017. **407**: p. 555-564.
171. Liu, J.P., et al., *Super-Hydrophobic/Icephobic Coatings Based on Silica Nanoparticles Modified by Self-Assembled Monolayers.* Nanomaterials, 2016. **6**(12):232.
172. Marcon, P. and K. Ostanina. *Overview of methods for magnetic susceptibility measurement*. in *PIERS Proceedings*. 2012.

173. Zhou, Z.P. and X.F. Wu, *Electrospinning superhydrophobic-superoleophilic fibrous PVDF membranes for high-efficiency water-oil separation.* Materials Letters, 2015. **160**: p. 423-427.

174. Tiu, B.D.B., et al., *Electrospinning Superhydrophobic and Antibacterial PS/MWNT Nanofibers onto Multilayer Gas Barrier Films.* Macromolecular Symposia, 2017. **374**(1): 1600138.

175. Al-Qadhi, M., et al., *Preparation of superhydrophobic and self-cleaning polysulfone non-wovens by electrospinning: influence of process parameters on morphology and hydrophobicity.* Journal of Polymer Research, 2015. **22**(11):1-9.

176. Mittal, K.L., *Contact Angle, Wettability and Adhesion, Volume 4*. 2006: CRC Press.

177. Shahabadi, S.M.S. and J.A. Brant, *Bio-inspired superhydrophobic and superoleophilic nanofibrous membranes for non-aqueous solvent and oil separation from water.* Separation and Purification Technology, 2019. **210**: p. 587-599.

178. Vanithakumari, S.C., et al., *Fabrication of superhydrophobic and self cleaning PVA-silica fiber coating on 304L SS surfaces by electrospinning.* Journal of Applied Polymer Science, 2021. **138**(13): p. 50118.

179. Zhao, H. and H. Chi, *Electrospun Bead-on-String Fibers: Useless or Something of Value?* Novel Aspects of Nanofibers, 2018: p. 87-102.

180. Huan, S.Q., et al., *Effect of Experimental Parameters on Morphological, Mechanical and Hydrophobic Properties of Electrospun Polystyrene Fibers.* Materials, 2015. **8**(5): p. 2718-2734.

181. Lasprilla-Botero, J., M. Alvarez-Lainez, and J.M. Lagaron, *The influence of electrospinning parameters and solvent selection on the morphology and diameter of polyimide nanofibers.* Materials Today Communications, 2018. **14**: p. 1-9.

182. Song, Z., et al., *Effects of solvent on structures and properties of electrospun poly(ethylene oxide) nanofibers.* Journal of Applied Polymer Science, 2018. **135**(5): 45787.

183. Ji, Y.L., et al., *Analysis of Raman and infrared spectra of poly (vinylidene fluoride) irradiated by KrF excimer laser.* Spectrochimica Acta Part a-Molecular and Biomolecular Spectroscopy, 2008. **70**(2): p. 297-300.

184. Bormashenko, Y., et al., *Vibrational spectrum of PVDF and its interpretation.* Polymer Testing, 2004. **23**(7): p. 791-796.

185. Farooqui, U.R., A.L. Ahmad, and N.A. Hamid, *Effect of polyaniline (PANI) on Poly(vinylidene fluoride-co-hexaflouro propylene) (PVDF-co-HFP) polymer electrolyte membrane prepared by breath figure method.* Polymer Testing, 2017. **60**: p. 124-131.

186. Liu, J. and S. Kumar, *Microscopic polymer cups by electrospinning.* Polymer, 2005. **46**(10): p. 3211-3214.

187. Lee, K.H., et al., *The change of bead morphology formed on electrospun polystyrene fibers.* Polymer, 2003. **44**(14): p. 4029-4034.

188. Lu, C., et al., *Computer simulation of electrospinning. Part I. Effect of solvent in electrospinning.* Polymer, 2006. **47**(3): p. 915-921.

189. Fong, H., I. Chun, and D.H. Reneker, *Beaded nanofibers formed during electrospinning.* Polymer, 1999. **40**(16): p. 4585-4592.

190. Liu, Y., et al., *Controlling numbers and sizes of beads in electrospun nanofibers.* Polymer International, 2008. **57**(4): p. 632-636.

191. Ahn, Y., et al., *Development of high efficiency nanofilters made of nanofibers.* Current Applied Physics, 2006. **6**(6): p. 1030-1035.

192. Padil, V.V., et al., *Electrospun fibers based on carbohydrate gum polymers and their multifaceted applications.* Carbohydrate Polymers, 2020: p. 116705.

193. Jahangir, M.A., et al., *Poly lactic acid (PLA) fibres: Different solvent systems and their effect on fibre morphology and diameter.* American Journal of Chemistry, 2017. **7**(6): p. 177-186.

194. Wannatong, L., A. Sirivat, and P. Supaphol, *Effects of solvents on electrospun polymeric fibers: preliminary study on polystyrene.* Polymer International, 2004. **53**(11): p. 1851-1859.

195. Koombhongse, S., W.X. Liu, and D.H. Reneker, *Flat polymer ribbons and other shapes by electrospinning.* Journal of Polymer Science Part B-Polymer Physics, 2001. **39**(21): p. 2598-2606.

196. Nosonovsky, M. and B. Bhushan, *Multiscale dissipative mechanisms and hierarchical surfaces: friction, superhydrophobicity, and biomimetics.* 2008.

197. Nosonovsky, M. and B. Bhushan, *Roughness optimization for biomimetic superhydrophobic surfaces.* Microsystem Technologies-Micro-and Nanosystems-Information Storage and Processing Systems, 2005. **11**(7): p. 535-549.

198. Moradi, R., et al., *Preparation and Characterization of Polyvinylidene Fluoride/Graphene Superhydrophobic Fibrous Films.* Polymers, 2015. **7**(8): p. 1444-1463.

199. Subramanyam, S.B., K. Rykaczewski, and K.K. Varanasi, *Ice Adhesion on Lubricant-Impregnated Textured Surfaces.* Langmuir, 2013. **29**(44): p. 13414-13418.

200. Dou, R.M., et al., *Anti-icing Coating with an Aqueous Lubricating Layer.* ACS Applied Materials & Interfaces, 2014. **6**(10): p. 6998-7003.

201. Ozbay, S., C. Yuceel, and H.Y. Erbil, *Improved Icephobic Properties on Surfaces with a Hydrophilic Lubricating Liquid.* ACS Applied Materials & Interfaces, 2015. **7**(39): p. 22067-22077.

202. Liu, F.T. and Q.M. Pan, *Facile Fabrication of Robust Ice-Phobic Polyurethane Sponges.* Advanced Materials Interfaces, 2015. **2**(15): 1500219.

203. Zhu, L., et al., *Ice-phobic Coatings Based on Silicon-Oil-Infused Polydimethylsiloxane.* ACS Applied Materials & Interfaces, 2013. **5**(10): p. 4053-4062.

204. Wang, P., Z. Lu, and D. Zhang, *Slippery liquid-infused porous surfaces fabricated on aluminum as a barrier to corrosion induced by sulfate reducing bacteria.* Corrosion Science, 2015. **93**: p. 159-166.

205. Zhou, X., et al., *Superhydrophobic and slippery liquid-infused porous surfaces formed by the self-assembly of a hybrid ABC triblock copolymer*

and their antifouling performance. Journal of Materials Chemistry B, 2018. **6**(3): p. 440-448.

206. Yong, J.L., et al., *Femtosecond Laser Direct Writing of Porous Network Microstructures for Fabricating Super-Slippery Surfaces with Excellent Liquid Repellence and Anti-Cell Proliferation.* Advanced Materials Interfaces, 2018. **5**(7): 1701479.
207. Okada, I. and S. Shiratori, *High-Transparency, Self-Standable Gel-SLIPS Fabricated by a Facile Nanoscale Phase Separation.* ACS Applied Materials & Interfaces, 2014. **6**(3): p. 1502-1508.
208. Liu, Q., et al., *Durability of a lubricant-infused Electrospray Silicon Rubber surface as an anti-icing coating.* Applied Surface Science, 2015. **346**: p. 68-76.
209. Dumont, T., et al., *Laser writing of 2D data matrices in glass.* Thin Solid Films, 2004. **453**: p. 42-45.
210. Lu, W. and A.M. Sastry, *Self-assembly for semiconductor industry.* IEEE Transactions on Semiconductor Manufacturing, 2007. **20**(4): p. 421-431.
211. Nune, S.K., et al., *Chapter 11 - Electrospinning of collagen nanofiber scaffolds for tissue repair and regeneration*, in *Nanostructures for Novel Therapy*, D. Ficai and A.M. Grumezescu, Editors. 2017, Elsevier. p. 281-311.
212. Wu, X.H., et al., *Transparent icephobic coatings using bio-based epoxy resin.* Materials & Design, 2018. **140**: p. 516-523.
213. Wu, X.H. and Z. Chen, *A mechanically robust transparent coating for anti-icing and self-cleaning applications.* Journal of Materials Chemistry A, 2018. **6**(33): p. 16043-16052.
214. Chen, L.Q., et al., *Transparent Slippery Surfaces Made with Sustainable Porous Cellulose Lauroyl Ester Films.* ACS Applied Materials & Interfaces, 2014. **6**(9): p. 6969-6976.
215. Wang, F.J., et al., *Anti-icing performance of transparent and superhydrophobic surface under wind action.* Journal of Sol-Gel Science and Technology, 2015. **75**(3): p. 625-634.

216. Gaharwar, A.K., et al., *Amphiphilic beads as depots for sustained drug release integrated into fibrillar scaffolds.* Journal of Controlled Release, 2014. **187**: p. 66-73.

217. Smith, J.D., et al., *Droplet mobility on lubricant-impregnated surfaces.* Soft Matter, 2013. **9**(6): p. 1772-1780.

218. Mahmut, Tas, et al., *Electrospun nanofibre membrane based transparent slippery liquid-infused porous surfaces with icephobic properties.* Colloids and Surfaces a-Physicochemical and Engineering Aspects, 2020. **585**.

219. Vogel, N., et al., *Transparency and damage tolerance of patternable omniphobic lubricated surfaces based on inverse colloidal monolayers.* Nature communications, 2013. **4**(1): p. 1-10.

220. Kim, P., et al., *Liquid-infused nanostructured surfaces with extreme anti-ice and anti-frost performance.* ACS Nano, 2012. **6**(8): p. 6569-6577.

221. Irajizad, P., et al., *Magnetic slippery extreme icephobic surfaces.* Nature Communications, 2016. **7**(1): p. 1-7.

222. Zhang, J., C. Gu, and J. Tu, *Robust slippery coating with superior corrosion resistance and anti-icing performance for AZ31B Mg alloy protection.* ACS Applied Materials & Interfaces, 2017. **9**(12): p. 11247-11257.

223. Tao, C., et al., *Highly icephobic properties on slippery surfaces formed from polysiloxane and fluorinated POSS.* Progress in Organic Coatings, 2017. **103**: p. 48-59.

224. Coady, M.J., et al., *Icephobic Behavior of UV-cured polymer networks incorporated into slippery lubricant-infused porous surfaces: Improving SLIPS durability.* ACS Applied Materials & Interfaces, 2018. **10**(3): p. 2890-2896.

225. Wang, N., et al., *Robust superhydrophobic coating and the anti-icing properties of its lubricants-infused-composite surface under condensing condition.* New Journal of Chemistry, 2017. **41**(4): p. 1846-1853.

226. Liu, M., et al., *Transparent slippery liquid-infused nanoparticulate coatings.* Chemical Engineering Journal, 2018. **337**: p. 462-470.

227. S. Aghdam, A. and F.C. Cebeci, *Tailoring the Icephobic Performance of Slippery Liquid-Infused Porous Surfaces through the LbL Method.* Langmuir, 2020. **36**(46): p. 14145-14154.

228. Liu, G., et al., *Fabrication of a Porous Slippery Icephobic Surface and Effect of Lubricant Viscosity on Anti-Icing Properties and Durability.* Coatings, 2020. **10**(9): p. 896.

229. Cui, W. and T.A. Pakkanen, *Icephobic performance of one-step silicone-oil-infused slippery coatings: Effects of surface energy, oil and nanoparticle contents.* Journal of Colloid and Interface Science, 2020. **558**: p. 251-258.

230. Boinovich, L.B., K.A. Emelyanenko, and A.M. Emelyanenko, *Superhydrophobic versus SLIPS: Temperature dependence and the stability of ice adhesion strength.* Journal of Colloid and Interface Science, 2022. **606**: p. 556-566.

231. Shen, Y., et al., *Statistically understanding the roles of nanostructure features in interfacial ice nucleation for enhancing icing delay performance.* Physical Chemistry Chemical Physics, 2019. **21**(36): p. 19785-19794.

232. Ruan, M., et al., *Preparation and anti-icing behavior of superhydrophobic surfaces on aluminum alloy substrates.* Langmuir, 2013. **29**(27): p. 8482-8491.

233. Shen, Y., et al., *Icephobic/anti-icing potential of superhydrophobic Ti6Al4V surfaces with hierarchical textures.* RSC Advances, 2015. **5**(3): p. 1666-1672.

234. Abe, J., M. Tenjimbayashi, and S. Shiratori, *Electrospun nanofiber SLIPS exhibiting high total transparency and scattering.* RSC Advances, 2016. **6**(44): p. 38018-38023.

235. Yoo, S.H., et al., *Enhanced Adhesion and Transmittance Uniformity in Laminated Polymer-Dispersed Liquid Crystal Films.* Journal of the Optical Society of Korea, 2014. **18**(6): p. 753-761.

236. Tao, P., et al., *TiO2 nanocomposites with high refractive index and transparency.* Journal of Materials Chemistry, 2011. **21**(46): p. 18623-18629.

237. Sun, S.T., et al., *Refractive Index Engineering as a Novel Strategy toward Highly Transparent and Tough Sustainable Polymer Blends.* Chinese Journal of Polymer Science, 2020. **38**(12): p. 1335-1344.

238. Fillion, R.M., A.R. Riahi, and A. Edrisy, *A review of icing prevention in photovoltaic devices by surface engineering.* Renewable & Sustainable Energy Reviews, 2014. **32**: p. 797-809.

239. Zhu, G., *Fabrication of Slippery Liquid-infused Porous Surfaces Using Layer-by-layer Assembly: Towards Multifunctional Surfaces and Facile Fabrication Processes*. 2018, University of Akron.

240. Anand, S., et al., *How droplets nucleate and grow on liquids and liquid impregnated surfaces.* Soft Matter, 2015. **11**(1): p. 69-80.

241. Ma, X.H., et al., *Porous superhydrophobic polymer/carbon composites for lightweight and self-cleaning EMI shielding application.* Composites Science and Technology, 2018. **158**: p. 86-93.

242. Das, A., et al., *Superhydrophobic and conductive carbon nanofiber/PTFE composite coatings for EMI shielding.* Journal of Colloid and Interface Science, 2011. **353**(1): p. 311-315.

243. Xing, Y.J., et al., *Superhydrophobic coatings on wood substrate for self-cleaning and EMI shielding.* Applied Surface Science, 2018. **436**: p. 865-872.

244. Zou, L., et al., *Superhydrophobization of Cotton Fabric with Multiwalled Carbon Nanotubes for Durable Electromagnetic Interference Shielding.* Fibers and Polymers, 2015. **16**(10): p. 2158-2164.

245. Han, J.T., et al., *Transparent, Conductive, and Superhydrophobic Films from Stabilized Carbon Nanotube/Silane Sol Mixture Solution.* Advanced Materials, 2008. **20**(19): p. 3724.

246. Zou, J.H., et al., *Preparation of a superhydrophobic and conductive nanocomposite coating from a carbon-nanotube-conjugated block copolymer dispersion.* Advanced Materials, 2008. **20**(17): p. 3337.

247. Zhang, Y., K. Ruan, and J. Gu, *Flexible Sandwich-Structured Electromagnetic Interference Shielding Nanocomposite Films with Excellent Thermal Conductivities.* Small, 2021. **17**(42): p. 2101951.

248. Guo, H., et al., *Electrospun fibrous materials and their applications for electromagnetic interference shielding: A review*. Composites Part A: Applied Science and Manufacturing, 2021. **143**: p. 106309.

249. Guo, H., et al., *Flexible TaC/C electrospun non–woven fabrics with multiple spatial-scale conductive frameworks for efficient electromagnetic interference shielding.* Composites Part A: Applied Science and Manufacturing, 2021. **151**: p. 106662.

250. Fridrikh, S.V., et al., *Controlling the fiber diameter during electrospinning.* Physical Review Letters, 2003. **90**(14): 144502.

251. Shokri, B., M.A. Firouzjah, and S.I. Hosseini. *FTIR analysis of silicon dioxide thin film deposited by metal organic-based PECVD.* in *Proceedings of 19th international symposium on plasma chemistry society, Bochum, Germany*. 2009.

252. Das, G., G. Mariotto, and A. Quaranta, *Microstructural evolution of thermally treated low-dielectric constant SiOC : H films prepared by PECVD.* Journal of the Electrochemical Society, 2006. **153**(3): p. F46-F51.

253. Ignat'eva, L.N. and V.M. Buznik, *IR-spectroscopic examination of polytetrafluoroethylene and its modified forms.* Russian Journal of General Chemistry, 2009. **79**(3): p. 677-685.

254. Van Krevelen, D.W. and K. Te Nijenhuis, *Properties of polymers: their correlation with chemical structure; their numerical estimation and prediction from additive group contributions*. 2009: Elsevier.

255. Azimi, A. and P. He, *Effect of gravity in the Cassie-to-Wenzel transition on a micropatterned surface.* MRS Communications, 2020. **10**(1): p. 129-134.

256. Sojoudi, H., et al., *Durable and scalable icephobic surfaces: similarities and distinctions from superhydrophobic surfaces.* Soft Matter, 2016. **12**(7): p. 1938-1963.

257. He, Z., et al., *Design of icephobic surfaces by lowering ice adhesion strength: A mini review.* Coatings, 2021. **11**(11): p. 1343.

258. Bengaluru Subramanyam, S., et al., *Low ice adhesion on nano-textured superhydrophobic surfaces under supersaturated conditions.* ACS Applied Materials & Interfaces, 2016. **8**(20): p. 12583-12587.

259. Kulinich, S. and M. Farzaneh, *How wetting hysteresis influences ice adhesion strength on superhydrophobic surfaces.* Langmuir, 2009. **25**(16): p. 8854-8856.

260. Fu, Q., et al., *Development of sol–gel icephobic coatings: effect of surface roughness and surface energy.* ACS Applied Materials & Interfaces, 2014. **6**(23): p. 20685-20692.

261. Sojoudi, H., G.H. McKinley, and K.K. Gleason, *Linker-free grafting of fluorinated polymeric cross-linked network bilayers for durable reduction of ice adhesion.* Materials Horizons, 2015. **2**(1): p. 91-99.

262. Farhadi, S., M. Farzaneh, and S.A. Kulinich, *Anti-icing performance of superhydrophobic surfaces.* Applied Surface Science, 2011. **257**(14): p. 6264-6269.

263. Sarshar, M.A., et al., *Anti-icing or deicing: Icephobicities of superhydrophobic surfaces with hierarchical structures.* Langmuir, 2018. **34**(46): p. 13821-13827.

264. Pan, R., H. Zhang, and M. Zhong, *Triple-scale superhydrophobic surface with excellent anti-icing and icephobic performance via ultrafast laser hybrid fabrication.* ACS Applied Materials & Interfaces, 2020. **13**(1): p. 1743-1753.

265. Uzoma, P.C., et al., *Anti-bacterial, icephobic, and corrosion protection potentials of superhydrophobic nanodiamond composite coating.* Colloids and Surfaces A: Physicochemical and Engineering Aspects, 2021. **630**: p. 127532.

266. Laroche, A., et al., *Silicone nanofilaments grown on aircraft alloys for low ice adhesion.* Surface and Coatings Technology, 2021. **410**: p. 126971.

267. Crespo, M., et al., *Synergistic effect of magnetite nanoparticles and carbon nanofibres in electromagnetic absorbing composites.* Carbon, 2014. **74**: p. 63-72.

268. Nasouri, K. and A.M. Shoushtari, *Fabrication of magnetite nanoparticles/polyvinylpyrrolidone composite nanofibers and their application as electromagnetic interference shielding material.* Journal of Thermoplastic Composite Materials, 2018. **31**(4): p. 431-446.

269. Chiscan, O., et al., *Electrospun PVC/Fe_3O_4 composite nanofibers for microwave absorption applications.* Materials Letters, 2012. **68**: p. 251-254.

270. Guo, J., et al., *Polypyrrole-interface-functionalized nano-magnetite epoxy nanocomposites as electromagnetic wave absorbers with enhanced flame retardancy.* Journal of Materials Chemistry C, 2017. **5**(22): p. 5334-5344.

271. Shukla, V., *Review of electromagnetic interference shielding materials fabricated by iron ingredients.* Nanoscale Advances, 2019. **1**(5): p. 1640-1671.

272. Al-Saleh, M.H. and U. Sundararaj, *Electromagnetic interference shielding mechanisms of CNT/polymer composites.* Carbon, 2009. **47**(7): p. 1738-1746.